

**Holes in nanowires and
quantum dots:
Spin qubits, Majorana fermions,
and hole and hyperfine interactions**

INAUGURALDISSERTATION

ZUR

Erlangung der Würde eines Doktors der Philosophie

vorgelegt der

Philosophisch-Naturwissenschaftlichen Fakultät

der Universität Basel

VON

Franziska Maier

aus Karlsruhe, Deutschland

Basel, 2015

Originaldokument gespeichert auf dem Dokumentenserver der Universität Basel
edoc.unibas.ch

Dieses Werk ist unter dem Vertrag „Creative Commons Namensnennung-Keine
kommerzielle Nutzung-Keine Bearbeitung 3.0 Schweiz“ (CC BY-NC-ND 3.0 CH)
lizenziiert. Die vollständige Lizenz kann unter
creativecommons.org/licenses/by-nc-nd/3.0/ch/
eingesehen werden.



Namensnennung-Keine kommerzielle Nutzung-Keine Bearbeitung 3.0 Schweiz
(CC BY-NC-ND 3.0 CH)

Sie dürfen: Teilen — den Inhalt kopieren, verbreiten und zugänglich machen

Unter den folgenden Bedingungen:



Namensnennung — Sie müssen den Namen des Autors/Rechteinhabers in der von ihm festgelegten Weise nennen.



Keine kommerzielle Nutzung — Sie dürfen diesen Inhalt nicht für kommerzielle Zwecke nutzen.



Keine Bearbeitung erlaubt — Sie dürfen diesen Inhalt nicht bearbeiten, abwandeln oder in anderer Weise verändern.

Wobei gilt:

- **Verzichtserklärung** — Jede der vorgenannten Bedingungen kann **aufgehoben** werden, sofern Sie die ausdrückliche Einwilligung des Rechteinhabers dazu erhalten.
- **Public Domain (gemeinfreie oder nicht-schützbare Inhalte)** — Soweit das Werk, der Inhalt oder irgendein Teil davon zur Public Domain der jeweiligen Rechtsordnung gehört, wird dieser Status von der Lizenz in keiner Weise berührt.
- **Sonstige Rechte** — Die Lizenz hat keinerlei Einfluss auf die folgenden Rechte:
 - Die Rechte, die jedermann wegen der Schranken des Urheberrechts oder aufgrund gesetzlicher Erlaubnisse zustehen (in einigen Ländern als grundsätzliche Doktrin des **fair use** bekannt);
 - Die **Persönlichkeitsrechte** des Urhebers;
 - Rechte anderer Personen, entweder am Lizenzgegenstand selber oder bezüglich seiner Verwendung, zum Beispiel für **Werbung** oder Privatsphärenschutz.
- **Hinweis** — Bei jeder Nutzung oder Verbreitung müssen Sie anderen alle Lizenzbedingungen mitteilen, die für diesen Inhalt gelten. Am einfachsten ist es, an entsprechender Stelle einen Link auf diese Seite einzubinden.

Genehmigt von der Philosophisch-Naturwissenschaftlichen Fakultät auf
Antrag von

Prof. Dr. Daniel Loss

Dr. Peter Stano

Basel, den 9. Dezember 2014

Prof. Dr. Jörg Schibler
Dekan

Acknowledgments

The work presented here would not have been possible without the support of many people and it is my pleasure to express my gratitude towards them here.

First of all, I would like to thank my supervisor Daniel Loss for accepting me as a PhD student in his group and for giving me the opportunity to work with him. During these four years I benefitted greatly from his knowledge, his ideas, and his ability to create a highly productive as well as enjoyable atmosphere in the group.

Furthermore, I am grateful to Peter Stano for coming all the way from Japan in order to be co-referee for this thesis.

Special thanks go to my close collaborators, Christoph Klöffel, Robert Zielke, Hugo Ribeiro, Tobias Meng, and Jelena Klinovaja, who shared their scientific expertise with me and with whom I had many fruitful discussions as well as pleasant conversations.

Moreover, I would like to acknowledge the remaining group members in Basel for being great colleagues. My thanks go to Samuel Aldana, Ehud Amitai, Daniel Becker, Bernd Braunecker, Christoph Bruder, Stefano Chesi, Carlos Egues, Gerson Ferreira, Suhas Gangadharaiyah, Silas Hoffmann, Kevin van Hoogdalem, Adrian Hutter, Viktoriia Kornich, Axel Lode, Kouki Nakata, Simon Nigg, Andreas Nunnenkamp, Christoph Orth, Fabio Pedrocchi, Diego Rainis, Maximilian Rink, Beat Röthlisberger, Arijit Saha, Manuel Schmidt, Thomas Schmidt, Constantin Schrade, Tibor Sekera, Marcel Serina, Dimitrije Stepanenko, Vladimir Stojanovic, Grégory Strübi, Pawel Szumniak, Rakesh Tiwari, Mircea Trif, Luka Trifunovic, Andreas Wagner, Stefan Walter, Ying-Dan Wang, James Wootton, Robert Zak, and Alexander Zyuzin.

Last but not least, I would like to thank Torf and my family for their unlimited support throughout these years.

Summary

In the last decades much scientific effort was spent on manufacturing and understanding the properties of smaller and smaller condensed matter systems. This eventually resulted in the reliable production of semiconductor quantum dots and nanowires, systems that are reduced to sizes of several (tens of) nanometers in all three or at least two dimensions. The confinement in such nanoscale systems is so strong that quantum effects play a crucial role. Furthermore, the exact energy level or band structure of these systems depends heavily on the material composition, the precise confinement geometry, the intrinsic strain distribution, the spin-orbit interaction, as well as the presence of intrinsic and externally applied electric and magnetic fields.

The feasibility of loading only a single charge carrier onto a quantum dot led to the proposal of the spin qubit, as a possible smallest building block of a semiconductor-based quantum computer. In a spin qubit the quantum information is stored in a superposition of Zeeman-split spin-up and spin-down states. Most crucial for its successful implementation is the reliable control and the proper understanding of the carrier spin dynamics. Solving this task has been a highly active research field ever since, both on the experimental and theoretical side. Most of the research conducted so far focused on electrons in the lowest conduction band states. However, at some point it was realized that holes in the states close to the valence band edge may sometimes offer a more advantageous behavior regarding qubit control and coherence. This is due to the p -type symmetry of the associated Bloch states which results in a strong spin-orbit interaction on the atomic level and in an anisotropic hyperfine interaction that is much weaker than the hyperfine interaction of electrons.

Semiconductor nanowires can serve both as hosts for quantum dots and as one-dimensional channels. Nanowire quantum dots are defined by putting additional closely spaced gates on the nanowire that allow for an electrically

tunable longitudinal confinement. Otherwise, a one-dimensional electron or hole gas forms inside the nanowire. Additionally, it has been proposed that nanowires with strong spin-orbit interaction can be employed as hosts for Majorana fermions. This is of special interest because their non-abelian braiding statistics make Majorana fermions good candidates for topological qubits.

In the first part of this thesis, we focus mostly on holes and hole spins confined to self-assembled quantum dots and quantum dots defined in Ge/Si core/shell nanowires. We calculate the hole spin relaxation and decoherence times in these quantum dots due to hole-spin phonon interactions and hole-spin nuclear-spin interactions that are mediated by the spin-orbit interaction and the hyperfine interaction, respectively. Subsequently, we show how these times are affected by specific system parameters such as intrinsic and extrinsic strain, the confinement strength as well as the magnitude and direction of applied electric and magnetic fields. Furthermore, we determine the effective Zeeman splitting by investigating the anisotropy and tunability of the effective g factor of electrons and holes in the lowest energy levels in these systems. In addition, we investigate the effect of non-collinear terms in the hole-spin nuclear-spin hyperfine interaction which reduce the degree of nuclear spin polarization that can be obtained by optical pumping. Also, we propose an experimental setup that allows to detect and quantify this effect.

In the second part of this work we survey holes in Ge/Si core/shell nanowires by employing an effective one-dimensional microscopic model that includes a strong and electrically tunable Rashba-type spin-orbit interaction. Using a Luttinger liquid description, we show that a screened Coulomb interaction strongly influences the nanowire properties. The strength of the interactions is explicitly quantified by calculating the scaling exponents of correlation functions and by examining the effect of the interactions on a partial gap opened by a small magnetic field. Finally, we consider the nanowires as hosts for Majorana fermions. This is possible when the nanowire is placed in close proximity to an s -wave superconductor and put into a helical regime by applying electric fields. Furthermore, a magnetic field is needed to open a gap in the spectrum. In this setup, we calculate the field dependence of the localization lengths of the associated Majorana fermion wave functions. In short nanowires the Majorana fermions hybridize and form a subgap fermion whose energy oscillates as a function of the applied fields. The oscillation period allows to measure the strength of the spin-orbit interaction and the g factor anisotropy of the nanowire.

Inhaltsverzeichnis

Acknowledgments	v
Summary	vii
Inhaltsverzeichnis	xi
1 Introduction	1
1.1 Solid state systems on the nanoscale	1
1.2 Spin qubits in quantum dots	5
1.3 Nanowires as one-dimensional systems	9
1.4 Frequently used mathematical tools	12
1.5 Outline	14
I Zero-dimensional systems: Quantum dots	15
2 Effect of strain on hyperfine-induced hole-spin decoherence in quantum dots	17
2.1 Introduction	18
2.2 Heavy-hole states in strained quantum dots	19
2.3 Effective hyperfine Hamiltonian of the heavy-hole spin	21
2.4 Effect of strain on the heavy-hole spin dynamics	22
2.5 Summary	26
3 Tunable g factor and phonon-mediated hole spin relaxation in Ge/Si nanowire quantum dots	29
4 Nuclear spin diffusion mediated by heavy hole hyperfine non-collinear interactions	39

5	Anisotropic g factor in InAs self-assembled quantum dots	51
5.1	Introduction	52
5.2	Model	53
5.3	Results	57
5.4	Discussion	62
5.5	Comparison to experiment	64
5.6	Conclusion	65
II	One-dimensional systems: Nanowires	67
6	Strongly interacting holes in Ge/Si nanowires	69
6.1	Introduction	70
6.2	Model	71
6.3	Bosonization	73
6.4	Exponents of the correlation functions	75
6.5	Renormalization of the partial gap	76
6.6	Conclusions	78
7	Majorana fermions in Ge/Si hole nanowires	81
7.1	Introduction	82
7.2	Nanowire Hamiltonian for holes	83
7.3	Tunability of the Majorana fermion localization length	90
7.4	Finite nanowires: hybridized Majorana fermions	95
7.5	Conclusion	98
	Appendix	103
A	Supplementary information for Chapter 2:	
	‘Effect of strain on hyperfine-induced hole-spin decoherence	
	in quantum dots’	103
A.1	Hamiltonian - explicit form	103
A.2	Continuum limit of the memory kernel	104
B	Supplementary information for Chapter 3:	
	‘Tunable g factor and phonon-mediated hole spin relaxation	
	in Ge/Si nanowire quantum dots’	107
B.1	Effective 1D Hamiltonian	107
B.2	Effective 1D phonon Hamiltonian	109

C	Supplementary information for Chapter 4:	
	‘Nuclear spin diffusion mediated by heavy hole hyperfine non-collinear interactions’	111
C.1	Effective heavy hole states in a self-assembled quantum dots . . .	111
C.2	Effective hyperfine interactions of heavy holes	113
C.3	Effective Hamiltonian for optical nuclear spin pumping via bright excitons	115
D	Supplementary information for Chapter 5:	
	‘Anisotropic g factor in InAs self-assembled quantum dots’	119
D.1	Trial wave functions	119
D.2	Material parameters	121
E	Supplementary information for Chapter 6:	
	‘Strongly interacting holes in Ge/Si nanowires’	123
E.1	Calculation of the screened Coulomb matrix elements	123
E.2	Operators and correlation functions in the i, o basis, and transformation to the diagonal basis	124
E.3	Divergences outside the perturbative regime and comparison to a fermionic RG approach	126
F	Supplementary information for Chapter 7:	
	‘Majorana fermions in Ge/Si hole nanowires’	131
F.1	Particle-hole coupling Hamiltonian	131
F.2	Wave functions	131
	Literaturverzeichnis	135
	Curriculum Vitae	153
	List of Publications	155

Introduction

In this Chapter, we present the ideas behind the questions raised and answered in this thesis. Chapter 1.1 introduces the solid state systems considered in this work, semiconductor quantum dots and nanowires. We point out the peculiarities that occur when holes instead of electrons are used and describe different intrinsic and extrinsic effects that influence the structure of the energy levels and bands. As a specific application, we introduce quantum dots as hosts for spin qubits in Chapter 1.2 and indicate system-specific challenges regarding spin coherence times. Chapter 1.3 describes necessary considerations when studying one-dimensional nanowire systems and gives a short introduction to Majorana fermions in nanowires. Mathematical tools that were frequently used in this work are introduced in Chapter 1.4, and, in Chapter 1.5, we give an outline of this thesis.

1.1 Solid state systems on the nanoscale

During the last decades, the exploration of the huge variety of existing solid state systems on the nanoscale has developed into a wide and highly active research field. The considered nanostructures are usually made of III-V (Ga, In, As, Sb), II-VI (Cd, Se), or group-IV (C, Si, Ge) semiconductor materials. In this thesis, we focus on self-assembled quantum dots (QDs) and core/shell nanowires (NWs). The latter can be used either as one-dimensional systems or to implement nanowire quantum dots (NW QDs) by introducing additional longitudinal confinement using electrical gates.

Self-assembled QDs are usually grown in the Stranski-Krastanow mode by epitaxial deposition of a several monolayers thick film of the QD material on substrate wafers [1, 2]. The lattice mismatch between the substrate and the deposited material results in a thin wetting layer that is topped with isolated islands, the QDs. Typical self-assembled QDs are several tens of nanometers

wide and a few nanometers high. A popular method for NW growth is the vapor-liquid-solid method [1, 3–5], which allows to produce large numbers of NWs under identical conditions. In this method, metal particles deposited to the substrate serve as catalysts that react with the substrate material as well as with the surrounding gas phase. Eventually, a crystalline NW starts to grow from the substrate, and its properties can be modified by tuning the growth temperature and the saturation of the gas phase. Furthermore, it is possible to grow several shells around the NW in successive steps. This process results in so-called core/(multi)shell NWs. Typical NW diameters are on the scale of several tens of nanometers, while the NW length can reach several micrometers.

It is possible to trap both types of charge carriers, electrons and holes, in QDs and NWs. However, due to the different symmetries of the Bloch states close to the valence band edge in bulk semiconductors, it is possible to observe striking differences when comparing hole physics with electron physics. These differences manifest themselves, for example, in the interaction strength of the charge carriers with the environment and related phenomena. The Bloch states of the lowest conduction band are of s -type ($l = 0$) symmetry contrasted by the p -type ($l = 1$) symmetry of the Bloch states of the hole bands close to the valence band edge [1, 6]. Including spin ($s = 1/2$) the latter gives rise to a total angular momentum with eigenvalues $j = l + s = 3/2$ and $j = l - s = 1/2$ for the hole states. Furthermore, the p -type symmetry of the hole Bloch states results in a strong spin-orbit interaction on the atomic level. This leads to a splitting between the $j = 3/2$ and $j = 1/2$ bands in the bulk semiconductor. For the $j = 3/2$ bands one distinguishes between the heavy hole ($j_z = \pm 3/2$) and the light hole ($j_z = \pm 1/2$) band. They are strongly coupled and remain degenerate at the center of the Brillouin zone Γ ($k = 0$). Because of this, the heavy and light hole states are usually described jointly by the Luttinger Hamiltonian, which includes all coupling terms between the states [6, 7]. While band parameters such as the effective mass and the g factor are isotropic for the lowest conduction band, they are highly anisotropic for the hole bands close to the valence band edge. In Fig. 1.1 a sketch of the approximate band structure in bulk semiconductors around Γ is shown.

Energy levels and bands in QDs and NWs

The band structure of bulk semiconductors is well researched, both in theory and experiment [1, 8]. However, the energy levels or bands of semiconductor

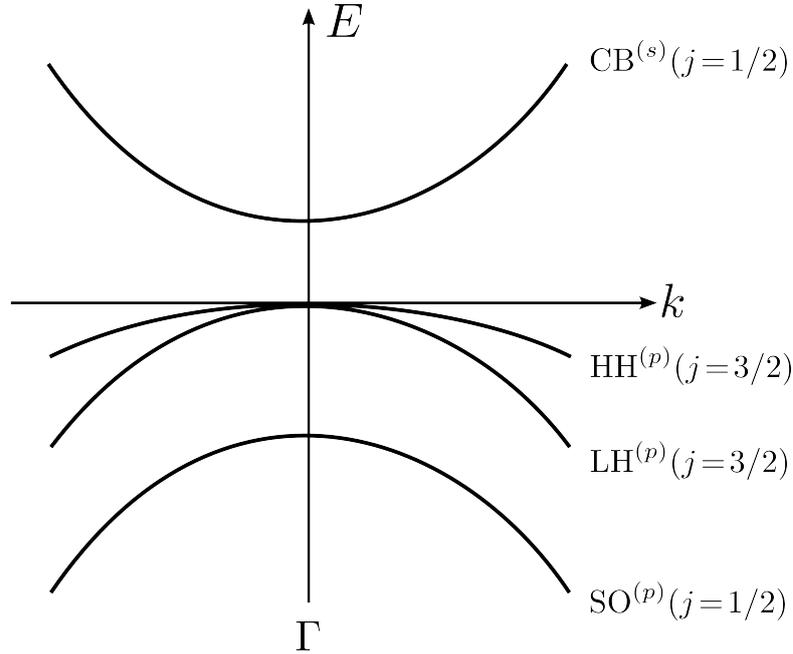


Abbildung 1.1: Sketch of the band structure of a bulk semiconductor around Γ at the valence band edge. The lowest conduction band (CB, s symmetric), the heavy hole band (HH, p symmetric), the light hole band (LH, p symmetric) and the split-off band (SO, p symmetric) are shown. Each band is two-fold spin degenerate.

QDs or NWs, respectively, deviate strongly from the level structure of the bulk material due to the reduced dimensionality and other band mixing effects. As described in detail below, the material composition, the precise confinement geometry, the intrinsic strain distribution, the spin-orbit interaction, as well as the presence of intrinsic and externally applied electric and magnetic fields may affect the level and band structure and related observables such as the conductivity and the optical response. Therefore, even the mere characterization of the physical properties of QDs and NWs is an active field.

Material composition. The Stranski-Krastanow growth mode that is commonly employed to obtain self-assembled QDs results in a gradient of the material composition inside the QD, changing from the substrate material to the deposited material along the growth axis of the QD [9, 10]. This effect is not significant for NWs, since the material composition is only determined by the growth material coming from the gas phase. However, the knowledge of the exact material buildup in the NWs is equally important, especially when separate core and shell materials are used.

Confinement. Due to the confinement of charge carriers to very small

systems, quantum effects become important and the confinement potential eventually determines the level splitting. Generally speaking, a stronger confinement leads to a stronger energy splitting. This can already be inferred from simple, analytically solvable confinement models such as the potential well or the harmonic oscillator. The equidistant level spacing observed in self-assembled QDs validates the usage of harmonic potentials when modeling the QD confinement [11]. Additional anisotropies of the confinement such as in flat, pyramidal or dome-like QDs, as well as in NWs further influence the energy splitting. The longitudinal confinement in NW QDs is produced by electric gates that allow for modifications of the confinement potential.

Static strain. During the QD growth in the Stranski-Krastanow mode the atoms deposited on the wetting layer eventually form small islands because of the lattice mismatch of the substrate and the deposited material. This results in QDs that show a rich strain profile [12, 13]. In addition to the intrinsic strain profile, strain can be applied to QDs by external means [14, 15], allowing for a (dynamic) alteration of the strain profile. In core/(multi)shell NWs, the presence of a shell induces compressive or tensile strain into the core due to the lattice mismatch of the core and shell material. This results in a strong dependence of the strain profile on the shell thickness [16, 17]. Since it is very complicated to obtain analytical models for the spatially varying strain distribution in QDs and NWs, one usually resorts to numerical models.

Spin-orbit interaction. The spin-orbit interaction is an effect which can be described using the Dirac equation and that can be understood intuitively when considering an electron moving in an electric field: in the electron's rest frame the latter is seen as an effective magnetic field that couples to the electron spin. Thus a moving electron experiences a spin rotation. In semiconductor crystals one finds different manifestations of the spin-orbit interaction. One is the spin-orbit interaction on the atomic level where the Bloch states couple. The others are the Rashba spin-orbit interaction originating in the structure inversion asymmetry as it is, for example, present in the asymmetric potential of a quantum well [18, 19], and the Dresselhaus spin-orbit interaction from the bulk inversion asymmetry as it exists in zincblende crystals [20]. In both cases, the inversion asymmetry causes internal electric fields that couple to the spin of the charge carriers. A detailed introduction into spin-orbit interaction in semiconductors can be found in Ref. [6]. In semiconductor nanostructures, the spin-orbit interaction leads to a mixing of the orbital and spin degrees of freedom [21] and, in the case of NWs, to helical states caused by the lifted spin degeneracy [22, 23]. The strength of the spin-orbit interaction

has been measured for QDs and NW QDs [24, 25]. However, even though measurement schemes for the spin-orbit interaction in NWs have been presented [26], their interpretation is not yet considered conclusive [27]. In addition to the known spin-orbit terms, a Rashba-type spin-orbit interaction caused by the direct dipolar coupling to the external electric field was predicted in Ge/Si core/shell NWs [23].

Electric fields. Applying external electric fields alters the intrinsic fields produced by the structure inversion asymmetry present in the system, thus the Rashba spin-orbit interaction can be tuned. Furthermore, the influence of the electric fields on the confinement potentials shifts the position of the wave functions of the confined charge carriers inside the nanostructure.

Magnetic fields. External magnetic fields couple to charge carriers via the orbital motion through a vector potential and to the carrier spin via the Zeeman effect. The latter lifts the spin degeneracy and induces a gap in the spectrum. The Zeeman splitting is characterized by the effective g factor which in QDs and NWs deviates strongly from the value of a free electron. The effective g factor depends on the band under consideration and the direction of the magnetic field, thus it can be anisotropic. In QDs and NWs made of materials with non-zero nuclear spins an additional intrinsic magnetic field, the Overhauser field, is present. In thermal equilibrium its net value is very small, around 10^{-3} Tesla. This changes if the nuclear spins are polarized, here the net value of the Overhauser field can reach a few Tesla [28].

Considering this list of internal and external mechanisms that influence the exact level or band structure in QDs and NWs, it is obvious that a thorough analysis is very complex. However, it is possible to cast subsets of interacting bands or levels into analytical or numerical models that capture the essential characteristics and provide the basis for further investigations.

1.2 Spin qubits in quantum dots

One of the most intriguing ideas regarding QD applications is to use them as hosts for the smallest building block of quantum computers, the qubit. It was proposed in 1998 that one of the most natural qubit implementations are two Zeeman-split states of an electron spin confined to a QD [29]. Here, the quantum information is stored in a superposition of the spin-up and spin-down states that is commonly represented as a point on the Bloch sphere, see Fig. 1.2. The time evolution of the qubit state then corresponds to a trajectory

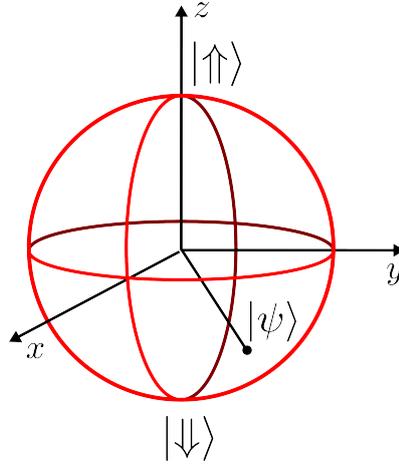


Abbildung 1.2: Bloch sphere representation of a qubit state $|\psi\rangle$, being a superposition of $|\uparrow\rangle$ and $|\downarrow\rangle$. Single qubit operations correspond to rotations around the axes of the Bloch sphere.

ry on the sphere's surface. The authors envisioned that single qubit rotations could be achieved by applying oscillating magnetic fields and that two-qubit gates could be implemented by employing the tunability of the exchange interaction (the latter is only possible for gate-defined QDs). Later on, several criteria that have to be met for the successful implementation of a qubit were formulated [30]: a scalable system with well defined qubits is needed, the qubit initialization and readout must be achievable with sufficiently high fidelity, the implementation of a universal set of quantum gates must be possible, and the qubit coherence times must be much longer than the qubit gate operation times.

Electron and hole spin qubit initialization, manipulation and readout are already performed as standard processes in laboratories all around the world [31–43]. The implementation of a universal set of quantum gates requires single qubit rotations and entangling two-qubit gates [29, 44]. The latter are especially challenging for self-assembled QDs since the employed optical approaches need resonant photons from the involved QDs, a circumstance that is not naturally given but can be achieved by means of strain-tuning or electric and magnetic fields [45]. However, the most limiting factors in semiconductor-based qubits are the short spin coherence times T_1 and T_2 . Here, T_1 denotes the spin relaxation time, thus the time in which a spin relaxes from the up- to the down-spin state. T_2 is the spin decoherence time and denotes the time in which a superposition of the two spin states decays into one of them.

Single qubit manipulation

The initial proposal of a spin qubit suggested that single-qubit rotations around one of the qubit axes could be performed by applying oscillating magnetic fields [29]. This electron spin resonance method drives Rabi oscillations between the two qubit levels by means of a magnetic field that oscillates perpendicular to the field that causes the Zeeman splitting, with the oscillation frequency in resonance with the Zeeman energy [45]. The suggested scheme was successfully implemented in 2006 [46]. However, it proves to be much easier to control locally oscillating electric fields than to control locally oscillating magnetic fields. Therefore different schemes to induce the qubit rotations have been developed that aim to reproduce the oscillating magnetic field needed to drive the Rabi oscillations while involving only static magnetic fields.

In the method presented in Ref. [47], the charge carrier performs electric-field-induced oscillations in a static magnetic field gradient that is produced by a nearby micromagnet. Another method, which was first introduced for spins in two-dimensional heterostructures [48], displaces the electron wave function to regions with different material composition and thus different g factors while a static magnetic field is applied. The application of this scheme was proposed in Refs. [49, 50] and successfully applied in Ref. [51]. An all-electrical scheme to obtain qubit control is the electric-dipole-induced spin rotation [52, 53]. Here, the presence of a strong spin-orbit interaction in the system causes the carrier spin to see an oscillating magnetic field that enables the spin rotation.

Qubit coherence

To facilitate the implementation of standard quantum error correction schemes [45, 54] the spin lifetimes, T_1 and T_2 , must by far exceed the timescales related to the qubit gate operations. This is because, depending on the specific error correction scheme, the application of roughly $10^2 - 10^4$ gate operations must be possible before the system decoheres. The interactions of the carrier spin with its environment influence the spin lifetimes heavily. This poses one of the fundamental problems regarding the successful implementation of semiconductor spin qubits. The main decay channels are the coupling of the spin to the phonon bath mediated by the spin-orbit interaction, causing spin relaxation, and the coupling of the spin to the nuclear spin bath via the hyperfine interaction, causing spin decoherence [21, 28, 45, 55]. Both coupling mechanisms are described in detail below.

Spin relaxation. Phonons in semiconductors cause electric field fluctua-

tions by displacing the atoms in the crystal lattice from their equilibrium position. By means of these fluctuations, the phonons couple to charge carriers either via the deformation potential or via the piezoelectric interaction [56–58], where the latter exists only in polar semiconductors with more than a single atomic species in the unit cell. However, phonons cannot couple directly to the carrier spin. This changes when spin-orbit interaction is present in the system. Here, the eigenstates of the system are mixed in terms of orbital states and spin states, enabling the phonons to couple to the effective spin [21, 59]. By treating the spin-orbit interaction as a perturbation, an effective coupling Hamiltonian for the spin qubit can be derived. Here, the charge carrier-phonon interaction manifests itself as a fluctuating magnetic field that causes spin relaxation [59]. When comparing the relaxation rates for electron spins and hole spins in QDs, one finds that the rates for hole spins are either comparable or much smaller than the electron spin relaxation rates [60].

Spin decoherence. A typical QD consists of roughly $10^4 - 10^6$ atoms with slowly fluctuating nuclear spins. The wave function of a charge carrier confined to the QD is spread over all nuclei. The charge carrier interacts with each one via the hyperfine interaction whose terms are derived from the Dirac equation. One obtains three coupling terms [61, 62]: the isotropic Fermi contact interaction, the dipole-dipole type anisotropic hyperfine interaction, and the coupling of the orbital angular momentum to the nuclear spin. The Fermi contact interaction is of great importance for the s -symmetric orbitals of electrons in the lowest conduction band, resulting in an isotropic hyperfine interaction term [63]. In contrast to this, the anisotropic hyperfine interaction and the coupling of the orbital angular momentum to the nuclear spins are of importance for the p -symmetric orbitals of holes [64]. This results in a hole hyperfine interaction of predominantly Ising form and reduces its strength to 10% of the electron hyperfine interaction strength [64–66]. Common routines to reduce or control the effects of the nuclear spin bath on the electron or hole spin are nuclear spin polarization and nuclear state narrowing [45, 67]. Dynamical nuclear spin polarization employs electron or hole spin-nuclearspin flip-flop processes induced by optical [68], electrical [69–71] or magnetic means [72, 73], but the maximal nuclear spin polarizations obtained so far were only 50-70%. This is far from sufficient since the degree of polarization must approach 100% for a significant reduction of the spin decoherence times [67]. Nuclear state narrowing [67, 71, 73–77] reduces the intrinsic nuclear spin distribution by indirect measurement and is a byproduct of several dynamical nuclear polarization schemes [45]. A completely different approach to control

the nuclear spin bath is to avoid hyperfine interaction at all by using materials with zero nuclear spin, for example the zero spin isotopes of group-IV materials such as C, Ge or Si, and growing the nanostructures in a purified fashion [78].

1.3 Nanowires as one-dimensional systems

Even though NWs are fully three-dimensional systems, they can be described as quasi one-dimensional channels with associated one-dimensional physical properties at low energies. Suitable one-dimensional models with microscopic parameters are obtained by integrating out the transverse degrees of freedom of initially three-dimensional models [23]. Due to the reduced dimensionality, interacting particles can no longer be described by Fermi liquid theory. Instead, Luttinger liquid theory has to be employed to characterize low-energy excitations in the NWs.

In 2010, it was realized that NWs could serve as hosts for Majorana fermions. They are of special interest due to their possible applications in topological quantum computation and non-local quantum information storage.

Luttinger liquid theory

Fermi liquid theory successfully describes the low-energy excitations of (Coulomb-) interacting fermions in two- and three-dimensional systems [58, 79]. Here, the interacting particles are represented in terms of non- or weakly interacting quasiparticles with effective parameters. However, when considering interacting electrons in a one-dimensional system the Fermi liquid theory fails [80, 81]. Intuitively, this can be understood when considering Fig. 1.3 (a), where interacting fermionic particles in a one-dimensional system are displayed. If a particle gets excited, as indicated by the red arrow, it starts to move and unavoidably bumps into the neighboring particles, hereby transferring momentum and energy. This happens throughout the system until the excitation energy is distributed among all particles. Thus, the low-energy degrees of freedom in a one-dimensional system are not single-particle excitations but (bosonic) density waves. In spinful systems, one additionally finds a spin-charge separation, meaning that spin density waves and charge density waves can exist independently of each other. Besides, the Mermin-Wagner theorem [82, 83] allows to conclude that there exists no true long-range order in one-dimensional systems. To describe the low-energy excitations adequate-

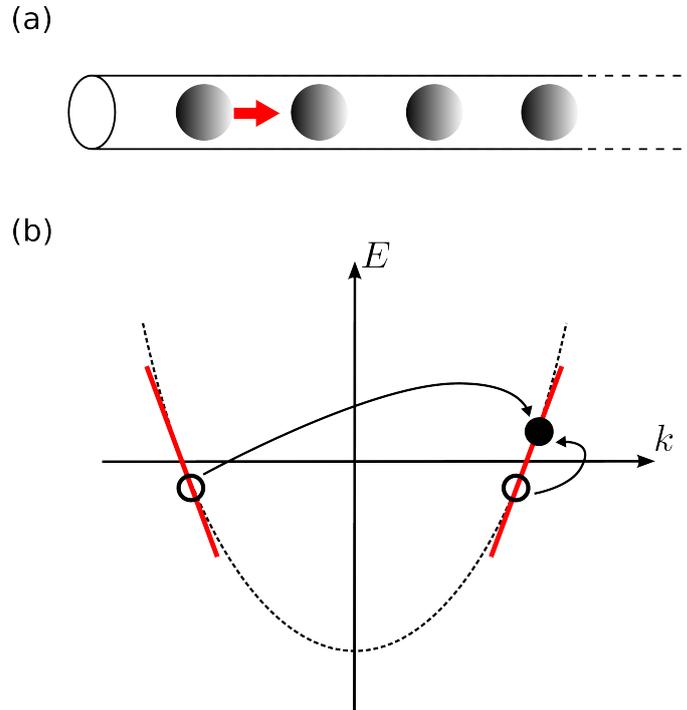


Abbildung 1.3: (a) Fermionic particles in a one-dimensional system. Exciting a single particle (red arrow) leads to unavoidable collisions and thus momentum and energy transfer between the particles. (b) Linearized spectrum (red) of the fermions around the Fermi points with possible low-energy excitations of a particle. The dotted line shows the initial parabolic spectrum.

ly, the Luttinger liquid theory is used. An elaborate introduction can be found in Ref. [81].

A crucial ingredient for making common one-dimensional problems solvable is the bosonization technique [81, 84], which allows to represent fermionic fields in terms of bosonic fields that describe the bosonic density waves. When considering only low-energy excitations, one can approximate the kinetic energy of the fermions by a linearized dispersion relation around the Fermi points, see Fig. 1.3 (b). After linearization of the kinetic energy one can show that the kinetic part of the Hamiltonian as well as many of the interactions can be expressed in terms that are quadratic in the bosonic operators, thus they can be readily diagonalized.

The experimentally accessible properties of one-dimensional systems are correlation functions. They decay as non-universal power laws with increasing distance, thus indicating that true long-range order is suppressed. The scaling exponents reveal details about the strength of the interactions.

Majorana fermions

Majorana fermions were introduced by E. Majorana in 1937 [85] as solutions of the Dirac equation in a modified basis. These solutions are real fields, thus the associated particles must be their own antiparticles. Since then, scientists have tried to design experimental platforms where Majorana fermions could be observed in condensed matter systems. In 2010, an experimental setup was proposed involving semiconductor NWs with a sizable spin-orbit interaction. Key ingredients is one of said NWs coupled to a *s*-wave superconductor and a magnetic field that opens a gap in the spectrum [86–89]. The setup has been predicted to allow for Majorana fermion bound states to form at the ends of the NW. Subsequently, efforts to realize the proposed model have been made in several experiments [90–94]. However, the observed signatures do not unambiguously point to the existence of Majorana fermions but could also be caused by other effects.

The tremendous amount of interest in finding Majorana fermions in rather small condensed matter systems is not only motivated by finding proof of their mere existence. Because Majorana fermions are non-abelian anyons [95] their braiding statistics makes them good candidates for topological quantum computation [96, 97]. Additionally, Majorana fermions can be used to store quantum information non-locally, thus immune to local perturbations that cause decoherence. A logical Majorana-based qubit consists of four Majorana fermions [97, 98] and might be implemented in NW networks [99].

1.4 Frequently used mathematical tools

Here we present mathematical tools that are frequently used in this thesis, the $\mathbf{k} \cdot \mathbf{p}$ method and the Schrieffer-Wolff transformation. The $\mathbf{k} \cdot \mathbf{p}$ method is an approximation scheme to calculate the electronic band structure of semiconductors. The Schrieffer-Wolff transformation is a quasi-degenerate perturbation theory that is employed to approximately block-diagonalize Hamiltonians.

$\mathbf{k} \cdot \mathbf{p}$ method

The $\mathbf{k} \cdot \mathbf{p}$ method is an approximation technique that allows to calculate the electronic band structure of semiconductors for small wave vectors \mathbf{k} around an expansion point \mathbf{k}_0 for which the system is exactly solvable, for example around Γ [1, 6]. In the derivation of the $\mathbf{k} \cdot \mathbf{p}$ method one uses the Schrödinger equation with the Pauli spin-orbit interaction and the lattice periodic crystal potential that acts on the Bloch functions,

$$\left[\frac{p^2}{2m_0} + V_0(\mathbf{r}) - \frac{\hbar}{4m_0^2 c^2} \boldsymbol{\sigma} \cdot \mathbf{p} \times (\nabla V_0(\mathbf{r})) \right] e^{i\mathbf{k} \cdot \mathbf{r}} u_{n\mathbf{k}}(\mathbf{r}) = E_n(\mathbf{k}) e^{i\mathbf{k} \cdot \mathbf{r}} u_{n\mathbf{k}}(\mathbf{r}). \quad (1.1)$$

Here, \mathbf{p} is the momentum operator, m_0 is free electron mass, $V_0(\mathbf{r})$ is the lattice periodic potential, \hbar is the reduced Planck constant, c is the speed of light, and $\boldsymbol{\sigma} = (\sigma_x, \sigma_y, \sigma_z)$ is the vector of the Pauli spin matrices. The Bloch functions $e^{i\mathbf{k} \cdot \mathbf{r}} u_{n\mathbf{k}}(\mathbf{r})$, with band index n , consist of a plane wave part $e^{i\mathbf{k} \cdot \mathbf{r}}$ and a lattice periodic part $u_{n\mathbf{k}}(\mathbf{r})$. The momentum operator acts on the plane wave part of the Bloch functions and a Schrödinger equation for the $u_{n\mathbf{k}}$ is obtained. For a fixed wavevector \mathbf{k}_0 the associated $\{u_{n\mathbf{k}_0}\}$ form a complete orthonormal basis, and one can express the $u_{n\mathbf{k}}$ for arbitrary \mathbf{k} as expansions in terms of this basis. By taking matrix elements of the Schrödinger equation for an arbitrary \mathbf{k} in terms of the orthonormal basis, one obtains a infinite-dimensional matrix that takes into account couplings between all existing bands of the semiconductor. One is usually interested in a finite-dimensional subset of bands, thus the subspace of interest is truncated from the coupling to remote bands by a Schrieffer-Wolff transformation. Due to this transformation higher order terms in \mathbf{k} appear in the resulting Hamiltonian and effective band parameters have to be taken into account. The finite-dimensional Hamiltonians obtained by the $\mathbf{k} \cdot \mathbf{p}$ method can be examined and supported by the theory of invariants [6]. Here, arguments from group theory are employed to decide which terms must persist in the Hamiltonian and which terms must vanish. This is based

on the fact that the Hamiltonian must remain invariant when applying certain symmetry operations.

Most relevant for band structure calculations close to the valence band edge are the Kane Hamiltonian [100], which includes the lowest conduction band, the heavy- and light-hole bands, and the split-off band and the Luttinger Hamiltonian [7], which includes only the heavy- and light-hole bands.

Schrieffer-Wolff transformation

The Schrieffer-Wolff transformation [6, 101] is a method of quasi-degenerate perturbation theory which is used to approximately block-diagonalize time-independent Hamiltonians. This results in the effective decoupling of two formerly weakly interacting subspaces of the Hamiltonian up to a desired order. In general, the procedure can be seen as a rotation of a Hamiltonian H by a unitary operator e^S ,

$$H \rightarrow \tilde{H} = e^S H e^{-S}, \quad (1.2)$$

with S being an anti-Hermitian operator ($S^\dagger = -S$) and where \tilde{H} is of block-diagonal form. One aims to approximate e^S such that the decoupling is performed to the desired order. To this, the Hamiltonian H is subdivided into $H = H_0 + H'_d + H'_{od}$, where H_0 is the leading order term with known eigenstates and eigenenergies. H'_d and H'_{od} are perturbing terms, where H'_d is diagonal and H'_{od} is off-diagonal with respect to the two subspaces being decoupled. The unitary operator is expanded in a series, $e^S \approx 1 + S + S^2/2 + \dots$, and for the anti-Hermitian operator S the ansatz $S = S_1 + S_2 + S_3 + \dots$ is employed, where the subscript of the S_i , $i = 1, 2, 3, \dots$, denotes the order of S_i in the matrix elements coupling the two subspaces divided by the associated energy splitting. Reinserting the expansion of e^S and the ansatz for S into the definition of \tilde{H} allows to determine the components of the S_i by eliminating the block-off-diagonal terms of the same order in \tilde{H} . Approximating S to first order, one finds that S_1 is given by $[S_1, H_0] = H'_{od}$. To second order, the block diagonal Hamiltonian is then given by

$$\tilde{H} \approx H_0 + H'_d - [S_1, H'_{od}] + \frac{1}{2}[S_1, [S_1, H_0]]. \quad (1.3)$$

Explicit expressions for higher order terms of the S_i and \tilde{H} are given in Ref. [6].

1.5 Outline

The first chapters of this thesis deal with topics related to spin qubits in QDs. In Chapter 2, we investigate the effect of strain on the decoherence rate of hole spins in QDs induced by the hyperfine coupling to the surrounding nuclear spins. This is followed by Chapter 3, where we consider the tunability and anisotropy of the g factor in Ge/Si core/shell NW QDs and calculate the spin-orbit interaction mediated hole-spin phonon relaxation rates. In Chapter 4, we show that the non-collinear heavy-hole hyperfine interaction influences the nuclear spin dynamics, and, in Chapter 5, we consider the anisotropy of the electron g factor in self-assembled pyramidal InAs QDs.

In the two final chapters of this work we study NWs as one-dimensional systems. We investigate and quantify the hole-hole interactions in Ge/Si core/shell NWs by means of Luttinger liquid theory in Chapter 6. In Chapter 7, the tunability of Majorana fermion wave function localization lengths in Ge/Si core/shell NWs is investigated.

Supplementary information for Chapters 2 to 7 can be found in the Appendices A to F.

Teil I

**Zero-dimensional systems:
Quantum dots**

Effect of strain on hyperfine-induced hole-spin decoherence in quantum dots

Adapted from:

F. Maier and D. Loss,

'Effect of strain on hyperfine-induced hole-spin decoherence in quantum dots',

Phys. Rev. B **85**, 195323 (2012).

We theoretically consider the effect of strain on the spin dynamics of a single heavy hole (HH) confined to a self-assembled quantum dot and interacting with the surrounding nuclei via hyperfine interaction. Confinement and strain hybridize the HH states, which show an exponential decay for a narrowed nuclear spin bath. For different strain configurations within the dot, the dependence of the spin decoherence time T_2 on external parameters is shifted and the non-monotonic dependence of the peak is altered. Application of external strain yields considerable shifts in the dependence of T_2 on external parameters. We find that external strain affects mostly the effective hyperfine coupling strength of the conduction band (CB), indicating that the CB admixture of the hybridized HH states plays a crucial role in the sensitivity of T_2 on strain.

2.1 Introduction

During the last years, heavy-hole (HH) spins have attracted much interest in the field of spintronics and spin-based quantum computing. This is because, compared to the timescales set by the electron spin, very long hole spin relaxation times $T_1 \approx 1\text{ms}$ have been predicted [60, 102] and confirmed experimentally [33, 37]. Furthermore, ensemble hole spin coherence times $T_2^* > 100\text{ns}$ have been measured [103]. Alongside, the essential ingredients for processing quantum information successfully, hole spin initialization [37, 38] and coherent control of single hole spins [41–43], have been shown in quantum dots. Additionally, methods applicable to overcome decoherence, e.g., by preparing the nuclear spin bath in a narrowed state [67, 71, 73–77], have been introduced. The prolonged timescales regarding decoherence are attributed to the Ising-like hyperfine coupling of holes [64] due to the p -wave symmetry of the Bloch states in the valence band (VB). Recently, the hyperfine interaction strength of holes was predicted to be approximately 10% of the interaction strength of electrons [64]. This was confirmed in experiments carried out in self-assembled InAs quantum dots [65, 66]. The associated hole spin decoherence time T_2 was shown to depend on external parameters in a non-monotonic fashion [104]. Due to lattice mismatch, the strain profiles of InAs/GaAs dots show a compression in the lateral plane and a stretching in the vertical direction [13]. The associated strain fields are of considerable strength and may strongly affect the band hybridization in the dot and hence the spin decoherence. For the light hole (LH) and HH band, the effect of confinement and anisotropic lateral strain on band mixing and on the interaction with a Gaussian nuclear field distribution via dipole-dipole hyperfine interaction has been considered in Refs. [105, 106]. In the present chapter, we examine the effect of realistic strain distributions on the spin decoherence time T_2 of a single HH spin confined to a self-assembled InAs quantum dot interacting with a narrowed nuclear spin bath via hyperfine interaction. We follow the procedure outlined in Ref. [104] with emphasis on the new features coming from strain. The emerging band hybridization is strain dependent and shows considerable admixtures of the lowest conduction band (CB), and the LH and the split-off (SO) band of the VB. An effective hyperfine Hamiltonian is derived from the hybridized states being, for realistic strain configurations, predominantly of Ising form with small hole-nuclear-spin flip-flop terms which cause exponential spin decoherence. We study the effect of various internal strain configurations and of applied external strain on the decoherence rate $1/T_2$ and its dependence on external parameters. Applying

external strain up to the breaking limit of the sample affects the effective hyperfine coupling of the CB admixture much more than the coupling of the LH admixture. In contrast to this, the changes in the Ising like HH coupling are negligible. This indicates the significance of the CB admixture regarding the changes of $1/T_2$ due to strain.

The outline of this chapter is as follows. In Sec. 2.2 we introduce the 8×8 $\mathbf{k} \cdot \mathbf{p}$ Hamiltonian describing states confined with a strained quantum dot and calculate the hybridized eigenstates of the HH subsystem. We find an effective Hamiltonian which describes the hyperfine interaction of the hybridized HH spin states with the surrounding nuclei in Sec. 2.3. In Sec. 2.4 we derive the dynamics of the transverse HH pseudospin states and examine the effect of strain on the decoherence time T_2 and on the hyperfine coupling constants. A summary can be found in Sec. 2.5. Technical details are deferred to App. A.

2.2 Heavy-hole states in strained quantum dots

We use the 8×8 $\mathbf{k} \cdot \mathbf{p}$ Kane Hamiltonian H_K which describes the states of bulk zincblende semiconductors in the lowest CB and in the HH, the LH, and the SO band of the VB [6, 100]. We assume a flat, cylindric dot geometry which is taken into account by choosing harmonic confinement V_{conf} with lateral and vertical confinement lengths L and a , respectively, satisfying $L \gg a$. For detailed expressions of H_K and V_{conf} see Appendix A.1. Strain is added perturbatively to the system by employing an 8×8 strain Hamiltonian H_ϵ [6, 107] of the form

$$H_\epsilon = \begin{pmatrix} S_{11} & S_1 & S_2 & S_3 \\ S_1^\dagger & S_{22} & S_4 & S_5 \\ S_2^\dagger & S_4^\dagger & S_{33} & S_6 \\ S_3^\dagger & S_5^\dagger & S_6^\dagger & S_{44} \end{pmatrix}, \quad (2.1)$$

where the relevant block matrix elements are

$$\begin{aligned} S_1 &= \begin{pmatrix} E^* & 0 \\ 0 & -E \end{pmatrix}, & S_{22} &= \begin{pmatrix} F + G & 0 \\ 0 & F - G \end{pmatrix}, \\ S_4 &= \begin{pmatrix} I & J^* \\ J & I^* \end{pmatrix}, & S_5 &= \frac{1}{\sqrt{2}} \begin{pmatrix} -I & -2J^* \\ 2J & I^* \end{pmatrix}. \end{aligned} \quad (2.2)$$

The entries read $E = \sqrt{2}P[k_x \varepsilon_{xx} - ik_y \varepsilon_{yy}]$, $F = D_d \text{Tr} \varepsilon - 1/3 D_u (\varepsilon_{xx} + \varepsilon_{yy} - 2\varepsilon_{zz})$, $G = 3/2 C_4 [k_z (\varepsilon_{xx} - \varepsilon_{yy})]$, $I = \sqrt{3}/2 C_4 [k_x (\varepsilon_{yy} - \varepsilon_{zz}) + ik_y (\varepsilon_{xx} - \varepsilon_{zz})]$,

and $J = 1/\sqrt{3}D_u(\varepsilon_{xx} - \varepsilon_{yy})$. Here, P is the matrix element of the inter-band momentum as defined in Ref. [6], and ε_{ii} , $i = x, y, z$, are the diagonal components of the strain tensor. D_d and D_u denote deformation potentials and the constant C_4 is defined in Ref. [107]. For simplicity, we restrict ourselves to a diagonal strain tensor ε since, due to symmetry, the shear strain components are only of appreciable size at the dot interfaces and negligible everywhere else. This assumption is valid because, due to their small effective mass, holes are strongly confined to the center of quantum dots [13]. In the vicinity of the Γ -point, the basis states in the single bands of the unperturbed Hamiltonian are given by

$$|\Psi_{j,\mathbf{n}}^\pm\rangle = \phi_j^\mathbf{n}(\mathbf{r})|\mathbf{u}_j^\pm(\mathbf{r}), \pm_j\rangle, \quad (2.3)$$

where $j = \text{CB, HH, LH, SO}$ is the band index and \pm distinguishes between the two states of each band which are degenerate in the bulk system. The basis functions of H_K consist of s - and p -symmetric Bloch states $|\mathbf{u}_j^\pm(\mathbf{r})\rangle$ in the CB and VB, respectively, and spin states $|\pm_j\rangle$. The envelopes are given by the three-dimensional eigenfunctions of the harmonic confinement potential V_{conf} , $\phi_j^\mathbf{n}(\mathbf{r})$, with $\mathbf{n} = (n_x, n_y, n_z)$ being a vector of the according quantum numbers. Motivated by the large energy splittings in quantum dots we choose $n_x, n_y, n_z \in \{0, 1\}$. We approximately block-diagonalize the complete Hamiltonian $H = H_K + V_{\text{conf}} + H_\varepsilon$ in the HH subspace by a Schrieffer-Wolff transformation $\tilde{H} = e^{-A}He^A$. The eigenstates of the diagonal HH subsystem are determined by

$$|\Psi_{\text{hyb}}\rangle = |\tilde{\Psi}\rangle \simeq (\mathbf{1} - A^{(1)})|\Psi\rangle, \quad (2.4)$$

where $A^{(1)}$ is the anti-Hermitian, block off-diagonal matrix describing the Schrieffer-Wolff transformation to first order. Explicitly, the hybridized eigenstates of the effective 2×2 HH Hamiltonian read

$$|\Psi_{\text{hyb}}^\tau(\varepsilon)\rangle = \mathcal{N} \sum_{j,\mathbf{n},\tau'} \lambda_{j,\mathbf{n}}^{\tau',\tau}(\varepsilon) |\Psi_{j,\mathbf{n}}^{\tau'}\rangle, \quad (2.5)$$

$\tau, \tau' = \pm$, with $\lambda_{j,\mathbf{n}}^{\tau',\tau}(\varepsilon) = \langle \Psi_{j,\mathbf{n}}^{\tau'} | H | \Psi_{\text{HH},\mathbf{0}}^\tau \rangle / (E_{j,\mathbf{n}} - E_{\text{HH},\mathbf{0}})$ being overlap matrix elements, where H and $E_{j,\mathbf{n}}$ introduce the strain dependence. $E_{j,\mathbf{n}}$ is the eigenenergy of the state $|\Psi_{j,\mathbf{n}}^{\tau'}\rangle$ and \mathcal{N} ensures proper normalization. In the zero strain case we find for $|\Psi_{\text{hyb}}^\tau(0)\rangle$ the leading coefficients $|\lambda_{\text{CB},(0,1,0)}^{\tau,\tau}(0)| = |\lambda_{\text{CB},(1,0,0)}^{\tau,\tau}(0)| \simeq 0.11$, $|\lambda_{\text{LH},(0,1,1)}^{\tau,\tau}(0)| = |\lambda_{\text{LH},(1,0,1)}^{\tau,\tau}(0)| \simeq 0.097$, and $|\lambda_{\text{SO},(0,1,1)}^{\tau,\tau}(0)| = |\lambda_{\text{SO},(1,0,1)}^{\tau,\tau}(0)| \simeq 0.031$. For all configurations, $\lambda_{\text{HH},\mathbf{0}}^{\tau,\tau}(\varepsilon) = 1$. The system parameters used in the calculations are listed in Table 2.1.

E_g	0.418 eV [6]	D_d	1.0eV [108]
m'	0.026 m_0	D_u	2.7 eV [6]
P	9.197 eVÅ[6]	D'_u	3.18 eV [6]
γ_1	20.0 [108]	C_4	11.3 eVÅ [109]
γ_2	8.5 [108]	C'_5	18.4 eVÅ [109]
γ_3	9.2 [108]		
α	0.666	a_{InAs}	6.058 Å[6]

Tabelle 2.1: Values of InAs parameters we use as input for the 8×8 Hamiltonian $H_K + V_{\text{conf}} + H_\epsilon$.

2.3 Effective hyperfine Hamiltonian of the heavy-hole spin

The hybridized HH states couple to the k th nucleus by the Fermi contact interaction h_1^k , being non-negligible due to the s -symmetric CB admixtures, the anisotropic hyperfine interaction h_2^k , and the coupling of the orbital angular momentum (OAM) to the nuclear spins h_3^k (see Refs. [62, 64]). We derive an effective, strain-dependent hyperfine Hamiltonian in the HH subspace by taking matrix elements over a single Wigner-Seitz (WS) cell: $H_{\text{eff}}^{\tau, \tau'}(\epsilon) = \sum_k \langle \Psi_{\text{hyb}}^\tau(\epsilon) | \sum_{i=1}^3 h_i^k | \Psi_{\text{hyb}}^{\tau'}(\epsilon) \rangle_{\text{WS}}$, $\tau, \tau' = \pm$. For the numerical evaluation of the matrix elements we model the WS cell as a sphere of radius one half of the In-In atom distance, centered in the middle of the In-As bond. The basis functions of H_K , $|\mathbf{u}_j^\pm(\mathbf{r}), \pm_j\rangle$, are written as products of OAM eigenstates and spin states [6]. We approximate the eigenstates of OAM, S , P^z , and P^\pm , as linear combinations of atomic eigenfunctions [110], $\mathbf{u}_j^\pm(\mathbf{r}) = \alpha \psi_{\text{In}}^{5lm}(\mathbf{r} + \mathbf{d}/2) \pm \sqrt{1 - \alpha^2} \psi_{\text{As}}^{4lm}(\mathbf{r} - \mathbf{d}/2)$, where α is the electron distribution between the two atoms and $\psi^{nlm}(\mathbf{r}) = R_{nl}(r) Y_l^m(\vartheta, \varphi)$ are hydrogenic eigenfunctions with quantum numbers n , l , and m . The radial part of the wave function depends on the effective central charge Z_{eff} of the nuclei where we use values for free atoms [111, 112]. $\mathbf{r} \pm \mathbf{d}/2$ denotes the position of the hole with respect to the nuclei located at $\pm \mathbf{d}/2$ in the WS cell, where $\mathbf{d} = a_{\text{InAs}}(1, 1, 1)/4$ is the InAs bonding vector defined by the lattice constant a_{InAs} . The bonding and anti-bonding character of the VB and CB are expressed by the + and - signs, respectively, and $\int_{\text{WS}} d^3r |\mathbf{u}_j^\pm(\mathbf{r}), \pm_j|^2 = 2$ enforces normalization [63]. The error of this method is small and has been estimated in Ref. [64]. For strain distributions in the vicinity of the realistic strain configuration of a cylindric InAs quantum dot, i.e., $\epsilon_{xx} = \epsilon_{yy} = -0.06$ and $\epsilon_{zz} = 0.06$ (see Ref. [13]), we find an effective hyperfine Hamiltonian of

the form

$$H_{\text{eff}} = (b_z + h^z)S^z + \frac{1}{2}(h^+S^- + h^-S^+). \quad (2.6)$$

Here, the term proportional to $b_z = g_h\mu_B B$ accounts for the Zeeman splitting due to a magnetic field B along the growth direction, with $g_h \simeq 2$ being the HH g factor and μ_B the Bohr magneton. The components of the Overhauser field read $h^{z,\pm} = \sum_k A_k^{z,\pm}(\boldsymbol{\varepsilon})\mathbf{I}_k^{z,\pm}$, where $A^{z,\pm}(\boldsymbol{\varepsilon}) = \sum_i \nu_i A_i^{z,\pm}(\boldsymbol{\varepsilon})$ denote the corresponding strain dependent hyperfine coupling constants weighted by the nuclear abundance ν_i of each atomic species i . \mathbf{S} is the pseudospin 1/2 operator of the hybridized HH states and \mathbf{I}_k is the nuclear spin operator of the k th nucleus. We find for the effective hyperfine coupling

$$A_k^z(\boldsymbol{\varepsilon}) \simeq v_0 A_z(\boldsymbol{\varepsilon}) |\phi_{\text{HH}}^0(\mathbf{r}_k)|^2, \quad (2.7)$$

$$A_k^\pm(\boldsymbol{\varepsilon}) \simeq \sum_{j,j',\mathbf{n},\mathbf{n}'} v_0 A_{\pm,j,j'}(\boldsymbol{\varepsilon}) \phi_j^{\mathbf{n}}(\mathbf{r}_k)^* \phi_{j'}^{\mathbf{n}'}(\mathbf{r}_k), \quad (2.8)$$

where v_0 is the volume occupied by a single nucleus. $A_z(\boldsymbol{\varepsilon})$ and $A_{\pm,j,j'}(\boldsymbol{\varepsilon})$ are the hyperfine coupling strengths and are given by $\mathbf{A}_{j,j'}(\boldsymbol{\varepsilon}) \cdot \mathbf{I}^k = \sum_{\kappa,\kappa'} (\lambda_{j,\mathbf{n}}^{\kappa,\tau}(\boldsymbol{\varepsilon}))^* \lambda_{j',\mathbf{n}'}^{\kappa',\tau'}(\boldsymbol{\varepsilon}) \langle \mathbf{u}_j^{\kappa}(\mathbf{r}), \kappa_j | \sum_{i=1}^3 h_i^k | \mathbf{u}_{j'}^{\kappa'}(\mathbf{r}), \kappa_{j'}' \rangle$, where $\kappa, \kappa' = \pm$ and \mathbf{I}^k is the nuclear spin operator. In Eq. (2.8), we neglect contributions where $A_{\pm,j,j'}(\boldsymbol{\varepsilon})$ is more than one order of magnitude smaller than the leading term. We find $|A_z(\boldsymbol{\varepsilon})| \gg \max|A_{\pm,j,j'}(\boldsymbol{\varepsilon})|$; thus H_{eff} is predominantly of Ising form with additional small pair-flip processes between nuclear and hole spin.

2.4 Effect of strain on the heavy-hole spin dynamics

For a Hamiltonian of the form of H_{eff} , the time evolution of the $S^+(t)$ component and hence the decoherence of the HH pseudospin state is described by the Nakajima-Zwanzig master equation [67]. We obtain an algebraic form in the rotating frame with frequency ω_n by performing a Laplace transform, $f(s) = \int_0^\infty f(t)e^{-st}dt$, $\text{Re}[s] > 0$, yielding

$$S^+(s + i\omega_n) = \frac{\langle S^+ \rangle_0}{s + \Sigma(s + i\omega_n)}. \quad (2.9)$$

Here $\langle S^+ \rangle_0 = \text{Tr} S^+ \rho$ with density operator ρ and $\Sigma(s)$ is the Laplace-transformed memory kernel which describes the dynamics of S^+ and is derived in Refs. [67, 113]. The Zeeman splitting ω_n is determined by the eigenvalue equation $\omega_n |n\rangle = (b_z + h^z)|n\rangle = (g_h\mu_B B + pA_z(\boldsymbol{\varepsilon})I)|n\rangle$, where p

($|p| \leq 1$) is the polarization of the nuclear spins in the positive z direction, and $|n\rangle$ is a narrowed nuclear spin state [67]. The exact Eq. (2.9) can only be solved perturbatively by expanding $\Sigma(s)$ in powers of the flip-flop processes $V = (h^+S^- + h^-S^+)/2$. This is possible since the energy scale of V is much smaller than the one associated with the Ising term $\sim h^z$ in Eq. (2.6). Following Ref. [113], we expand $\Sigma(s)$ up to fourth order in V , $\Sigma(s) = \Sigma^{(2)}(s) + \Sigma^{(4)}(s) + \mathcal{O}(V^6)$, where the Zeeman splitting between the HH and nuclear spins forbids processes of odd order. $\Sigma^{(2)}(s)$ and $\Sigma^{(4)}(s)$ are given explicitly in Eqs. (A.4) and (A.5) in Appendix A.2. $\Sigma^{(2)}(s)$ is purely real and hence leads to no decay in Eq. (2.9) but to a frequency shift $\Delta\omega = -\text{Re}[\Sigma^{(2)}(s + i\omega_n)]$. This reflects the fact that energy conservation forbids the real flip of the electron spin, and only virtual flips are possible. The imaginary part of $\Sigma^{(4)}(s)$ yields a decay, resulting in the decoherence rate $1/T_2$ given by the relation $1/T_2 = -\text{Im}[\Sigma^{(4)}(i\omega_n + i\Delta\omega - 0^+)]$, where 0^+ is a positive infinitesimal. $\Sigma^{(2)}(s)$ and $\Sigma^{(4)}(s)$ are evaluated in the continuum limit (see Appendix). We simplify the calculations by averaging over the vertical dependence of the coupling constants $A_k^{z,\pm}(\boldsymbol{\varepsilon})$, which is possible since $a \ll L$. The frequency shift $\Delta\omega$ can be calculated directly, whereas the lengthy calculation of the decoherence rate $1/T_2$ can be found in Appendix A.2. After calculating analogously to Ref. [104] we find ¹

$$\frac{1}{T_2} = \pi \frac{c_+c_-}{4\omega_n^2} \frac{|A_\pm|^4}{|A_z|} \int_\eta^1 dx x [\ln x]^2 (x - \eta) [\ln(x - \eta)]^2, \quad (2.10)$$

where $c_\pm = I(I+1) - \langle\langle m(m \pm 1) \rangle\rangle$ with nuclear spin I and $m = -I, \dots, I$. The brackets $\langle\langle \dots \rangle\rangle$ denote averaging over all eigenvalues m of I_k^z . $\eta(\boldsymbol{\varepsilon}) = \Delta\omega/|A_z| \propto 1/\omega_n$ and $1/T_2$ can be evaluated numerically for any $\eta < 1$. It is evident that the Ising-like form of the Hamiltonian (2.6), which corresponds to $|A_z| \gg |A_\pm|$, prolongs T_2 . The effect of non-zero strain configurations on the hyperfine decoherence rate is clearly visible when comparing with the zero strain case. In Fig. 2.1 we display the decoherence rate $1/T_2$ as a function of the Zeeman energy $\omega_n = g_h\mu_B B + pA_z(\boldsymbol{\varepsilon})I$ for an unstrained dot and different internal strain configurations. The general shape of the decoherence rate remains unchanged for the different strain distributions, but the rate is shifted along the ω_n axis, the width of the peak is altered, and a lowering of the rate's maximum for asymmetric lateral strain is induced. The lower

¹Here, we have corrected an error in the previous calculation [104]. As a consequence of this, the dip in Fig. 1 of Ref. [104] turns out to be an artifact.

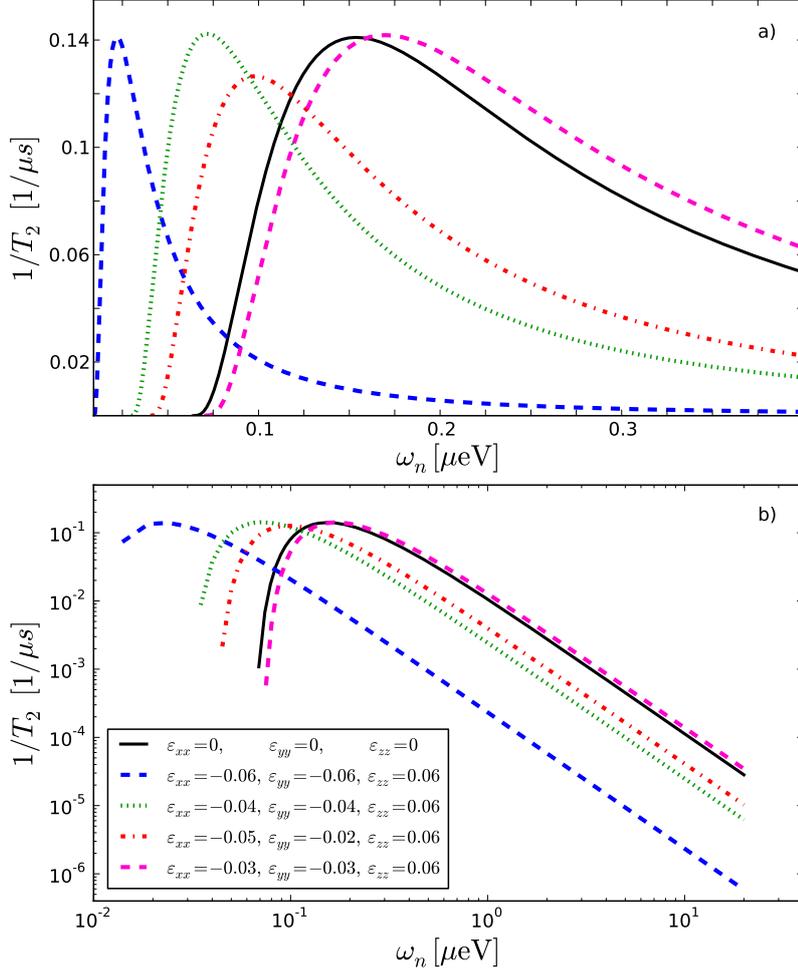


Abbildung 2.1: The decoherence rate $1/T_2$ for different internal strain configurations as a function of the Zeeman energy ω_n . (a) For most configurations the maximum is shifted to the left with respect to the unstrained case except if $\text{Tr } \epsilon \gtrsim \xi$. (b) Large ω_n , i.e., magnetic fields B or polarizations p , cause a power-law decay of $1/T_2$. The legend in the lower panel is valid for both plots and denotes the strain configurations.

bound of the rates on the ω_n axis is determined by $\eta = 1$. The decoherence rate is shifted to the left with respect to the zero-strain curve for $\text{Tr } \epsilon < \xi$ and shifted to the right if $\text{Tr } \epsilon \gtrsim \xi$, respectively, where ξ is a small negative number of $\mathcal{O}(10^{-3})$. The latter relation corresponds to a dominant vertical strain tensor component. When the rate is shifted to the left, the peak becomes more pronounced; hence the sensitivity of $1/T_2$ to changes in the external parameters is increased. The associated hybridized wave functions show a gradual lowering of the admixtures of all leading components with respect to the zero-strain case. A broadening of the peak occurs when the curve is

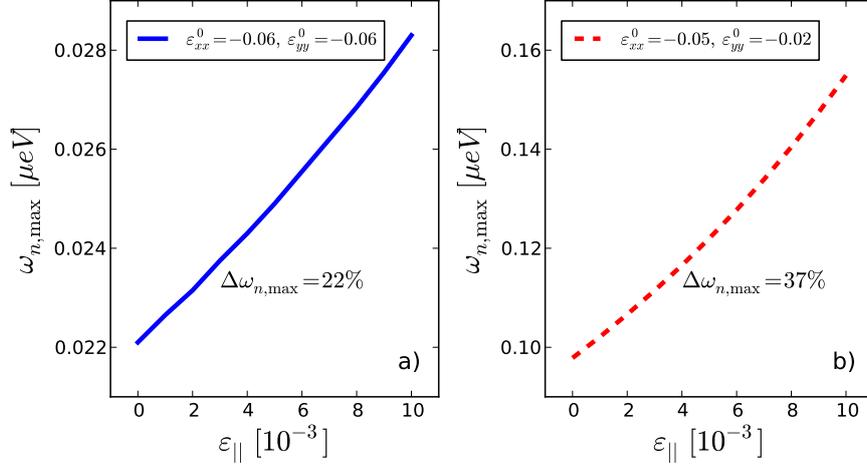


Abbildung 2.2: Shift of the peak of the decoherence rate located at $\omega_{n,\max}$ when external strain ε_{\parallel} up to the breaking limit is applied. In both panels the change is roughly linear. For the asymmetric lateral strain configuration (b) the relative change of $\omega_{n,\max}$ is considerably larger than for the symmetric configuration (a). The legends display the internal strain configurations of the dots, ε_{xx}^0 and ε_{yy}^0 , at $\varepsilon_{\parallel} = 0$. For all configurations we keep $\varepsilon_{zz} = 0.06$ constant.

shifted to the right. Here, the CB admixture of the hybridized wave function is increased while the other admixtures are lowered again. For the chosen dot geometry, $L = 10\text{nm}$ and $a = 2\text{nm}$, the minimal coherence time at the peak of the curves is $T_2 \simeq 7\mu\text{s}$. For large magnetic fields B or polarizations p , the curves decay following a power law as evident in Fig. 2.1b). As a general result, we state that regardless the strain configuration, the decoherence rate $1/T_2$ can be decreased over orders of magnitude by relatively small changes of the external parameters.

The strain fields in a quantum dot can be modified by applying additional strain, e.g., by the technique demonstrated in Ref. [14]. Here, a GaAs sample containing InAs quantum dots is tightly glued on top of a piezoelectric stack, its stretching direction aligned with the $\langle 110 \rangle$ crystal axis, and a voltage is applied. So far, additional strain of about $\varepsilon_{\parallel} \simeq 0.003$ (see Ref. [15]) has been reached whereas the breaking point of GaAs corresponds to a strain of $\varepsilon_{\parallel} \approx 0.012$ (see Ref. [114]). We examine the peak of the decoherence rate located at $\omega_{n,\max}$ which is determined by the implicit, strain-dependent equation

$$\int_{\eta}^1 dx x [\ln x]^2 \ln(x - \eta) \left[\left(\frac{3}{2} \eta - x \right) \ln(x - \eta) + \eta \right] = 0. \quad (2.11)$$

Additional strain alters $\omega_{n,\max}$ significantly, as displayed in Fig. 2.2, and hence inflicts measurable changes on the decoherence rate. The relative shift of the

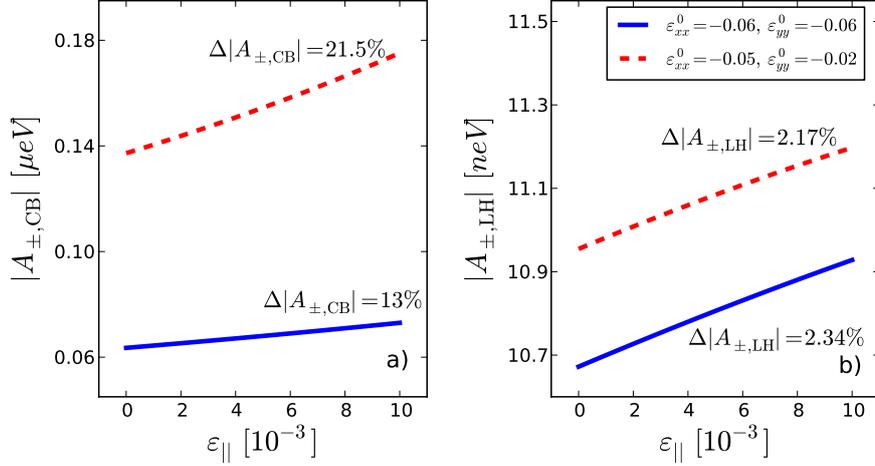


Abbildung 2.3: The largest contributions to the hyperfine coupling as a function of applied external strain ε_{\parallel} . The relative change of the CB coupling (a) is much larger than the change of the LH coupling (b). In the legend the internal strain configurations of the dots, ε_{xx}^0 and ε_{yy}^0 , at $\varepsilon_{\parallel} = 0$ are displayed. Again we keep $\varepsilon_{zz} = 0.06$ constant for all configurations.

peak for the asymmetric lateral strain configuration is about 37%, thus larger than for the symmetric configuration where the shift is 22%. The strain-induced change of the decoherence rate is directly connected to variances in the magnitude of the coupling strengths $A_z(\varepsilon)$ and $A_{\pm,j,j'}(\varepsilon)$. In Fig. 2.3 we display the dependence of the absolute values of the dominant coupling strengths on applied strain ε_{\parallel} . We find that the relative change of $A_{\pm,CB}$, ranging up to 21.5%, is the largest of all whereas the relative change of $A_{\pm,LH}$ is only about 2%. The Ising-like coupling A_z (not on display) changes less than 1% and thus is negligible. From this we deduce that the strain-induced changes of the decoherence rate can be attributed mainly to the difference in the CB admixture of the hybridized HH states. Hence the usually neglected contribution of the CB to the hole spin dephasing is of significance.

2.5 Summary

In conclusion, we investigated the dynamics of hybridized HH spin states confined to self-assembled and hence strained semiconductor quantum dots. By taking into account hyperfine interaction between these states and the surrounding nuclei an effective, strain-dependent Hamiltonian was found, which is, for realistic strain configurations, predominantly of Ising form. The time evolution of its S^+ component was derived for a narrowed nuclear spin state,

and we have shown that the internal strain fields of self-assembled quantum dots affect the decoherence rate $1/T_2$ significantly. For all strain configurations, $1/T_2$ was found to be tunable over orders of magnitude by adjusting external parameters. Different strain fields were shown to cause a shift of the dependence of $1/T_2$ on external parameters ω_n and to change the non-monotonicity of the peak. Additional application of external strain inflicted measurable changes upon $1/T_2$ which could mostly be attributed to large alterations in the effective hyperfine coupling of the CB admixture. This finding indicated the importance of the CB admixture of the hybridized HH states regarding the sensitivity of $1/T_2$ on strain.

Acknowledgments

We thank Dimitrije Stepanenko and Richard J. Warburton for helpful discussions. This work has been supported by the Swiss SNF, NCCR Nanoscience, NCCR QSIT, and DARPA.

Tunable g factor and phonon-mediated hole spin relaxation in Ge/Si nanowire quantum dots

Adapted from:

F. Maier, C. Klöffel and D. Loss,

'Tunable g factor and phonon-mediated hole spin relaxation in Ge/Si nanowire quantum dots',

Phys. Rev. B **87**, 161305(R) (2013).

We theoretically consider g factor and spin lifetimes of holes in a longitudinal Ge/Si core/shell nanowire quantum dot that is exposed to external magnetic and electric fields. For the ground states, we find a large anisotropy of the g factor which is highly tunable by applying electric fields. This tunability depends strongly on the direction of the electric field with respect to the magnetic field. We calculate the single-phonon hole spin relaxation times T_1 for zero and small electric fields and propose an optimal setup in which very large T_1 of the order of tens of milliseconds can be reached. Increasing the relative shell thickness or the longitudinal confinement length further prolongs T_1 . In the absence of electric fields, the dephasing vanishes and the decoherence time T_2 is determined by $T_2 = 2T_1$.

Semiconducting nanowires (NWs) allow to create nanoscale systems defined precisely regarding composition, geometry, and electronic properties and hence are subject to great experimental efforts. Furthermore, they offer new ways for implementing spin-based quantum computation [29]. Both III-V compounds and group-IV materials are considered and operated in the conduction band (CB, electrons) [24, 115–121] and in the valence band (VB, holes) [122–134] regime. A particularly favored material is InAs, where single-electron quantum dots (QDs) [24] and electrically controlled spin rotations [117, 118, 120] have been implemented. Recently, qubits have also been implemented in InSb NW QDs [119, 121, 134], a system for which extremely large electron g factors have been found [116, 119]. However, the strong hyperfine interaction in InAs and InSb is considered the dominant source for the short coherence times observed [117, 121]. The latter may therefore be substantially prolonged in group-IV NWs that can be grown nuclear-spin-free. In this context, Ge and Si have emerged as promising materials for nanoscale systems such as lateral QDs [135–138], self-assembled QDs [139–141], cylindrical core/shell NWs [122–132], and ultrathin, triangular NWs [133].

For applications in spintronics and quantum information processing, it can be advantageous to consider holes instead of electrons. Due to the p -wave symmetry of the Bloch states, holes experience a strong spin-orbit interaction (SOI) on the atomic level leading to an effective spin $J = 3/2$ behavior. Hence spin and momentum are coupled strongly which allows efficient control of the hole spin by electrical means. Furthermore, hole spin lifetimes are prolonged in the presence of confinement [33, 60, 64, 102–104].

In Ge/Si core/shell NWs, the large VB offset leads to an accumulation of holes in the core [123, 142]. They form a one-dimensional (1D) hole gas with an unusually large, tunable Rashba-type SOI, referred to as direct Rashba SOI (DRSOI) [23]. This DRSOI makes Ge/Si core/shell NWs attractive candidates for quantum information processing via electric-dipole induced spin resonance, [52] and we mention that signatures of a tunable Rashba SOI were already deduced from magnetotransport experiments [129]. Experiments on gate defined QDs in this system revealed an anisotropy and confinement dependence of the g factor [127, 128]. Recently, singlet-triplet relaxation times in the range of several hundred microseconds were measured [132].

In this chapter, we consider holes forming qubits in the energetically lowest states of longitudinal QDs in Ge/Si core/shell NWs. We find the effective g factor g_{eff} of this subsystem which turns out to be strongly anisotropic and tunable by choosing the direction and magnitude of applied electric

fields. For small electric fields, we perturbatively derive an effective subspace Hamiltonian and the according hole-spin-phonon coupling and calculate the hole-spin relaxation rate T_1^{-1} . At small Zeeman splittings $\hbar\omega$ we observe a $\omega^{7/2}$ -proportionality of T_1^{-1} which contrasts the ω^5 behavior found for electrons in QDs [21, 59, 143–146]. The magnitude of T_1^{-1} depends strongly on the direction of the magnetic field with respect to the wire. For zero electric field, aligning the magnetic field perpendicular to the wire results in very long T_1 of the order of tens of milliseconds. Directing the magnetic field along the wire results in a much shorter T_1 . For both configurations, the dephasing is zero, hence the decoherence time is given by $T_2 = 2T_1$. Applying small electric fields can enhance the relaxation rate by several orders of magnitude. This effect depends strongly on the direction of the electric field with respect to the magnetic field. Long T_1 in the presence of electric fields are obtained when electric and magnetic fields are perpendicular to each other and perpendicular to the wire. Moreover, we find that T_1 can be prolonged further by increasing the relative shell thickness and the longitudinal QD confinement. Thus, we predict an optimal field geometry for spin qubits in Ge/Si NWs that can be tested experimentally.

Low-energetic hole states in a cylindrical Ge/Si core/shell NW are well described by an effective 1D Hamiltonian [23]

$$H_w = H_0 + H' \quad (3.1)$$

that can be split into a leading order term H_0 and a perturbation H' ,

$$H_0 = H_{\text{LK}_d} + H_{\text{strain}} + H_{B,Z}, \quad (3.2)$$

$$H' = H_{\text{LK}_{od}} + H_R + H_{\text{DR}} + H_{B,\text{orb}}. \quad (3.3)$$

Using the notation introduced in Ref. [23] and defining the z axis as the NW axis (see Fig. 3.1), the diagonal terms of the Luttinger-Kohn (LK) Hamiltonian and the strain-induced energy splitting read

$$H_{\text{LK}_d} + H_{\text{strain}} = A_+(k_z, \gamma) + A_-(k_z, \gamma)\tau_z. \quad (3.4)$$

Here, τ_i and σ_i are the Pauli matrices for band index ($\{g, e\}$) and spin block ($\{+, -\}$) of the basis states $g_{\pm}(x, y)$ and $e_{\pm}(x, y)$ that provide the transverse motion. In Eq. (3.4), we defined $A_{\pm}(k_z, \gamma) \equiv \hbar^2 k_z^2 (m_g^{-1} \pm m_e^{-1})/4 \pm \Delta/2$, with $m_g \simeq m_0/(\gamma_1 + 2\gamma_s)$ and $m_e = m_0/(\gamma_1 + \gamma_s)$ as the effective masses along z . Here, γ_1 and γ_s are the Luttinger parameters in spherical approximation and m_0 denotes the bare electron mass. For Ge, $\gamma_1 = 13.35$ and $\gamma_s = 5.11$ [147].

$\Delta \equiv \Delta_{\text{LK}} + \Delta_{\text{strain}}(\gamma)$ is the level splitting between the g_{\pm} and e_{\pm} states, $\gamma \equiv (R_s - R)/R$ is the relative shell thickness, and R (R_s) is the core (shell) radius. The Zeeman coupling $H_{B,Z}$ with splitting $\hbar\omega_{B,Z}$ in the lowest-energy subspace (g band) is determined by the magnetic field $\mathbf{B} = (B_x, 0, B_z) \equiv |\mathbf{B}|(\sin\theta, 0, \cos\theta)$ (Fig. 3.1), where we set $B_y = 0$ due to cylindrical symmetry. The main contributions to H' are

$$H_{\text{LK}_{\text{od}}} = Ck_z\tau_y\sigma_x, \quad (3.5)$$

$$H_{\text{DR}} = eU(E_x\tau_x\sigma_z - E_y\tau_y), \quad (3.6)$$

where $H_{\text{LK}_{\text{od}}}$ features the off-diagonal couplings with coupling constant $C = 7.26\hbar^2/(m_0R)$ provided by the LK Hamiltonian as a consequence of the strong atomic level SOI. H_{DR} is the DRSOI that results from direct, dipolar coupling to an electric field $\mathbf{E} = (E_x, E_y, 0)$, where $U = 0.15R$. We note that $\hbar k_z = -i\hbar\partial_z$ in Eqs. (3.4) and (3.5) is the momentum operator along the wire. In the absence of longitudinal confinement the wave functions along z are of type $e^{ik_z z}$ with k_z as the wave number. H_{R} is the conventional Rashba SOI, and, although fully taken into account in the present analysis, turns out to be negligible for the typical parameters and electric fields considered here. Finally, $H_{B,\text{orb}}$ denotes the orbital coupling to the magnetic field. Details on all elements of H_0 and H' are provided in Ref. [23] and in Eqs. (B.1)-(B.7) in Appendix B.1.

We proceed with the derivation of an effective 1D Hamiltonian $H_{\text{h-ph}}$ for the coupling between low-energetic holes and acoustic phonons. There are three different types of acoustic phonon modes in cylindric NWs: torsional, dilatational, and flexural [57]. We find four different modes λ with dispersion relation $\omega_{\lambda}(q)$, where q is the phonon wave number along the wire and the exact form of ω_{λ} depends strongly on the shell thickness. For the torsional and dilatational mode ($\lambda = T, L$) ω_{λ} depends linearly on q , whereas for the two flexural modes ($\lambda = F_{\pm 1}$) this dependence is quadratic. The detailed derivation will be published elsewhere; in this chapter we directly apply the displacement field $\mathbf{u}(\mathbf{r}, t) = \sum_{\lambda, q} [\mathbf{u}_{\lambda}(q, \mathbf{r}, t)b_{q, \lambda}(t) + \text{H.c.}]$ obtained for a finite shell following Refs. [56, 57, 148]. Here, $b_{q, \lambda}(t) = e^{-i\omega_{\lambda}(q)t}b_{q, \lambda}$ is the time-dependent phonon annihilation operator. To derive $H_{\text{h-ph}}$, we insert the associated strain tensor components $\varepsilon_{ij}(\mathbf{r}, t)$ in the Bir-Pikus Hamiltonian [149],

$$H_{\text{BP}} = b \left[\sum_i \varepsilon_{ii} J_i^2 + 2(\varepsilon_{xy} \{J_x, J_y\} + \text{c.p.}) \right], \quad (3.7)$$

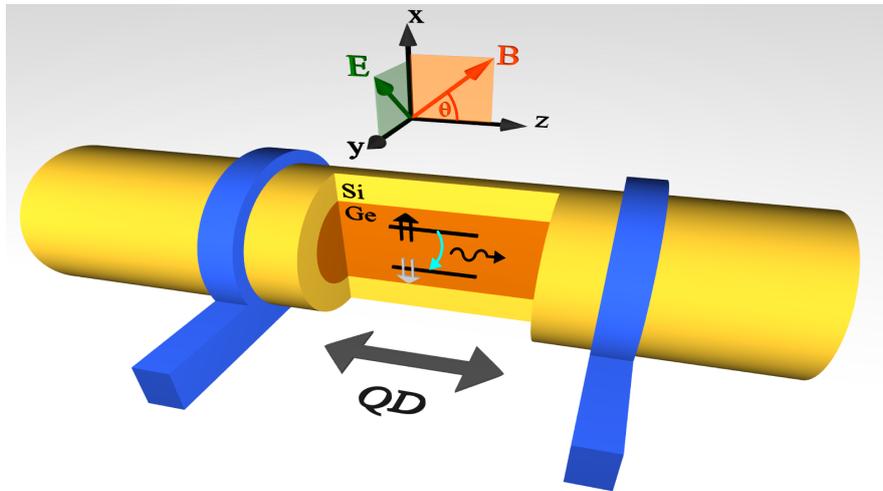


Abbildung 3.1: Sketch of a Ge/Si core/shell NW aligned with the z axis of the coordinate system. Electric gates (blue) induce confinement along the z axis and define a QD. The electric field \mathbf{E} lies perpendicular to the wire in the xy plane and the magnetic field \mathbf{B} lies in the xz plane.

where we omitted the global shift in energy and used the spherical approximation. The J_i , $i = x, y, z$, are the effective spin-3/2 operators of the VB electrons and the anti-commutator is defined as $\{A, B\} = (AB + BA)/2$. For Ge, the deformation potential b takes the value $b \simeq -2.5$ eV [149]. We finally obtain

$$H_{\text{h-ph}} = \sum_{\lambda} H_{\lambda} = H_{\text{T}} + H_{\text{L}} + H_{F_{+1}} + H_{F_{-1}} \quad (3.8)$$

by integrating out the transverse part of the matrix elements, i.e., by projecting the Hamiltonian onto the subspace spanned by g_{\pm} and e_{\pm} . The components of $H_{\text{h-ph}}$ are given explicitly in Eqs. (B.8)-(B.11) in Appendix B.2.

Longitudinal confinement is realized by electric gating (see Fig. 3.1), which is modeled by adding a harmonic confinement potential in the z direction,

$$H_{qd} = H_w + V_c(z), \quad (3.9)$$

where $V_c(z) = \frac{1}{2}\alpha_c z^2$. H_{qd} describes the QD well if the longitudinal confinement length is much larger than R . The basis states of H_{qd} are products of type $g_{\pm}\psi_m^g$ and $e_{\pm}\psi_m^e$, where the $\psi_m^{g/e}(z)$ are eigenfunctions of the harmonic oscillator $\hbar^2 k_z^2 / (2m_{g/e}) + V_c(z)$ and $m \in \{0, 1, \dots\}$ is the harmonic oscillator quantum number. The confinement energies $\hbar\omega_{g/e}$ relate to α_c via $\alpha_c = m_{g/e}\omega_{g/e}^2$ and the harmonic oscillator confinement lengths read $z_{g/e} = \sqrt{\hbar/(m_{g/e}\omega_{g/e})}$.

From H_{qd} we extract the effective g factor g_{eff} of the lowest-energy subsystem by performing an exact, numerical diagonalization which gives the

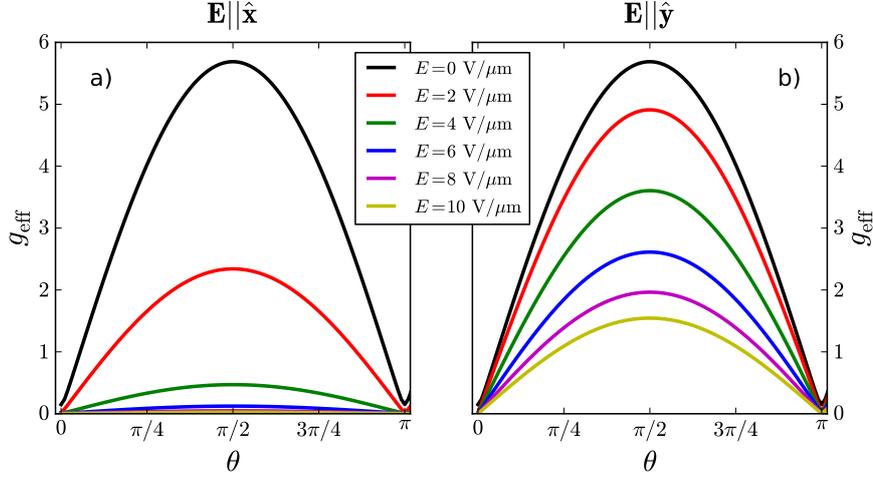


Abbildung 3.2: Effective g factor g_{eff} as a function of the angle θ defined by $\mathbf{B} = |\mathbf{B}|(\sin \theta, 0, \cos \theta)$ for $\mathbf{E} \parallel \hat{\mathbf{x}}$ (a) and $\mathbf{E} \parallel \hat{\mathbf{y}}$ (b). We vary $|\mathbf{E}|$ from 0 to 10 V/ μm . For $|\mathbf{E}| = 0$, we find $g_{\text{eff}}(0) \approx 0.14$ and $g_{\text{eff}}(\pi/2) \approx 5.7$. It is clearly visible that g_{eff} is affected much stronger by changes in $|\mathbf{E}|$ for $\mathbf{E} \parallel \hat{\mathbf{x}}$ than for $\mathbf{E} \parallel \hat{\mathbf{y}}$. Even though the curves in (a) seem to overlap for $|\mathbf{E}| \geq 6$ V/ μm , $g_{\text{eff}}(\pi/2)$ still decreases for growing fields and g_{eff} remains anisotropic. We choose $R = 10$ nm and $R_s = 13$ nm for the NW and a QD confinement length of $z_g \approx 80$ nm.

Zeeman splitting $\Delta E_{Z,\text{num}}$ (defined as positive) and

$$g_{\text{eff}} = \frac{\Delta E_{Z,\text{num}}}{\mu_B |\mathbf{B}|}, \quad (3.10)$$

where μ_B denotes the Bohr magneton. In Fig. 3.2, we plot g_{eff} as a function of the angle θ , for both $\mathbf{E} \parallel \hat{\mathbf{x}}$ and $\mathbf{E} \parallel \hat{\mathbf{y}}$. In both cases, g_{eff} is highly anisotropic and tunable over a wide range of values by adjusting the magnitude of \mathbf{E} . The tunability is caused by two mechanisms which occur in the system for large $|\mathbf{E}|$. The admixture of the e_{\pm} states to the effective lowest-energy subsystem increases while the spin-orbit length l_{SOI} decreases. For very small l_{SOI} ($l_{\text{SOI}} \ll z_g$), the hole spin flips many times while moving through the QD and the resulting g_{eff} starts to average out. The tunability is much stronger for $\mathbf{E} \parallel \hat{\mathbf{x}}$ than for $\mathbf{E} \parallel \hat{\mathbf{y}}$. Note that g_{eff} is also tunable by varying $V_c(z)$. We find good agreement with the results given in Ref. [132], where $g_{\text{exp}} \approx 1.02$ was measured for \mathbf{B} aligned with the NW with an accuracy of $\sim 30^\circ$. We note, however, that clearly different results for g can be expected in QDs with very large occupation number, i.e., when the hole-spin qubits are formed in an excited band.

In the following, we are interested in the dynamics of the lowest-lying, Zeeman split states which we decouple perturbatively from the higher-energy

states. This is done by two consecutive Schrieffer-Wolff transformations (SW-Ts) to account for the two different energy scales Δ and $\hbar\omega_g$. The general form of the SWT is $\tilde{H} = e^{-S} H e^S$, where to lowest order $S \approx S_1$. We first remove the coupling between the g_{\pm} and e_{\pm} states in the effective 1D picture using S_1^g . The hole-phonon coupling then transforms according to $H_{\text{h-ph}} - [S_1^g, H_{\text{h-ph}}]$ and we refer to its projection on g_{\pm} as $H_{\text{h-ph}}^g$. In the second step, we add harmonic confinement as introduced above and decouple the two lowest, Zeeman split states $|0\rangle \equiv \{|\uparrow\rangle, |\downarrow\rangle\}$ by another SWT using $S_1^{(0)}$. A necessary condition for this approach is that the energy splittings obey $\Delta \gg \hbar\omega_g \gg \hbar\omega_{B,Z}$, and the magnitude of \mathbf{E} is restricted by $2C|\mathbf{E}|eU/(z_g\Delta) \ll \hbar\omega_g$. The latter condition is fulfilled for $|\mathbf{E}| \ll 1 \text{ V}/\mu\text{m}$. We obtain an effective Zeeman term $H_{Z,\text{eff}} = \mu_B \mathbf{B}_{\text{eff}} \cdot \boldsymbol{\sigma}$ with Zeeman splitting $\Delta E_{Z,\text{eff}} = 2\mu_B |\mathbf{B}_{\text{eff}}|$, where $\boldsymbol{\sigma}$ is a vector of Pauli matrices. The effective hole spin phonon coupling is obtained by taking

$$H_{\text{s-ph}} = H_{\text{h-ph}}^g - [S_1^{(0)}, H_{\text{h-ph}}^g], \quad (3.11)$$

where $H_{\text{h-ph}}^g$ is now written in the basis given by the confinement. Projecting $H_{\text{s-ph}}$ on $|0\rangle$ results in an effective coupling $H_{\text{s-ph,eff}} = \mu_B \delta\mathbf{B} \cdot \boldsymbol{\sigma}$ with the fluctuating magnetic field $\delta\mathbf{B}(t) = \sum_{\lambda,q} [\mathbf{a}_{\lambda}(q) b_{q,\lambda}(t) + \text{H.c.}]$. The effective subspace Hamiltonian then reads

$$H_{\text{eff}} = H_{Z,\text{eff}} + H_{\text{s-ph,eff}} = \mu_B (\mathbf{B}_{\text{eff}} + \delta\mathbf{B}(t)) \cdot \boldsymbol{\sigma}. \quad (3.12)$$

The spin relaxation rate in the Born-Markov approximation is given by the Bloch-Redfield approach [59, 150, 151]

$$\frac{1}{T_1} = n_i n_j \left[\delta_{ij} (\delta_{pq} - n_p n_q) J_{pq}^+(\omega) - (\delta_{ip} - n_i n_p) J_{pj}^+(\omega) - \delta_{ij} \varepsilon_{kpq} n_k I_{pq}^-(\omega) + \varepsilon_{ipq} n_p I_{qj}^-(\omega) \right], \quad (3.13)$$

where summation over repeated indices is assumed, $\mathbf{n} = \mathbf{B}_{\text{eff}}/|\mathbf{B}_{\text{eff}}|$ is the unit vector in direction of the effective magnetic field, and $\hbar\omega = \hbar\omega_{Z,\text{eff}} = \Delta E_{Z,\text{eff}}$ is the energy splitting of the considered states. Here, $J_{ij}^+(\omega) = \text{Re}[J_{ij}(\omega) + J_{ij}(-\omega)]$ and $I_{ij}^-(\omega) = \text{Im}[J_{ij}(\omega) - J_{ij}(-\omega)]$, with $J_{ij}(\omega) = (\mu_B/\hbar)^2 \int_0^\infty dt e^{-i\omega t} \langle \delta B_i(0) \delta B_j(t) \rangle$ denoting the spectral function.

In Fig. 3.3, we display T_1^{-1} for $|\mathbf{E}| = 0$ and two different directions of \mathbf{B} with respect to the wire, $\mathbf{B} \parallel \hat{z}$ and $\mathbf{B} \parallel \hat{x}$. In this case, the spin-phonon coupling $H_{\text{s-ph,eff}}$ depends only on the coupling terms of $H_{B,\text{orb}}$. For low $\omega_{Z,\text{eff}}$, i.e., the long wavelength regime ($qz_g \ll 1$), both curves are proportional to $\omega_{Z,\text{eff}}^{7/2}$. This behavior is valid for low temperatures ($\hbar\omega_{Z,\text{eff}} \gg k_B T$) and will be replaced

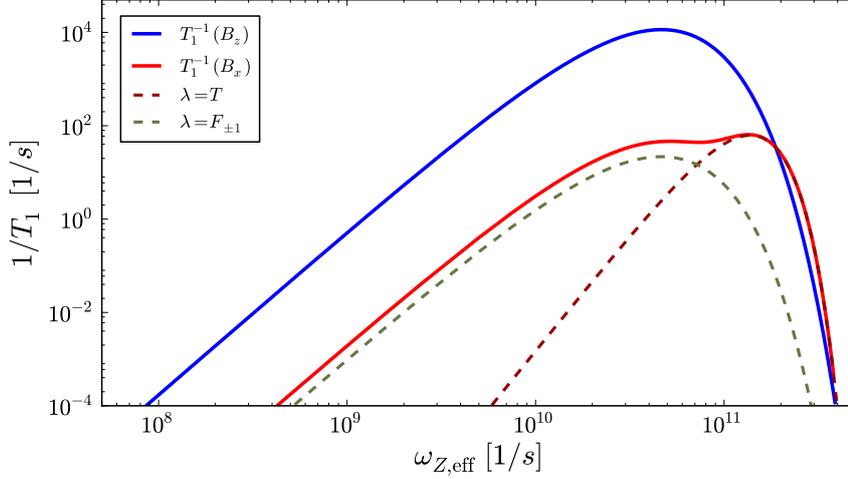


Abbildung 3.3: Relaxation rate T_1^{-1} at $|\mathbf{E}| = 0$ for $\mathbf{B}\|\hat{\mathbf{x}}$ (red, solid) and $\mathbf{B}\|\hat{\mathbf{z}}$ (blue, solid). For $\mathbf{B}\|\hat{\mathbf{x}}$, we plot the contributing phonon branches $F_{\pm 1}$ and T (dashed). We find maximal values $T_{1,\max}^{-1}(\mathbf{B}\|\hat{\mathbf{z}}) \approx 11 \text{ ms}^{-1}$ and $T_{1,\max}^{-1}(\mathbf{B}\|\hat{\mathbf{x}}) \approx 60 \text{ s}^{-1}$. Note the non-monotonic behavior of T_1^{-1} as a function of $\omega_{Z,\text{eff}}$. The NW and QD parameters are chosen as in Fig. 3.2.

by $T_1^{-1} \propto \omega_{Z,\text{eff}}^{5/2} T$ for $\hbar\omega_{Z,\text{eff}} \ll k_B T$. The $\omega_{Z,\text{eff}}^{7/2}$ scaling contrasts the $\omega_{Z,\text{eff}}^5$ behavior of electrons in QDs [21, 59, 143–146]. For $\mathbf{B}\|\hat{\mathbf{z}}$, only the $F_{\pm 1}$ modes contribute significantly to T_1^{-1} . When directing $\mathbf{B}\|\hat{\mathbf{x}}$, the $F_{\pm 1}$ contributions dominate for low $\omega_{Z,\text{eff}}$ and, for the chosen QD geometry, are replaced by a dominating T contribution at $|\mathbf{B}| \approx 150 \text{ mT}$ (Fig. 3.3, dashed). This results in a double peak whose relative height can be modified by changing z_g or R and R_s . Most remarkably, for $\mathbf{B}\|\hat{\mathbf{x}}$, T_1^{-1} is several orders of magnitude smaller than for $\mathbf{B}\|\hat{\mathbf{z}}$. For the chosen QD geometry, T_1^{-1} reaches maximal values $T_{1,\max}^{-1}(\mathbf{B}\|\hat{\mathbf{x}}) \approx 60 \text{ s}^{-1}$ and $T_{1,\max}^{-1}(\mathbf{B}\|\hat{\mathbf{z}}) \approx 11 \text{ ms}^{-1}$. These rates are, depending on the direction of \mathbf{B} , comparable to or much smaller than for electrons in InAs NW QDs [143].

Considering non-zero electric fields, we plot T_1^{-1} for $\mathbf{E}\|\hat{\mathbf{x}}$ again for $\mathbf{B}\|\hat{\mathbf{z}}$ and $\mathbf{B}\|\hat{\mathbf{x}}$ (Fig. 3.4). We add the corresponding curves for $|\mathbf{E}| = 0$ (Fig. 3.4, dashed) to allow for comparison. For both orientations of \mathbf{B} , T_1^{-1} is enhanced significantly for larger $\omega_{Z,\text{eff}}$. This is due to phonons of the L mode coupling $|\uparrow\rangle$ and $|\downarrow\rangle$ via a combination of $H_{LK_{\text{od}}}$ and H_{DR} which dominates H_{R} . Due to cylindrical symmetry, applying $\mathbf{E}\|\hat{\mathbf{y}}$ for $\mathbf{B}\|\hat{\mathbf{z}}$ results in the same effect as described for $\mathbf{E}\|\hat{\mathbf{x}}$. Remarkably, in stark contrast to $\mathbf{E}\|\mathbf{B}\|\hat{\mathbf{x}}$, only minor changes with respect to the curve at $|\mathbf{E}| = 0$ (Fig. 3.4, dotted) are observed when $\mathbf{E}\|\hat{\mathbf{y}}$ and $\mathbf{B}\|\hat{\mathbf{x}}$ (Fig. 3.4, dashed). In the latter case, the dominant contributions of $H_{\text{s-ph,eff}}$ are already present in $H_{\text{s-ph,eff}}$ for $|\mathbf{E}| = 0$.

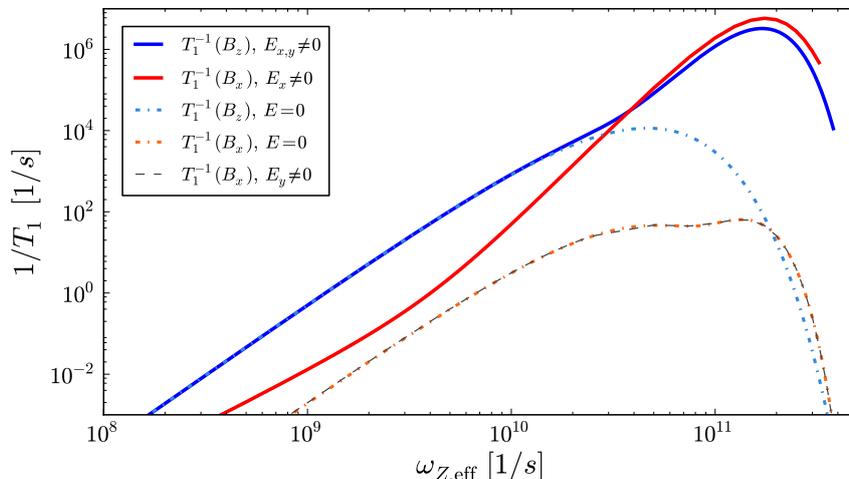


Abbildung 3.4: Relaxation rates T_1^{-1} for $\mathbf{E} \parallel \hat{\mathbf{x}}$ with $|\mathbf{E}| = 0.1 \text{ V}/\mu\text{m}$ for $\mathbf{B} \parallel \hat{\mathbf{x}}$ (red, solid) and $\mathbf{B} \parallel \hat{\mathbf{z}}$ (blue, solid). For comparison we plot T_1^{-1} at $|\mathbf{E}| = 0$ (dotted). We find maximal values $T_{1,\text{max}}^{-1}(\mathbf{B} \parallel \hat{\mathbf{z}}) \approx 3.2 \mu\text{s}^{-1}$, $T_{1,\text{max}}^{-1}(\mathbf{B} \parallel \hat{\mathbf{x}}) \approx 5.8 \mu\text{s}^{-1}$. Rotating the electric field so that $\mathbf{E} \parallel \hat{\mathbf{y}}$ yields the same curve for $\mathbf{B} \parallel \hat{\mathbf{z}}$. Remarkably, for $\mathbf{B} \parallel \hat{\mathbf{x}}$ almost no difference between the curves at $\mathbf{E} \parallel \hat{\mathbf{y}}$ (dashed) and $|\mathbf{E}| = 0$ (dotted) is observed. We use the NW and QD parameters given below Fig. 3.2.

In both cases, $|\mathbf{E}| = 0$ and $|\mathbf{E}| \neq 0$, increasing the relative shell thickness γ shifts the T_1^{-1} curves to slightly larger $\omega_{Z,\text{eff}}$ and lowers the peak height, e.g., increasing γ from 0.3 to 0.7 reduces T_1^{-1} by a factor $\simeq 3$. However, decreasing (increasing) R and R_s while keeping γ constant has no substantial effect on T_1^{-1} aside from slight shifts to the right (left) on the $\omega_{Z,\text{eff}}$ axis. Additionally, enhancing the confinement length z_g lowers $T_{1,\text{max}}^{-1}$ since the short wavelength regime is reached for smaller $\omega_{Z,\text{eff}}$. This effect is quite large, for instance raising z_g from 60 to 100 nm tunes $T_{1,\text{max}}^{-1}$ by factors between 10 and 100. From this analysis we conclude that there exist optimal configurations of \mathbf{B} and \mathbf{E} in order to obtain long T_1 in this type of NW QD. \mathbf{B} should be applied perpendicular to the NW and the optional \mathbf{E} should lie perpendicular to both \mathbf{B} and the NW. For vanishing \mathbf{B} , as pointed out in Ref. [132], two-phonon processes [102] might become relevant.

In the Bloch-Redfield framework, the decoherence time is given by $T_2^{-1} = (2T_1)^{-1} + T_\varphi^{-1}$, where T_φ denotes the dephasing time [59, 151]. For $|\mathbf{E}| = 0$, we find $T_2 = 2T_1$ because the corresponding spectral function is super-ohmic and gives $T_\varphi^{-1} = 0$. For $|\mathbf{E}| \neq 0$ the SOI results in a non-zero dephasing term $T_\varphi^{-1} \neq 0$ and hence $T_2 < 2T_1$.

In conclusion, we have examined effective Zeeman splitting and hole spin dynamics for holes in the lowest VB of a Ge/Si core/shell NW QD. We re-

ported a highly anisotropic effective g factor which is strongly tunable by applying electric fields. We calculated relaxation rates and found configurations of electric and magnetic fields which correspond to very long spin relaxation times. Furthermore we pointed out that the relative shell thickness and the QD confinement length influence the spin relaxation time.

Acknowledgments

We thank Peter Stano for helpful discussions. This work has been supported by SNF, NCCR Nano, NCCR QSIT, DARPA, and IARPA.

Nuclear spin diffusion mediated by heavy hole hyperfine non-collinear interactions

Adapted from:
H. Ribeiro, F. Maier and D. Loss,
*'Nuclear spin diffusion mediated by heavy hole hyperfine
non-collinear interactions'*,
arXiv:1403.0490

We show that the effective hyperfine interaction for heavy-hole states (or any particle described with a p -like Bloch function) can induce non-trivial dynamics of nuclear spins. Experimental evidences can be found, e.g., in self-assembled quantum dots by measuring the saturation of nuclear spin polarization with different orientations of an external magnetic field.

We are currently in the midst of an effort to develop nanostructures that can be used to host qubits. Among the possible architectures [99, 152–154], the progress made with spin-based qubits confined in semiconductor structures [29] has been the most impressive [45]. In only a decade, it became possible to efficiently initialize [155], manipulate [35, 36, 46, 55, 156–158], and measure the state of a single spin confined in both electrically defined and self-assembled quantum dots. All of these remarkable achievements are, however, mitigated by poor coherence times on the order of tens of nanoseconds [35, 46, 55, 156]. In quantum dots made out of III-V materials, nuclear spin fluctuations are the main source of decoherence via the hyperfine interaction [46, 55, 63, 67, 159–162]. Nevertheless, dynamical decoupling schemes have improved the situation and revealed longer dephasing times [40, 163–165].

Like the electron spin, hole states interact with nuclear spins via the hyperfine interaction. The first theories suggested an effective Ising-like type of interaction with a strength on the order of 10% of the one of the electron and with opposite sign [64, 106], which seemed to be experimentally confirmed [65, 66]. However, subsequent experiments seem to contradict these findings. Some results indicate a feedback mechanism between heavy holes and nuclear spins [162, 166]. Theories based on p -symmetric Bloch functions predict that flip-flop terms similar to those of the electronic hyperfine Hamiltonian are very weak [64, 106]. It was, then, proposed that non-collinear hyperfine interactions could account for the joint dynamics [167, 168]. An alternative explanation would be that hole states have to be described by both p - and d -type Bloch functions [169]. This leads to a stronger flip-flop mechanism and the sign of the Ising-like interaction to be opposite for cations and anions.

In spite of all, it remains unclear if a more involved interaction than the Ising-like exists between heavy holes confined in a nanostructure and the surrounding nuclear spins. This unknown is a hindrance to our understanding of the joint dynamics and to future developments relying on nuclear spins for quantum computing [157, 158, 170–173].

In this chapter, we show that the hyperfine interaction for heavy-hole states, described with p -symmetric Bloch functions, induces nuclear spin precession via the non-collinear interaction. This prevents from polarizing nuclear spins by transferring the angular momentum of a well-defined electron spin state. Signatures of this dynamics can be observed in self-assembled quantum dots by pumping nuclear spins optically [68] and measuring the saturation value of nuclear spin polarization. Under the right conditions, the non-collinear

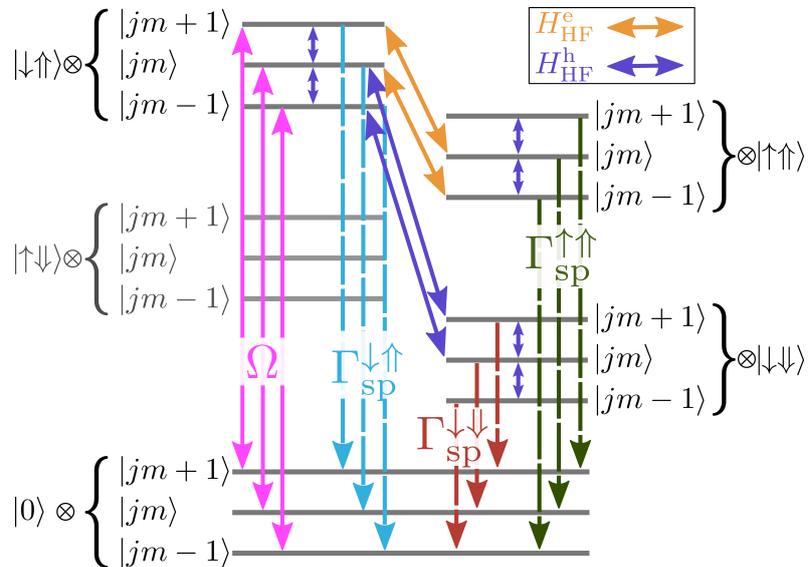


Abbildung 4.1: Level scheme of the excitonic states in a neutral quantum dot showing optically driven transitions with Rabi frequency Ω under the absorption of σ_+ polarized light (magenta). The nuclear states are described with the total angular momentum j and magnetization m . Hyperfine mediated transitions via the electron are shown in orange and in purple for the hole spin. The excited states relax via spontaneous emission with rates $\Gamma_{\text{sp}}^{\downarrow\uparrow} \approx \Gamma_{\text{sp}}^{\uparrow\downarrow} \gg \Gamma_{\text{sp}}^{\uparrow\uparrow} \approx \Gamma_{\text{sp}}^{\downarrow\downarrow}$. Figure provided by Hugo Ribeiro.

interaction can be cancelled and a simultaneous increase in nuclear spin polarization can be detected.

Opposite to earlier theories [167, 168], we treat the non-collinear interaction coherently and show that it influences the nuclear spin dynamics even when the laser frequency is on resonance with the optically allowed electronic transition. Our results not only provide an explanation for the experimentally observed low degrees of nuclear spin polarization, but they also offer an alternative interpretation to the results found in Ref. [169] since the orientation of nuclear spins cannot be assumed to be solely defined by the electron spin flip.

The effective Hamiltonian (see App. C.3),

$$H = H'_0 + H'_L + H_Z^{\text{nuc}} + H_{\text{HF},z}^e + H_{\text{HF},z}^h + H_{\text{HF},\text{nc}}^h, \quad (4.1)$$

describes the system's coherent dynamics under optical excitation and in the presence of an external magnetic field oriented along the growth axis of the quantum dot (Faraday geometry). The Hamiltonian H'_0 describes the evolution

of the exciton states,

$$\begin{aligned}
H'_0 = & \frac{\hbar\Delta}{2} (-|0\rangle\langle 0| + |\downarrow\uparrow\rangle\langle\downarrow\uparrow|) + \left(\frac{\hbar\Delta}{2} + E_{\downarrow\uparrow}^{\uparrow\downarrow}\right) |\uparrow\downarrow\rangle\langle\uparrow\downarrow| \\
& + \left(\frac{\hbar\Delta}{2} + E_{\downarrow\uparrow}^{\uparrow\uparrow}\right) |\uparrow\uparrow\rangle\langle\uparrow\uparrow| + \left(\frac{\hbar\Delta}{2} + E_{\downarrow\uparrow}^{\downarrow\downarrow}\right) |\downarrow\downarrow\rangle\langle\downarrow\downarrow|,
\end{aligned} \tag{4.2}$$

where Δ is the laser detuning and we use the notation \uparrow, \downarrow to denote the electron's spin states and \uparrow, \downarrow the effective heavy-hole states. We have

$$\begin{aligned}
E_{\downarrow\uparrow}^{\uparrow\downarrow} &= -\sqrt{\delta_1^2 + g_-^2 \mu_B^2 B^2}, \\
E_{\downarrow\uparrow}^{\uparrow\uparrow} &= -\delta_0 + \frac{1}{2} \left(\sqrt{\delta_2^2 + g_+^2 \mu_B^2 B^2} - \sqrt{\delta_1^2 + g_-^2 \mu_B^2 B^2} \right), \\
E_{\downarrow\uparrow}^{\downarrow\downarrow} &= -\delta_0 - \frac{1}{2} \left(\sqrt{\delta_2^2 + g_+^2 \mu_B^2 B^2} + \sqrt{\delta_1^2 + g_-^2 \mu_B^2 B^2} \right),
\end{aligned} \tag{4.3}$$

with $E_j^i = E_i - E_j$ and we have defined $g_+ = g_e + 3g_h$ and $g_- = g_e - 3g_h$ with g_e (g_h) the electron (heavy hole) Landé g factor, and μ_B is the Bohr magneton. The coefficients δ_0 , δ_1 , and δ_2 describe, respectively, the fine structure splitting between bright and dark excitons, among bright, and among dark excitons [174]. Since we are considering σ_+ circularly polarized light and working in a Faraday geometry, the evolution of $|\uparrow\downarrow\rangle$ is trivial. We can therefore reduce the complexity of the problem by omitting this state. The laser Hamiltonian reads

$$H'_L = \hbar\Omega (|0\rangle\langle\downarrow\uparrow| + |\downarrow\uparrow\rangle\langle 0|). \tag{4.4}$$

where Ω is the Rabi frequency. The electronic hyperfine Hamiltonian within the homogeneous coupling approximation is given by

$$H_{\text{HF}}^e = H_{\text{HF},z}^e + H_{\text{HF},\perp}^e = A^e \left(S_z I_z + \frac{1}{2} (S_+ I_- + S_- I_+) \right). \tag{4.5}$$

Here, S_z and $I_z = \sum_k I_z^k$ are, respectively, the electron spin and total nuclear spin operators in z direction, where the sum run over all nuclear spins k . We have also introduced the ladder operators, $S_{\pm} = S_x \pm iS_y$ and $I_{\pm} = \sum_k I_x^k \pm iI_y^k = I_x \pm iI_y$. We denote the average hyperfine coupling constant as A^e , the longitudinal part of Eq. (4.5) by $H_{\text{HF},z}^e$, and the transverse one by $H_{\text{HF},\perp}^e$. The effective hyperfine Hamiltonian for heavy holes can be written as (see App. C.2)

$$\begin{aligned}
H_{\text{HF}}^h &= H_{\text{HF},z}^h + H_{\text{HF},\perp 1}^h + H_{\text{HF},\perp 2}^h + H_{\text{HF},\text{nc}}^h \\
&= A_z^h S_z^h I_z + A_{\perp 1}^h S_+^h I_- + A_{\perp 1}^{h*} S_-^h I_+ + A_{\perp 2}^h S_+^h I_+ \\
&\quad + A_{\perp 2}^{h*} S_-^h I_- + A_{\text{nc}}^h S_z^h I_+ + A_{\text{nc}}^{h*} S_z^h I_-,
\end{aligned} \tag{4.6}$$

where S_i^h ($i = z, \pm$) are pseudospin operators for the effective heavy-hole states (see App. C.2). We use a similar notation to the one introduced in Eq. (4.5) and further denote the non-collinear term by $H_{\text{HF,nc}}^h$. The nuclear Zeeman Hamiltonian is given by

$$H_n^Z = g_n \mu_n B I_z, \quad (4.7)$$

with g_n the nuclear Landé g factor and μ_n the nuclear Bohr magneton. Finally, we emphasize that Hamiltonian (4.1) is valid when the laser frequency is close to resonance with the transition $|0\rangle \leftrightarrow |\downarrow\uparrow\rangle$ [c.f. Fig. 4.1].

Here, we follow the procedure of Refs. [175, 176] and describe the contribution of the transverse (flip-flop) terms of Eqs. (4.5) and (4.6) on the dynamics as a dissipative process. The evolution of the system is then described by the Lindblad master equation [177], $\dot{\rho} = -\frac{i}{\hbar}[H, \rho] + \sum_{j=1}^{d^2-1} ([L_j \rho, L_j^\dagger] + [L_j, \rho L_j^\dagger])/2$, with d the dimension of the Hilbert space. Since we only consider dissipative processes within the electronic subspace, we get by with less Lindblad operators. We take into account spontaneous emission from the bright exciton $|\downarrow\uparrow\rangle$ and from both (quasi) dark excitons to the ground state [169]. These are described by $L_1 = \sqrt{\Gamma_{\text{sp}}^{\downarrow\uparrow}} |0\rangle \langle\downarrow\uparrow|$, $L_2 = \sqrt{\Gamma_{\text{sp}}^{\uparrow\uparrow}} |0\rangle \langle\uparrow\uparrow|$, and $L_3 = \sqrt{\Gamma_{\text{sp}}^{\downarrow\downarrow}} |0\rangle \langle\downarrow\downarrow|$, where Γ_{sp}^j , $j = \downarrow\uparrow, \uparrow\uparrow, \downarrow\downarrow$, is the spontaneous decay rate. The nuclear spin state is characterized by its total angular momentum j and its projection along the magnetic field given by m [c.f. Fig. 4.1]. The Lindblad operators $L_4 = \sqrt{\Gamma_e^{\downarrow\uparrow}} |0, j, m-1\rangle \langle\downarrow\uparrow, j, m|$ and $L_5 = \sqrt{\Gamma_h^{\downarrow\uparrow}} |0, j, m+1\rangle \langle\downarrow\uparrow, j, m|$ describe electron and hole flip-flop processes, respectively. The rates $\Gamma_e^{\downarrow\uparrow}$ and $\Gamma_h^{\downarrow\uparrow}$ are calculated with the same method as in Ref. [176], we find

$$\Gamma_e^{\downarrow\uparrow} \simeq \frac{\Gamma_{\text{sp}}^{\uparrow\uparrow}}{4} \left| \frac{A^e \sqrt{j(j+1) - m(m-1)}}{-E_{\downarrow\uparrow}^{\uparrow\uparrow} - A^e(m - \frac{1}{2}) + \frac{3}{2}A_z^h + g_n \mu_n B} \right|^2, \quad (4.8)$$

where we have neglected the contribution coming from $H_{\text{HF},\pm 2}^h$ since $|A_{\pm 2}^h|/A^e \ll 1$ and

$$\Gamma_h^{\downarrow\uparrow} = \frac{\Gamma_{\text{sp}}^{\downarrow\downarrow}}{4} \left| \frac{A_{\pm 1,1}^h \sqrt{j(j+1) - m(m+1)}}{-E_{\downarrow\uparrow}^{\downarrow\downarrow} + \frac{1}{2}A^e + 3A_z^h(m + \frac{1}{2}) - g_n \mu_n B} \right|^2. \quad (4.9)$$

We assume nuclear spins to be initially in a thermal state. This is a reasonable assumption even for experiments performed at low temperatures, where the thermal energy is larger than the nuclear Zeeman energy, $k_B T \gg E_Z^{\text{nuc}}$, with k_B the Boltzmann's constant. Thus, at $t = 0$, the nuclear spins are assumed to be in a fully mixed state. Further assuming spin-1/2 for the nuclei,

we have $\rho_{\text{nuc}} = \sum_{j,m} p(j)p(m|j) |j, m\rangle \langle j, m|$ [176],

$$\rho_{\text{nuc}} = \sum_{j=j_{\text{min}}}^{N/2} \sum_{m=-j}^j \frac{(2j+1)N!}{\left(\frac{N}{2}+j+1\right)! \left(\frac{N}{2}-j\right)! 2^N} |j, m\rangle \langle j, m|, \quad (4.10)$$

with N the number of nuclear spins and $j_{\text{min}} = 0$ for even N and $j_{\text{min}} = 1/2$ for odd N . The initial electronic state is given by the quantum dot vacuum, i.e., $\rho_e = |0\rangle \langle 0|$. Thus, we have $\rho(t=0) = \rho_e \otimes \rho_{\text{nuc}}$.

In Fig. 4.2(a), we present the degree of nuclear spin polarization $P = \text{Tr}[\rho_{\text{nuc}}(t_p)I_z]/P_{\text{max}}$ as a function of pumping time t_p and spontaneous decay rate of the dark states $\Gamma_{\text{sp}}^{\text{d}}$, where $P_{\text{max}} = N/2$. Since the ratio of the dark states energy is nearly one, $E_{\uparrow\uparrow}/E_{\downarrow\downarrow} \approx 1$ (see App. C.3), we have $\Gamma_{\text{sp}}^{\uparrow\uparrow} \simeq \Gamma_{\text{sp}}^{\downarrow\downarrow} = \Gamma_{\text{sp}}^{\text{d}}$. The calculations were performed with $\delta_0 = 5.6213 \cdot 10^{11}$ Hz, $\delta_1 = \delta_2 = 5.3174 \cdot 10^{10}$ Hz, $B = 8$ T, $g_e = -0.35$, $g_h = 0.63$, $g_n \mu_n = 3.3 \cdot 10^{-8}$ eV/T, $\Delta = 0$ Hz, $\Omega = 2.03 \cdot 10^{10}$ Hz, $A^e = 10^8$ Hz, $A_z^h = -10^7$ Hz, $|A_{\perp 1}^h| = 3 \cdot 10^5$ Hz, $A_{\text{nc}}^h = 3 \cdot 10^5$ Hz, $\Gamma_{\text{sp}}^{\downarrow\uparrow} = 2 \cdot 10^9$ Hz, and $N = 30$. We have cancelled out the imaginary part of $H_{\text{HF,nc}}^h$ by performing a suitable rotation of angle θ , $U = \exp[i\theta I_z]$. The saturation of the nuclear polarization depends strongly on the lifetime of the dark excitons. To demonstrate clearly this behavior, we present traces taken for different values of $\Gamma_{\text{sp}}^{\text{d}}$ [Fig. 4.2(b)] and for $t_p = 30$ s [Fig. 4.2(c)], for which P has reached saturation. Both of these traces show that P saturates at smaller values for slower $\Gamma_{\text{sp}}^{\text{d}}$. To identify the interaction responsible of this behavior, we compare P as function of t_p for $\Gamma_{\text{d}} = 10^7 \text{ s}^{-1}$ between an Ising-like ($H_{\text{HF},z}^h$) and other forms of the effective heavy hole hyperfine Hamiltonian. In Fig. 4.2(d), we compare P obtained with $H_{\text{HF},z}^h$ (gray) to the effective Hamiltonian given by Eq. (4.6) (red). The different values of P at saturation indicate that the relatively small corrections to the Ising-like hyperfine Hamiltonian influence the dynamics. For $H_{\text{HF},z}^h$, P saturates due to formation of a nuclear spin dark state [176]. To tell apart the contribution of $H_{\text{HF},\perp 1}^h$ and $H_{\text{HF,nc}}^h$, we plot P obtained with $H_{\text{HF},z}^h$ (gray) and $H_{\text{HF},z}^h + H_{\text{HF},\perp 1}^h$ (orange) in Fig. 4.2(e), which show that heavy hole flip-flop processes are irrelevant for the nuclear spin dynamics. In the presence of a large magnetic field and due to the smallness of $|A_{\perp 1}^h|$, the heavy hole forbidden relaxation rate $\Gamma_{\text{h}}^{\downarrow\uparrow}$ is too slow compared to the electronic forbidden relaxation rate $\Gamma_{\text{e}}^{\downarrow\uparrow}$ and to spontaneous emission $\Gamma_{\text{sp}}^{\downarrow\uparrow}$ to have an impact on the nuclear spin polarization. In Fig. 4.2(f), we show P calculated with $H_{\text{HF},z}^h$ (gray) and $H_{\text{HF},z}^h + H_{\text{HF,nc}}^h$ (blue). P is hindered by the non-collinear interaction because it induces precession of the nuclear spins. In essence, it is similar to a spin-1/2 prepared in a given direction and evolving in a perpendicular B field. If the

evolution time is shorter than the period, then the polarization along the initial direction is always smaller than at time $t = 0$. Consider the system to be in the electronic dark state $|\uparrow\uparrow\rangle$ and for simplicity that only the nuclear states $|j, -j\rangle$ are populated after an electron spin flip. The evolution of the nuclear spins is then approximatively given by $U_{\text{nuc}} \approx \exp[-i \int_0^{1/\Gamma_{\text{sp}}^{\text{d}}} dt H_{\text{HF,nc}}^{\text{h}}/\hbar]$ and $\rho_{\text{nuc}}(1/\Gamma_{\text{sp}}^{\text{d}}) = \sum_{j,m,m'} p(j) c_m(1/\Gamma_{\text{sp}}^{\text{d}}) c_{m'}^*(1/\Gamma_{\text{sp}}^{\text{d}}) |j, m\rangle \langle j, m'|$. For an evolution time shorter than the precession period, $1/\Gamma_{\text{sp}}^{\text{d}} < 1/A_{\text{nc}}^{\text{h}}$, we have $\text{Tr}[\rho_{\text{nuc}}(0)I_z]/P_{\text{max}} > \text{Tr}[\rho_{\text{nuc}}(1/\Gamma_{\text{sp}}^{\text{d}})I_z]/P_{\text{max}}$ because nuclear states with a magnetization $m > -j$ are effectively repopulated ($|c_m(1/\Gamma_{\text{sp}}^{\text{d}})|^2 > 0$). This simple picture qualitatively agrees with our results, where a lower value of P at saturation indicates that most of the nuclear spin states are still populated [cf. Figs. 4.2(a), (b), and (c)]. The steady state corresponds to the nuclear state whose precession lowers P by the same amount it was increased after receiving angular momentum from the electron spin. The mechanism depicted above relies on having nuclear spins oriented along a different direction than the one defined by the effective magnetic field associated with $H_{\text{HF,nc}}^{\text{h}}$, which is provided by the optical pumping mechanism. Finally, we emphasize that the oscillator strength for dark excitons is a hundred to a thousand times smaller than the oscillator strength of bright excitons [169], which implies $\Gamma_{\text{sp}}^{\downarrow\uparrow}/\Gamma_{\text{sp}}^{\text{d}} \approx 100 - 1000$. Our findings suggest that there could be an alternative interpretation of recent experimental results about the sign of the Ising-like interaction [169]. The unexpected shift of the Overhauser field could simply originate from the induced dynamics, which lowers P , when measuring the spectral position of the dark excitons.

In the following, we propose an experiment to detect and simultaneously cancel the effect of the non-collinear interaction. A short hand notation for Eq. (4.6) is $H_{\text{HF}}^{\text{h}} = \mathbf{S} \cdot \mathbf{A}^{\text{h}} \cdot \mathbf{I}$, with \mathbf{A}^{h} the heavy-hole hyperfine tensor. The idea is to align the external magnetic field, by rotating it, along the principal axis defined by \mathbf{A}^{h} . In this geometry, the non-collinear interaction vanishes and the precession of nuclear spins stops. By rotating B , the nuclear Zeeman Hamiltonian becomes $H_{\text{n}}^Z = g_{\text{n}}\mu_{\text{n}}B \cos(\varphi)I_z + g_{\text{n}}\mu_{\text{n}}B \sin(\varphi)(I_+ + I_-)/2$, with φ the rotation angle. In our coordinate system the magnetic field has to be rotated around the y -axis, i.e., φ is the angle between the z -axis and \mathbf{B} . In addition to the change $B \rightarrow B \cos(\varphi) \equiv B_z$ in Eqs. (4.1), (4.8), and (4.9) as well as the discussed modification of the nuclear Zeeman Hamiltonian, we also need to take into account that misalignment of \mathbf{B} leads to mixing of bright and dark excitons via $H_{\text{bd}} = g_{\text{e}}\mu_{\text{B}}B \sin(\varphi)(S_+ + S_-)/4 + g_{\text{h}}^{xx}\mu_{\text{B}}B \sin(\varphi)(S_+^{\text{h}} + S_-^{\text{h}})/4$, with $g_{\text{h}}^{xx} \simeq g_{\text{h}}/10$ [178, 179] the heavy hole Landé g factor along the x -axis. We also

add to the dissipative part of the Lindblad equation spontaneous relaxation from $|\uparrow\downarrow\rangle$ to the ground state with rate $\Gamma_{\text{sp}}^{\uparrow\downarrow}$ and two non-conserving nuclear spin relaxation mechanisms. These are described by $L_6 = \sqrt{\Gamma_{\text{sp}}^{\uparrow\downarrow}} |0\rangle \langle\uparrow\downarrow|$, $L_7 = \sqrt{\Gamma_e^{\uparrow\downarrow}} |0, j, m+1\rangle \langle\uparrow\downarrow, j, m|$, and $L_8 = \sqrt{\Gamma_h^{\uparrow\downarrow}} |0, j, m-1\rangle \langle\uparrow\downarrow, j, m|$ with

$$\Gamma_e^{\uparrow\downarrow} \simeq \frac{\Gamma_{\text{sp}}^{\downarrow\downarrow}}{4} \left| \frac{A^e \sqrt{j(j+1) - m(m+1)}}{-E_{\uparrow\downarrow}^{\downarrow\downarrow} + A^e(m + \frac{1}{2}) + \frac{3}{2}A_z^h - g_n\mu_n B_z} \right|^2, \quad (4.11)$$

and

$$\Gamma_h^{\uparrow\downarrow} = \frac{\Gamma_{\text{sp}}^{\uparrow\uparrow}}{4} \left| \frac{A_{\perp\perp 1}^h \sqrt{j(j+1) - m(m-1)}}{-E_{\uparrow\downarrow}^{\uparrow\uparrow} + \frac{1}{2}A^e + \frac{3}{2}A_z^h(m - \frac{1}{2}) + g_n\mu_n B_z} \right|^2. \quad (4.12)$$

In Fig. 4.3(a), we plot the nuclear spin polarization P as a function of t_p and φ . We use the same set of parameters as before and $\Gamma_{\text{sp}}^d = 10^7 \text{ s}^{-1}$. As for the dark exciton, we have $E_{\downarrow\uparrow}/E_{\uparrow\downarrow} \approx 1$ which allows us to write $\Gamma_{\text{sp}}^{\uparrow\downarrow} \simeq \Gamma_{\text{sp}}^{\downarrow\uparrow} = \Gamma_{\text{sp}}^b$. The results show that nuclear spin precession is fully suppressed at $\varphi \simeq -0.014 \text{ rad}$, for which we retrieve the saturation limit set by the nuclear spin dark state. In Fig. 4.3(b), we show a trace taken for $t_p = 30 \text{ s}$.

In conclusion, we have shown that the effective heavy-hole non-collinear hyperfine interaction creates a feedback mechanism between heavy holes and nuclear spins and how to experimentally detect the latter. Our results can be extended to self-assembled dots which are embedded in a Schottky diode and operated in the cotunnelling regime. It was experimentally demonstrated that even in the presence of cotunnelling the lifetime of dark excitons is approximately 30 times longer than the radiative lifetime of bright excitons [180]. As our results suggest, this timescale is sufficiently long to allow experimental observation of the discussed dynamics. Finally, we expect the described effects to be stronger when considering an inhomogeneous hyperfine Hamiltonian since the statistical weight of the states contributing the most to P are not suppressed [176]. Moreover, when trying to cancel the heavy hole non-collinear interaction, a series of maximums, one for each nuclear species, should be observed as a function of the rotation angles.

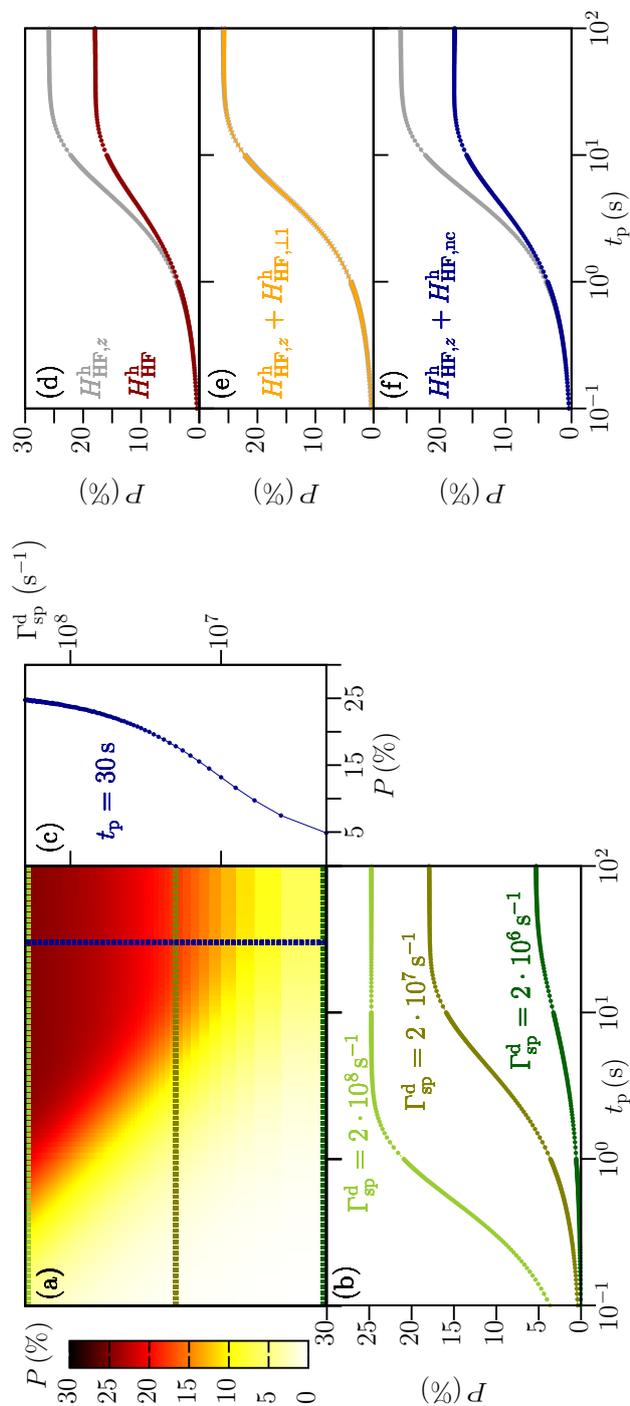


Abbildung 4.2: (a) Nuclear spin polarization P as a function of pumping time t_p and spontaneous decay rate $\Gamma_{sp}^d \approx \Gamma_{sp}^{d,\downarrow} = \Gamma_{sp}^d$. Values of other parameters are given in the main text. (b) Traces taken along $\Gamma_{sp}^d = 2 \cdot 10^8$, $2 \cdot 10^7$, and $2 \cdot 10^6$ Hz. P saturates at lower values for smaller Γ_{sp}^d 's. (c) Trace taken along $t_p = 30$ s showing the dependence on Γ_{sp}^d . (d) Comparison of P as a function of t_p between $H_{HF}^h = H_{HF,z}^h$ (gray), for which saturation corresponds to formation of a nuclear spin dark state, and the full effective Hamiltonian Eq. (4.6) (red) for $\Gamma_{sp}^d = 2 \cdot 10^7$ Hz. (e) Same as (d) but compared with $H_{HF}^h = H_{HF,z}^h + H_{HF,11}^h$. The result shows that heavy hole mediated flip-flop processes are negligible. (f) Same as (d) but compared with $H_{HF}^h = H_{HF,z}^h + H_{HF,nc}^h$. The heavy hole hyperfine non-collinear interaction is the origin of the lower values of P since it leads to an effective nuclear spin diffusion mechanism. *Figure provided by Hugo Ribeiro.*

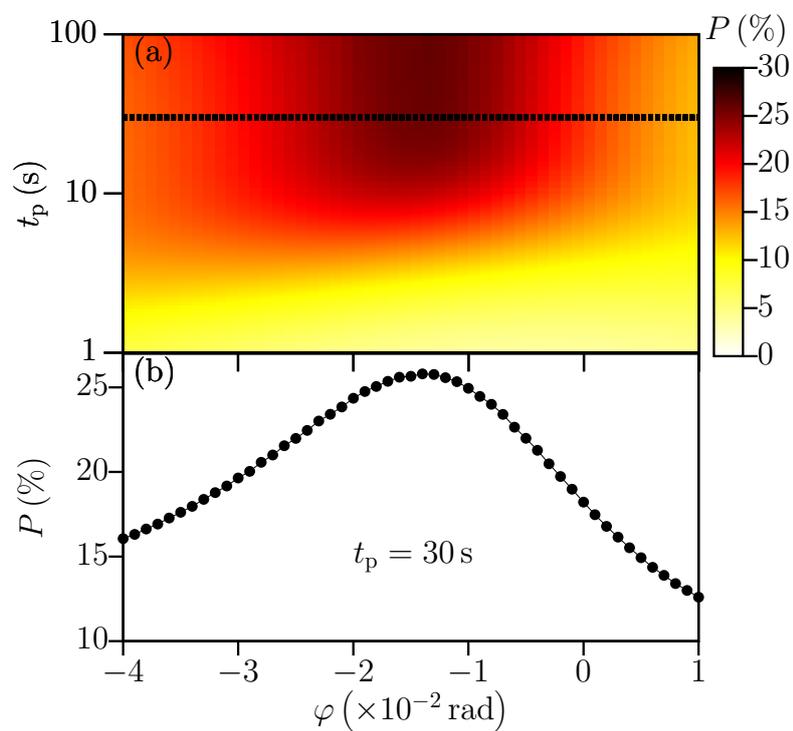


Abbildung 4.3: (a) Nuclear spin polarization P as a function of t_p and φ (angle between the external magnetic field \mathbf{B} and the z -axis) for $\Gamma_{\text{sp}}^{\text{d}} = 2 \cdot 10^7 \text{ s}^{-1}$. (b) Trace taken along $t_p = 30 \text{ s}$. The effect of the non-collinear interaction can be cancelled by orienting the magnetic field opposite to the effective Overhauser field defined by the hyperfine non-collinear Hamiltonian. *Figure provided by Hugo Ribeiro.*

Acknowledgments

We are thankful to Julia Hildmann and Richard J. Warburton for fruitful discussions. We acknowledge funding from the Swiss SNF, NCCR QSIT, and S³ NANO.

Anisotropic g factor in InAs self-assembled quantum dots

Adapted from:

R. Zielke, F. Maier and D. Loss,
‘Anisotropic g factor in InAs self-assembled quantum dots’,
Phys. Rev. B **89**, 115438 (2014).

We investigate the wave functions, spectrum, and g -factor anisotropy of low-energy electrons confined to self-assembled, pyramidal InAs quantum dots (QDs) subject to external magnetic and electric fields. We present the construction of trial wave functions for a pyramidal geometry with hard-wall confinement. We explicitly find the ground and first excited states and show the associated probability distributions and energies. Subsequently, we use these wave functions and 8-band $\mathbf{k} \cdot \mathbf{p}$ theory to derive a Hamiltonian describing the QD states close to the valence band edge. Using a perturbative approach, we find an effective conduction band Hamiltonian describing low-energy electronic states in the QD. From this, we further extract the magnetic field dependent eigenenergies and associated g factors. We examine the g factors regarding anisotropy and behavior under small electric fields. In particular, we find strong anisotropies, with the specific shape depending strongly on the considered QD level. Our results are in good agreement with recent measurements [181] and support the possibility to control a spin qubit by means of g -tensor modulation.

5.1 Introduction

Electron spins confined to semiconductor quantum dots (QDs) are excellent candidates for the physical realization of qubits, the elementary units of quantum computation [29]. The qubit state can be initialized and manipulated by means of externally applied electric and magnetic fields. Thus knowledge about the qubit's response to these fields is crucial for the successful operation of qubits. This response depends strongly on the type of QD considered, e.g., lateral gate defined QDs, nanowire QDs, and self-assembled QDs [28, 45]. The most prominent type of QDs for self-assembled QDs are InAs QDs grown on a GaAs surface or in a GaAs matrix. These QDs can be grown in various shapes such as pyramids [12, 182, 183], truncated pyramids [184], and flat disks [185] and hence are highly strained due to the lattice constant mismatch of substrate and QD materials. In self-assembled InAs QDs, spin states have been prepared with more than 99% fidelity [31] and complete quantum control by optical means has been shown [36, 40]. However, full qubit control by means of external fields and small system sizes are the most important goals in solid state based quantum computation, allowing for the construction of integrated circuits [28, 45]. Regarding these requirements, g -tensor modulation is a powerful mechanism that allows control of the qubit [49–51] but is sensitive to the shape of the QD hosting the qubit [28]. Hence the qubit behavior under the influence of geometry, external fields, etc., is still subject to ongoing scientific effort [120, 186, 187]. A crucial ingredient for modeling the qubit behavior is the knowledge of the particle distribution within the QD, i.e., the envelope wave function which is mainly determined by the shape of the QD. For simple structures such as spheres, flat cylinders, and cubes, the wave functions in QDs can be described analytically, e.g., by employing hard-wall or harmonic confinement potentials [188]. For more complicated shapes usually numerical models are employed [12, 189–192]. Recently, there have been efforts to find analytical wave functions for pyramids with different types of boundary conditions [193, 194]. However, the set of wave functions introduced so far has been observed to be incomplete, lacking for example the ground state wave function. Both analytical and numerical methods are employed to further explore QD characteristics such as strain [12, 195], spectra [12], and g factors [196, 197]. Explicit values depend on the material properties. Building QDs in materials with very large, isotropic bulk g factors, i.e., InAs ($g = -14.9$), is favorable due to an improved opportunity of g -factor modification. Measurements emphasize the decrease of the g factor when considering electrons in

InAs QDs. Numerical calculations [192, 196, 197] and measurements [198, 199] show that the g factor can go down to very small values and depends strongly on the dot size. Furthermore, recent measurements show a significant anisotropy [181, 200] of the g factor which turned out to be tunable by electrical means [181, 201]. This behavior of g can be attributed to material- and confinement-induced couplings between the conduction band (CB) and the valence band (VB) which result in totally mixed low-energy states.

The outline of this chapter is as follows. In Sec. 5.2, we present an 8-band $\mathbf{k} \cdot \mathbf{p}$ Hamiltonian describing the low-energy QD states which accounts for strain and external electric and magnetic fields. Additionally, we introduce a set of trial wave functions satisfying the hard-wall boundary conditions of a pyramidal QD. Furthermore, we derive an effective Hamiltonian describing CB states in the QD. In Sec. 5.3, we present the results of our calculations, in particular the g -factor anisotropy of CB QD levels. These results are discussed and compared to recent measurements in Secs. 5.4 and 5.5, respectively. Finally, in Sec. 5.6, we conclude.

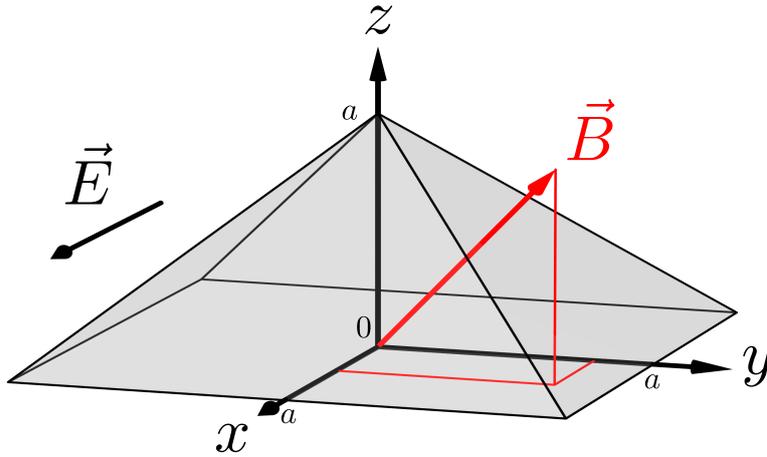


Abbildung 5.1: Sketch of the QD geometry and the coordinate system used in this work with x , y , and z axes pointing along the growth directions [100], [010], and [001], respectively. The externally applied fields under consideration are $\mathbf{B} = (B_x, B_y, B_z)$ and $\mathbf{E} = (E_x, 0, 0)$. *Figure provided by Robert Zielke.*

5.2 Model

In this section, we introduce the Hamiltonian and wave functions used in this chapter. Furthermore we outline the performed calculations and give the main results in a general manner.

Hamiltonian

Low-energy states in bulk III-V semiconductors are well described by an 8-band $\mathbf{k} \cdot \mathbf{p}$ model [6], which includes the CB and the VB consisting of heavy-hole (HH) and light-hole (LH) bands, and split-off (SO) bands. The associated Hamiltonian $H_{\mathbf{k} \cdot \mathbf{p}}$ is given in terms of two-fold degenerate basis states $|j, \pm\rangle$, $j = \text{CB, HH, LH, SO}$, which are linear combinations of products of angular momentum eigenfunctions and real spin states [6]. We model a pyramidal QD by taking into account a three-dimensional hard-wall confinement potential V_c defining a square pyramid of height a and base length $2a$ as sketched in Fig. 5.1. We introduce strain by adding the strain Hamiltonian H_{strain} [6]. An analytical description of the strain distribution within an InAs pyramid enclosed in a GaAs matrix can be modeled by exploiting the analogy to electrostatic theory [195]. We include the effect of an externally applied magnetic field $\mathbf{B} = \nabla \times \mathbf{A}$ defined by the vector potential \mathbf{A} ($\nabla \cdot \mathbf{A} = 0$) by adding two terms. The first term is the magnetic interaction term H_Z [6]. To derive the second term, H_B , we replace $\mathbf{k} \rightarrow \mathbf{k} + e\mathbf{A}/\hbar$ in $H_{\mathbf{k} \cdot \mathbf{p}}$ and H_{strain} in a semiclassical manner, where e is the positive elementary charge and \hbar the Planck constant. We drop all contributions independent of \mathbf{B} and obtain a Hamiltonian which accounts for orbital effects of \mathbf{B} . An external electric field \mathbf{E} is included by adding the electric potential $H_E = e \mathbf{E} \cdot \mathbf{r}$, with $\mathbf{r} = (x, y, z)$. The full system is then described by the Hamiltonian

$$H = H_{\mathbf{k} \cdot \mathbf{p}} + H_{\text{strain}} + H_Z + H_B + H_E + V_c. \quad (5.1)$$

Note that literature values for $\mathbf{k} \cdot \mathbf{p}$ parameters are usually given for 4-band models. In an 8-band model, the parameters have to be modified accordingly [6].

Hard-wall wave function

As a first step, we consider V_c of a pyramidal QD analytically and require a vanishing particle density at the boundaries. We construct a trial wave function satisfying these boundary conditions as follows.

The Schrödinger equation of a particle confined in a square with sides of length a with vanishing boundary conditions on the borders, has the well-known solution $\psi_{mn}^{\square}(x, y)$ with eigenenergies E_{mn}^{\square} . The wave function of a particle confined in an isosceles triangle obtained by cutting the square along the diagonal, $\psi^{\triangle}(x, y)$, is then constructed by linear combinations of degenerate solutions $\psi_{mn}^{\square}(x, y)$ while requiring a vanishing wave function at the

diagonal of the square [202]. We span the full three-dimensional (3D) volume of the pyramid and the corresponding wave functions with the product of two such triangles and the associated ψ^Δ . This consideration suggests then the following ansatz for the hard-wall wave functions inside the pyramidal geometry of the form

$$\begin{aligned} \psi_{\mathbf{m}}(\mathbf{r}) = c \prod_{\xi=x,y} & \left[\sin(\alpha_\xi \xi^+) \sin(\alpha_z \xi^-) \right. \\ & \left. - (-1)^{m_\xi+m_z} \sin(\alpha_z \xi^+) \sin(\alpha_\xi \xi^-) \right], \end{aligned} \quad (5.2)$$

with $\mathbf{r} = (x, y, z)$, $c = \csc(\pi z)/N_{\mathbf{m}}$, $\alpha_i = m_i\pi/a$, $m_i = 1, 2, 3, \dots$, $m_x \neq m_z$, $m_y \neq m_z$, $\mathbf{m} = (m_x, m_y, m_z)$, $\xi^\pm = \xi \pm (z - a)/2$, and $N_{\mathbf{m}}$ such that the integral over the pyramid volume $\int d^3r |\psi_{\mathbf{m}}(\mathbf{r})|^2 \equiv 1$. We define energies of $\psi_{\mathbf{m}}(\mathbf{r})$ by taking

$$\frac{\hbar^2}{2m_0} \langle \psi_{\mathbf{m}}(\mathbf{r}) | (-i\nabla)^2 | \psi_{\mathbf{m}}(\mathbf{r}) \rangle = E_{\mathbf{m}}, \quad (5.3)$$

where m_0 denotes the bare electron mass. For notational simplicity we use $\psi_{\mathbf{m}} \equiv \psi_{m_x m_y m_z}$ and $E_{\mathbf{m}} \equiv E_{m_x m_y m_z}$. Exact analytical solutions of the Schrödinger equation have been derived using specular reflections of plain waves at the boundaries of the geometry [193]. However, the obtained set of solutions is incomplete, consisting solely of excited states and especially lacking the ground state. We stress that our ansatz $\psi_{\mathbf{m}}$ is not an eigenstate of the Schrödinger equation. However, the energies $E_{\mathbf{m}}$ we find are lower than the eigenenergies of the Schrödinger equation derived in Ref. [193]; see Secs. 5.3 and 5.4. In addition, the wave function for the lowest energy state, ψ_{221} , exhibits the expected nodeless shape for the ground state. A more detailed justification of $\psi_{\mathbf{m}}(\mathbf{r})$ is given in Appendix D.1. In the following calculations, we apply these trial envelope wave functions for both CB and VB states. In general, electron and hole envelope wave functions differ [12, 191]; however, this choice is justified since we find that even this overly simplified picture yields already good results.

Zeeman splitting of the CB states in the QD

A strong confinement of the electron and hole wave functions to the QD, as assumed by taking V_c into account, corresponds to a splitting of the basis states into localized states which can be described as products of the former basis states and the confinement-induced envelope functions,

$$\Psi_{\mathbf{m}}^{j,\pm}(\mathbf{r}) = \psi_{\mathbf{m}}(\mathbf{r}) |j, \pm\rangle. \quad (5.4)$$

We note that a non-trivial set of basis states requires $\max\{m_j\} \geq 3$. We rewrite H in a basis formed by the $\Psi_{\mathbf{m}}^{j,\pm}$ by taking the according matrix elements and find a new Hamiltonian H_d describing the QD states. We split H_d into three parts,

$$H_d = H_d^{\text{d}} + H_d^{\text{bd}} + H_d^{\text{bod}}, \quad (5.5)$$

where H_d^{d} denotes the diagonal elements of H_d , H_d^{bd} denotes the block-diagonal parts of H_d between the CB and VB, and H_d^{bod} the associated block-off-diagonal elements. The external electric and magnetic fields are treated as a perturbation to the system. Hence diagonal terms of H_d stemming from taking matrix elements of H_Z, H_B , and H_E are included in H_d^{d} . Since we are interested in describing electrons confined to CB states of the QD, we decouple the CB states from the VB states by a unitary transformation, the Schrieffer-Wolff transformation (SWT) $\tilde{H}_d = e^{-S} H_d e^S$, where S is an anti-unitary operator ($S^\dagger = -S$) [6]. We approximate the SWT to third order in a small parameter λ determined by the ratio of the CB-VB coupling and the CB-VB energy gap. To this end, we express S as $S = S_1 + S_2 + S_3$, where $\mathcal{O}(S_i) = \lambda^i$. Here, the operators S_i are defined by $[H_d^{\text{d}}, S_1] = -H_d^{\text{bod}}$, $[H_d^{\text{d}}, S_2] = -[H_d^{\text{bd}}, S_1]$, $[H_d^{\text{d}}, S_3] = -[H_d^{\text{bd}}, S_2] - 1/3[[H_d^{\text{bod}}, S_1], S_1]$ [6]. Since λ is small, we can expand e^S up to third order in λ using the decomposition of S . Assuming that $\mathcal{O}(H_d^{\text{d}}) = \lambda^0$, $\mathcal{O}(H_d^{\text{bd}}) = \mathcal{O}(H_d^{\text{bod}}) = \lambda^1$, we perform the SWT where we keep terms up to third order in λ in the final Hamiltonian \tilde{H}_d . In a last step, we project \tilde{H}_d on the CB and find an effective CB Hamiltonian, \tilde{H}_d^{CB} . In \tilde{H}_d^{CB} , the single QD levels are strongly coupled, and thus cannot be treated perturbatively anymore. Instead, we diagonalize \tilde{H}_d^{CB} exactly and evaluate the eigenenergies E_n^\pm , where the indices denote the n th QD level from the VB edge with effective spin \pm . We find the g factor of the n th spin-split QD level by taking

$$g_n = \frac{E_n^+ - E_n^-}{\mu_B |\mathbf{B}|}, \quad (5.6)$$

with Bohr magneton μ_B . Since the exact values of the energies E_n^\pm depend on the magnitude and direction of the external fields \mathbf{E} and \mathbf{B} , $g_n = g_n(\mathbf{E}, \mathbf{B})$. \tilde{H}_d^{CB} contains higher order terms in \mathbf{B} ; thus we find

$$g_n = g_{n,0} + g_{n,2} |\mathbf{B}|^2, \quad (5.7)$$

which is consistent with the general behavior expected of \tilde{H}_d under time reversal. However, with $|g_{n,2}| \ll |g_{n,0}|$, the quadratic dependence of g_n on $|\mathbf{B}|$ is barely measurable in experiments.

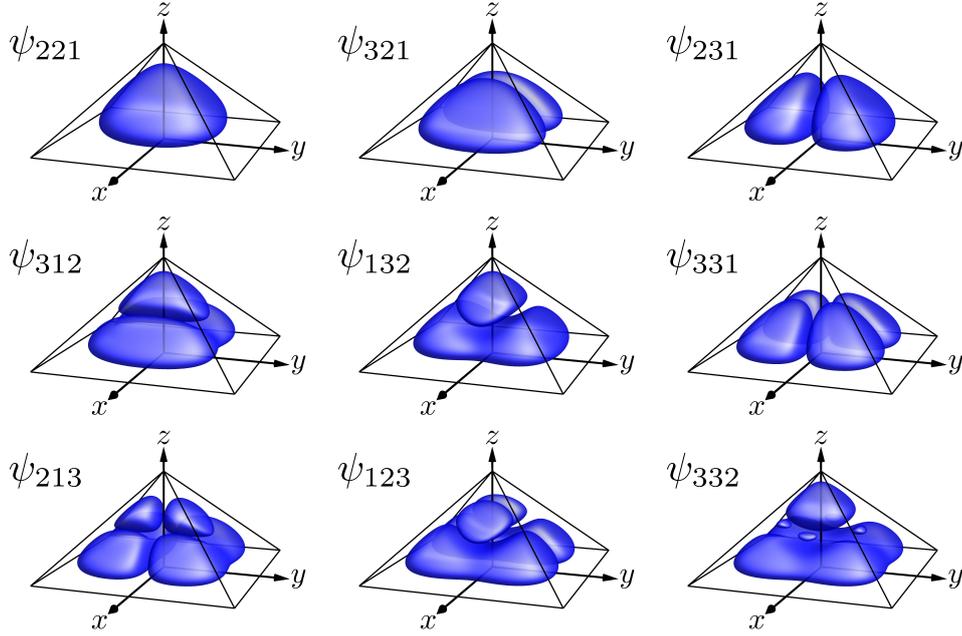


Abbildung 5.2: Probability distributions of the smallest nontrivial set of trial wave functions $\psi_{\mathbf{m}}(\mathbf{r})$, i.e., $\max(m_i) = 3$, satisfying the hard-wall boundary conditions for the geometry given in Fig. 5.1. We show contour plots of $|\psi_{\mathbf{m}}(\mathbf{r})|^2 = 0.1$ inside the pyramidal geometry assumed for the QD; see Fig. 5.1. Note the degenerate pairs: ψ_{321} and ψ_{231} , ψ_{312} and ψ_{132} , ψ_{213} and ψ_{123} . Figure provided by Robert Zielke.

5.3 Results

In this section, we present the results of the calculations outlined in Sec. 5.2. All calculations were performed for a pyramidal QD of height $a = 50$ nm. We consider basis states that fulfill $\max\{m_i\} \leq 3$, which results in a splitting of each band $|j, +\rangle$ ($|j, -\rangle$) into nine QD levels. The system parameters used for the Hamiltonians are listed in Table D.1 in Appendix D.2, where the notation directly corresponds to the notation used in Ref. [6].

Probability distribution of the wave function

We show contour plots of the probability distribution $|\psi_{\mathbf{m}}(\mathbf{r})|^2$ of the wave function found in Eq. (5.2), see Fig. 5.2. We present the lowest-energy states forming the smallest nontrivial set of wave functions. The ground state ψ_{221} with associated ground state energy $E_{221} = 0.53$ meV exhibits s -wave character; i.e., we find a single density cloud roughly fitting the pyramidal shape. For excited states, nodes appear in the center of the pyramid and along the axes of the coordinate system. We observe p -wave character for the states ψ_{321} , ψ_{231} ,

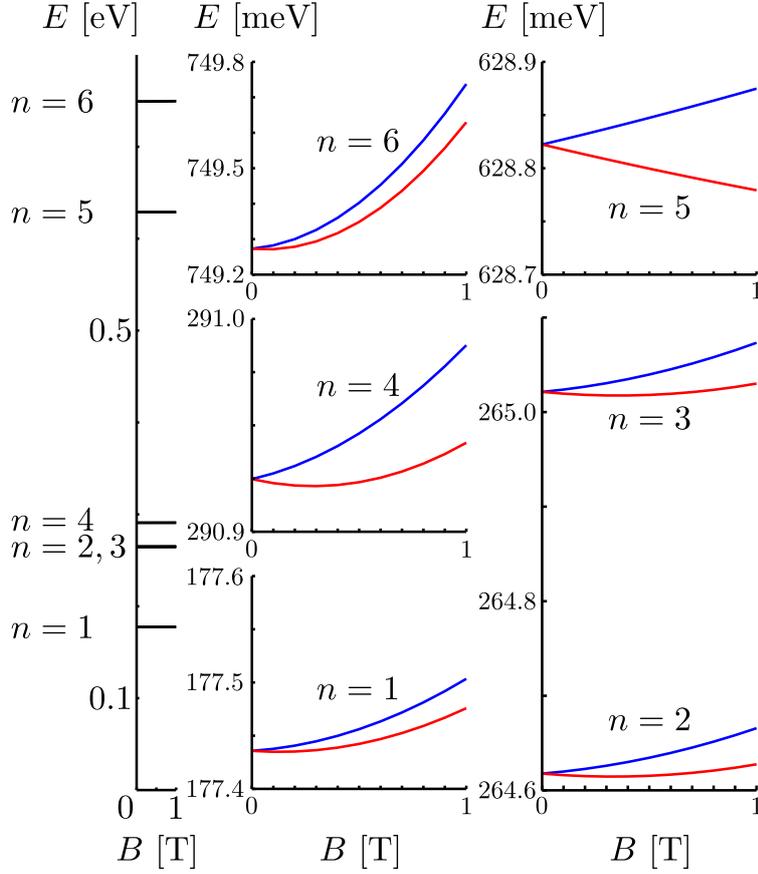


Abbildung 5.3: Left: Spectrum of the lowest six QD levels E_n of \tilde{H}_d^{CB} as a function of the magnetic field $\mathbf{B} = (0, 0, B_z)$, where we increase $|\mathbf{B}| = 0$ T to 1 T. We assume $\mathbf{E} = 0$. Right: Enlarged plots of the \mathbf{B} -dependent splitting of the single QD levels. For most QD levels, except for $n = 5$, we observe a nonlinear dependence of E_n^\pm on \mathbf{B} . *Figure provided by Robert Zielke.*

ψ_{312} , and ψ_{132} ; see Fig. 5.2. The wave functions $\psi_{m_i m_j m_k}$ and $\psi_{m_j m_i m_k}$ with $m_i \neq m_j$ are degenerate and we find that the associated particle densities are of the same form, only with nodes oriented along different axes, i.e., x and y . Further restrictions arising from the pyramid geometry, such as correlations between the coordinates, result in symmetries regarding the quantum numbers, $\psi_{m_i m_i m_j} = \psi_{m_j m_j m_i}$.

Spectra of the CB states in the QD

In Fig. 5.3, we plot the energy spectrum of the low-energy CB states given by \tilde{H}_d^{CB} and examine the behavior of the QD levels as functions of $\mathbf{B} = (0, 0, B_z)$.

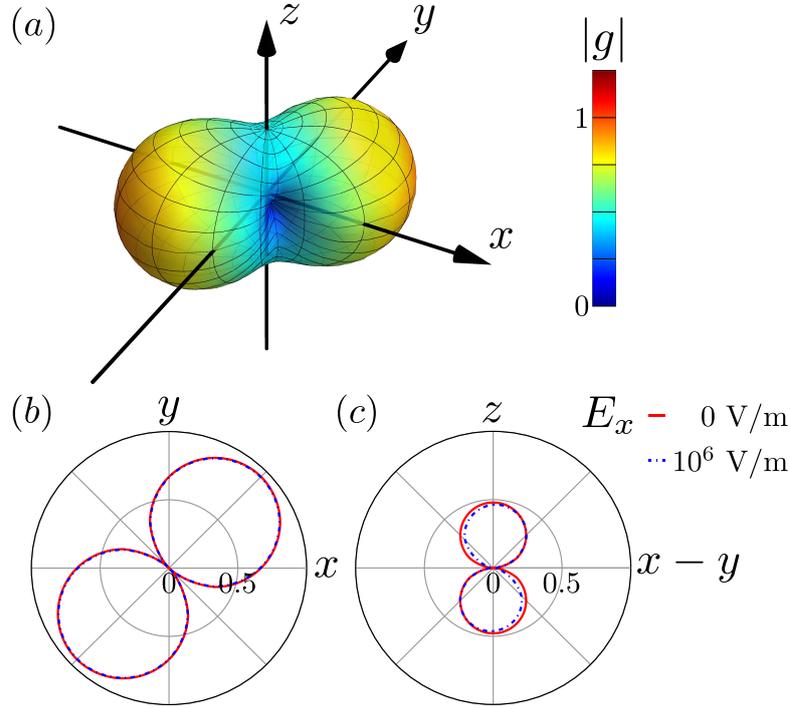


Abbildung 5.4: Ground state g factor $|g_1|$ as a function of the magnetic field direction for $|\mathbf{B}| = 1$ T shown in (a) 3D plot, and cuts along the planes (b) xy , and (c) $(x - y)z$ with electric field $\mathbf{E} = (E_x, 0, 0)$. *Figure provided by Robert Zielke.*

For $|\mathbf{B}| = 0$, we find six degenerate QD levels E_n which split into pairs while increasing \mathbf{B} from 0 to 1 T, where we assume that $\mathbf{E} = 0$. Confinement and strain push the QD levels far apart from each other; hence the \mathbf{B} -induced spin splitting cannot be observed in the full plot, Fig. 5.3 on the left. To circumvent this, we produce magnified plots showing the \mathbf{B} dependence of the single QD levels n , Fig. 5.3 on the right. We note that the splitting of the CB levels, $E_{n+1} - E_n$, is on the order of 100 meV which contrasts the Zeeman splitting, $E_n^+ - E_n^-$, which is on the order of 1 meV or below. For most QD levels E_n^\pm , we observe a clearly nonlinear dependence on \mathbf{B} , indicating a diamagnetic shift of the QD levels [203]. This dependence is not independent of the direction of \mathbf{B} , resulting in an anisotropy associated with the g factor; see Sec. 5.3.

g factor of the CB states in the QD

We discover strong anisotropies for the g factors of electrons confined to low-energy CB states of pyramidal shaped InAs QDs. The g factors of the first six QD levels from the VB edge, g_n with $n = 1, \dots, 6$, are shown as 3D plots and

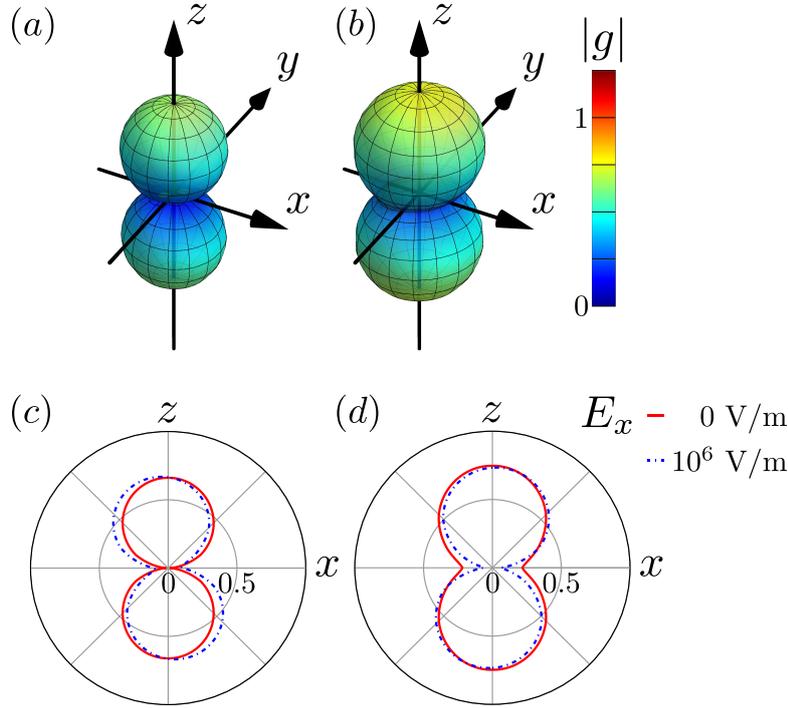


Abbildung 5.5: $|g_2|$ and $|g_3|$ as functions of the magnetic field direction for $|\mathbf{B}| = 1$ T shown in 3D plots for (a) $n = 2$, (b) $n = 3$, and cuts along the xz plane for (c) $n = 2$ and (d) $n = 3$ with electric field $\mathbf{E} = (E_x, 0, 0)$. *Figure provided by Robert Zielke.*

cuts along specific planes in Figs. 5.4 to 5.8 in ascending order. We calculate the g_n for magnetic fields of strength $|\mathbf{B}| = 1$ T. We further apply electric fields of strengths $|\mathbf{E}| = 0$ V/m and $|\mathbf{E}| = 10^6$ V/m along the x axis. In response to an electric field along the x axis the anisotropy axis slightly tilts away from the z axis. To reduce calculation effort, we interpolate between data points, however, we have checked consistency in several cases with non-interpolated plots.

We find anisotropies of various shapes and directions depending on the QD level under consideration. We observe the emerging of three main axes of anisotropy, $x + y$, $x - y$, and z , pointing along crystallographic directions $[110]$, $[1\bar{1}0]$, and $[001]$, respectively. QD levels $n = 1, 4, 6$ ($n = 2, 3$) reveal g -factor maxima along the $x + y$ (z) axes, whereas small g -factor values tend to appear along (in) the $x - y$ axis (xy plane). Along the $x - y$ axis we observe that a special situation arises for $n = 1$; here g approaches a very small value close to but still larger than zero. However, this drop depends strongly on the dot size; see Sec. 5.4. Interestingly, g_5 barely exhibits any anisotropy with maximum

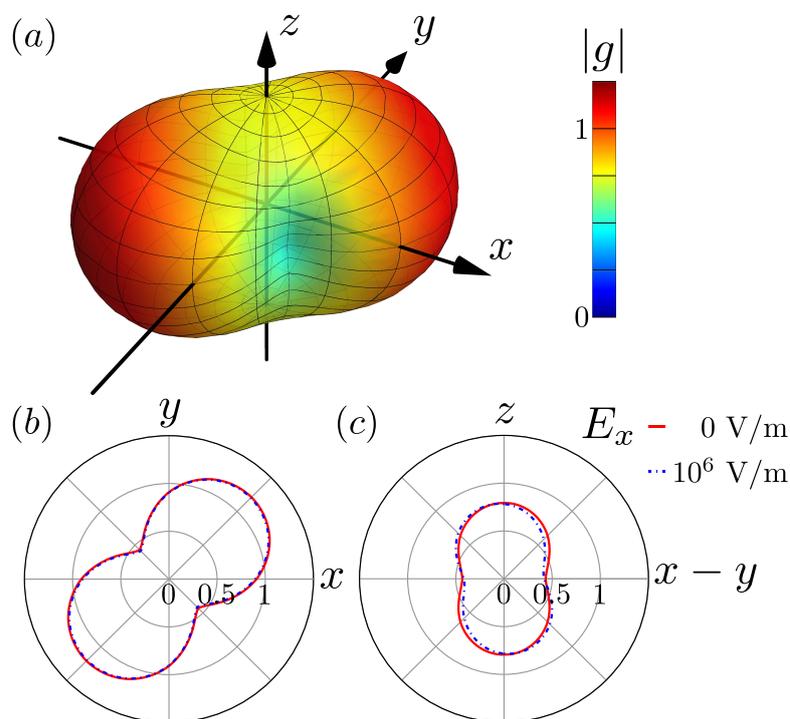


Abbildung 5.6: $|g_4|$ as a function of the magnetic field direction for $|\mathbf{B}| = 1$ T shown in (a) 3D plot, and cuts along the planes (b) xy , and (c) $(x-y)z$ with electric field $\mathbf{E} = (E_x, 0, 0)$. Figure provided by Robert Zielke.

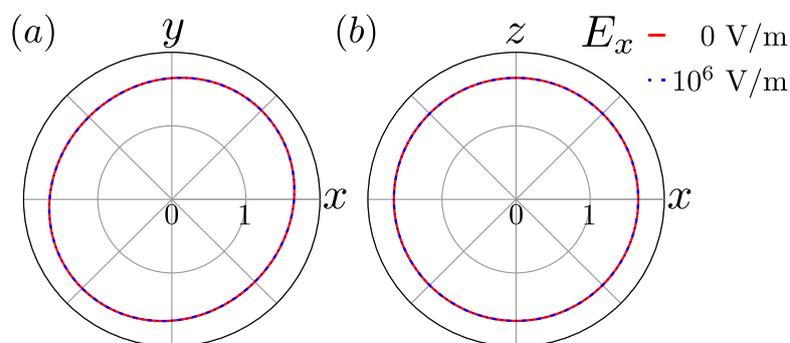


Abbildung 5.7: $|g_5|$ as a function of the magnetic field direction shown for $|\mathbf{B}| = 1$ T in cuts along the planes (a) xy , and (b) xz with electric field $\mathbf{E} = (E_x, 0, 0)$. Here we omit the 3D plot since the g factor shows a spherical distribution, where such a plot does not yield further insight. Figure provided by Robert Zielke.

values at the $x + y$ axis and minimum values at the $x - y$ axis; see Fig. 5.7. This is in contrast to g_6 , where we note a considerable increase of the g -factor values and again a significant anisotropy. Note the change of the color scale

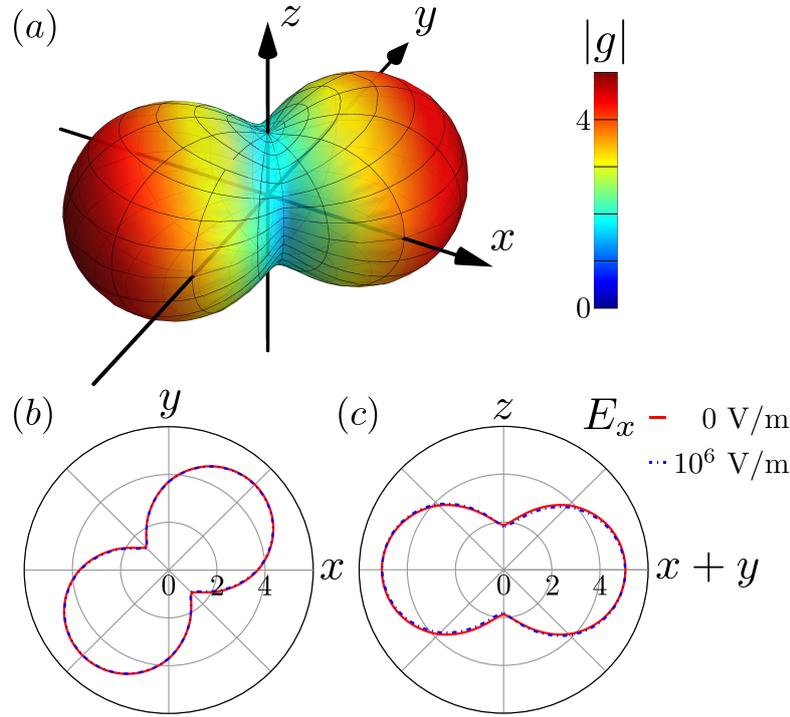


Abbildung 5.8: $|g_6|$ as a function of the magnetic field direction for $|\mathbf{B}| = 1$ T shown in (a) 3D plot, and cuts along the planes (b) xy and (c) $(x+y)z$ with electric field $\mathbf{E} = (E_x, 0, 0)$. Note that the color scale changed because $|g_6|$ reaches larger values than the $|g_n|$ of the QD levels with $n < 6$. *Figure provided by Robert Zielke.*

in Fig. 5.8. In general, we observe a dependence of the absolute values of the g_n on the QD size; see Sec. 5.4.

5.4 Discussion

In this section, we comment on the probability distributions of pyramidal QDs calculated in Sec. 5.3. Furthermore, we discuss the \mathbf{B} dependence of both spectrum and g factor of the CB states in the QD presented in Secs. 5.3 and 5.3, respectively.

Probability distribution of the wave function

The wave functions of the lowest states exhibit the structure of cuboidal wave functions adapted to the pyramidal shape of the enclosing QD. We definitely observe the ground state as well as excited states. This is consistent with the method used for the construction of the wave functions. Note that the wave

functions $\psi_m(\mathbf{r})$ are not exact eigenfunctions of the Schrödinger equation. However, the boundary conditions are satisfied and the corresponding energies, see Eq. (5.3), are smaller than the energies of known analytical solutions of the Schrödinger equation provided that the correct boundary conditions are taken into account [193]. Due to the method of construction, we find that the wave functions do not vanish at the diagonal planes $(x+y)z$ and $(x-y)z$, respectively, as was observed in Ref. [193]. Furthermore, the authors of the work presented in Ref. [193] explicitly state that the obtained set of wave functions is incomplete; solutions with a finite density at the center of the pyramid are not contained. In particular, a distinct ground state is missing. From this we conclude that our set of wave functions is more suitable to describe low-energy states in pyramidal QDs. Numerical calculations of QD wave functions usually include piezoelectric potentials and specific material properties directly from the beginning, which complicates a direct comparison [12, 191]. However, compared to numerical calculations without strain as performed in Ref. [12], where the wave functions extend into a wetting layer, and Ref. [191], where no intermixing with a wetting layer is observed, we report similar shapes of the probability distributions with our analytical ansatz. Even though we apply this simplistic model, we recover the effects recently observed in experiments to a very good degree [181]; see Sec. 5.4.

Spectra of the CB states in the QD

After diagonalizing \tilde{H}_d^{CB} , we find states in the CB of the QD which are degenerate for $|\mathbf{B}| = 0$ and split into pairs by an increasing magnetic field. These energy levels exhibit a quadratic dependence on \mathbf{B} . We note that the direction of the magnetic field is important to the exact behavior of the splitting of the QD levels. Due to the highly admixed nature of the final eigenstates of \tilde{H}_d^{CB} , which consist of CB and VB states of the basis introduced for H_d in Eq. (5.5), we find ourselves unable to comment on the exact shape of the n th eigenfunction. For illustrative plots of the electron wave function in considerably (one order of magnitude) smaller QDs from numerical and experimental studies, we refer the interested reader to Refs. [191] and [204].

g factor of the CB states in the QD

The reported anisotropy in our system stems from several effects. The first effect is the mixing of CB and VB states caused by the confinement potential and intrinsic material parameters of the QD. This mixing is further influenced

by the second effect, a change of gaps between the bands $|j, \pm\rangle$ due to strain. The intrinsic strain fields in the QD impose additional constraints on the system yielding a reduction of the symmetry of the level splitting with respect to the direction of \mathbf{B} . Furthermore, the strain fields reduce the symmetry class of the pyramid along the z axis from C_4 to C_2 [12]. This reduction of the symmetry class agrees well with the observed anisotropy of the g_n in our work. Additionally, effects due to the orbital coupling of \mathbf{B} may have an effect on g . For $|\mathbf{B}| = 1$ T, we find that the magnetic length $l_B = \sqrt{\hbar/e|\mathbf{B}|} \sim 25$ nm is much smaller than the dot size characterized by $a = 50$ nm; hence Landau levels form. However, we took this into account by including H_B into our Hamiltonian; see Eq. (5.1). Compared to experimental results [181], we observe very small g factors, mainly $g_n < 2$. However, small g -factor values, in particular a zero crossing of g due to the transition from the bulk value $g_{\text{bulk}} \approx -14.9$ to the free electron value $g_{\text{free}} = +2$, have also been reported for circular and elliptical InAs QDs [196, 197]. This transition is characterized as a function of the band gap between the CB and VB in the QD. In fact, we find a comparable magnitude of the g -factor values considering the band gap present in our system. In general, decreasing the QD size leads to a decrease of the CB-VB admixture and the g -factor values ultimately yield the free electron value, $g_{\text{free}} = +2$. On the other hand, when increasing the QD size the g -factor values will finally approach the bulk value, $g_{\text{bulk}} \approx -14.9$. Considering these two limits and assuming that the g factor is a continuous quantity, zero values of g will be observed eventually [196, 197].

5.5 Comparison to experiment

In this section, we compare our results to recent experimental observations of the three-dimensional g -factor anisotropy in self-assembled InAs QDs by Takahashi *et al.*; see Ref. [181]. The anisotropy of the QD g factor is usually extracted by transport measurements for different magnetic field directions [181, 200]. The basic setup of these experiments consists of a QD which is tunnel coupled to two leads. An additional back-gate creates an electric field parallel to the growth direction. The back-gate voltage is used to select the QD level participating in the transport by changing the chemical potential of the QD. Furthermore, the tunneling rates depend on the different g factors of QD and leads [205]. We first point out that the QD considered in Ref. [181] is rather a half pyramid due to the applied gates. Thus, deviations of the absolute value of g compared to our findings are not unexpected. Such deviations increase

even further due to different dot sizes. However, we find good qualitative agreement when accounting for the different confinement geometries in the following way. One can perform a coordinate transformation in order to align the axes of the upright pyramid considered above and the half-pyramid of Ref. [181]. Indeed, a rotation of 135° around the y axis aligns the symmetry axes of both systems in first approximation. We observe now that the g -factor anisotropies of the QD levels $n = 2, 3$ (Fig. 5.5) agree well with regions I and II of the charge stability diagram reported by Takahashi *et al.* in Ref. [181]. In region III they also find a state with a spherical distribution of the g factor similar to our calculation for QD level $n = 5$. Furthermore, they report measurements of a symmetrically covered upright pyramid as well. In this case the axes and shapes of the anisotropy are directly comparable to our results. The associated g -factor anisotropy agrees well with our findings for QD levels $n = 2, 3$. In general, due to confinement and strain, the QD size and shape have a strong influence on characteristic quantities such as spectrum and g factor, both absolute value and anisotropy. However, we find good qualitative agreement between our model calculation and the measurements. This is not surprising since both consider square-based pyramids which conserve the main anisotropy axes independent of the QD size. Finally, we point out that our model further predicts different shapes of the g -factor anisotropy depending on the QD levels – in particular, shapes not yet observed in experiments, such as the ones described for the QD levels $n = 1, 4, 6$.

5.6 Conclusion

In conclusion, we have found trial wave functions satisfying hard-wall boundary conditions for a pyramidal QD geometry. We calculated the associated particle density distributions of the low-energy states and found a ground-state-like, s symmetric state of lowest energy, as well as excited states with nodes along the coordinate axes of the system and at the center of the QD. We argued that these wave functions provide a good basis for analytical calculations of QD states. Furthermore, we have presented 8-band calculations to derive the spectrum of low-energy CB states in the QD. The magnetic field induced splitting of the QD levels shows a nonlinear dependence on the magnetic field and strong anisotropies depending on the direction of the field. Starting from this, we have calculated the g factor of low-energy electrons in self-assembled InAs QDs subject to externally applied electric and magnetic fields. We calculated the g factor for all possible spatial orientations of the

magnetic field and found distinct anisotropies. In particular, we showed that the anisotropies include configurations where the g factor drops down to values close to zero. Furthermore, we observed that the shape of the anisotropies depends on the QD level n and that the maximal values of g_n increase with n . Finally, we showed that our results are in good qualitative agreement with recent measurements. From these findings we conclude that the direction of magnetic fields applied to QDs can be used to control the splitting of qubit states efficiently and hence should prove useful for the manipulation of qubits in such QDs.

Acknowledgments

We thank Christoph Kloeffel, Markus Samadashvili, Peter Stano, Dimitrije Stepanenko, and Seigo Tarucha for useful discussions. We acknowledge support from the Swiss NF, the NCCR QSIT, and IARPA.

Teil II

**One-dimensional systems:
Nanowires**

Strongly interacting holes in Ge/Si nanowires

Adapted from:

F. Maier, T. Meng and D. Loss,
‘Strongly interacting holes in Ge/Si nanowires’,
Phys. Rev. B **90**, 155437 (2014).

We consider holes confined to Ge/Si core/shell nanowires subject to strong Rashba spin-orbit interaction and screened Coulomb interaction. Such wires can, for instance, serve as host systems for Majorana bound states. Starting from a microscopic model, we find that the Coulomb interaction strongly influences the properties of experimentally realistic wires. To show this, a Luttinger liquid description is derived based on a renormalization group analysis. This description in turn allows to calculate the scaling exponents of various correlation functions as a function of the microscopic system parameters. It furthermore permits to investigate the effect of Coulomb interaction on a small magnetic field, which opens a strongly anisotropic partial gap.

6.1 Introduction

In the past decades, semiconductor nanowires (NWs) have proven to be a versatile platform for the engineering of nanoscale systems, both as intrinsically one-dimensional (1D) channels, and as hosts for NW quantum dots (QDs). So far, NWs have predominantly been grown using III-V compounds, which can be operated both in the electron regime [24, 115–121], and the hole regime [134]. Recently, a new class of NWs, made of a cylindrical Ge core and a Si shell [122–128, 130–132], and ultrathin triangular Ge NWs on a Si substrate [133], have emerged as promising alternatives to III-V NWs. The core/shell NWs can be grown with core diameters of 5 – 100 nm, and shell thicknesses of 1 – 10 nm. Inside the core, a 1D hole gas accumulates [123, 142], and the p -wave symmetry of the hole Bloch states results in an unusually large and tunable Rashba-type spin-orbit interaction (SOI) [23]. Applying a magnetic field allows one to access a helical regime [23] susceptible to the formation of Majorana zero-energy bound states (MBS) when the NW is proximity coupled to an s -wave superconductor [206]. Finally, when grown nuclear spin free, these systems have significantly reduced hyperfine induced decoherence effects. Experimentally, high mobilities [124, 131], long mean free paths [123], proximity-induced superconductivity [125], and signatures of the tunable Rashba SOI [129] have been identified. Longitudinal confinement has been demonstrated to create tunable single and double QDs [126], with anisotropic and confinement dependent g factors [127, 128], short SOI lengths [207], as well as long singlet-triplet relaxation times [132] and hole spin coherence times [208]. Holes confined to such QDs have furthermore been predicted to exhibit strongly anisotropic, tunable g factors and long spin phonon relaxation times [209], and have been proposed as a platform for quantum information processing [210].

In this chapter, the effects of hole-hole interactions, and their Luttinger liquid description in Ge/Si core/shell NWs are, to the best of our knowledge, addressed and quantified for the first time based on a concrete microscopic model. We focus on the single subband regime most relevant for the emergence of MBS. After explicitly evaluating the interaction matrix elements for a realistic geometry, we derive the Luttinger liquid description of the NW, and calculate the interaction dependent scaling exponents of various correlation functions for our microscopic model. The scaling exponents show a weak dependence on the magnitude of an applied electric field, which tunes the SOI strength. This is contrasted by a strong dependence on the NW para-

eters. The exponents differ substantially from their non-interacting value, thus revealing rather strong interaction effects. As an example for experimental implications of Luttinger liquid physics beyond the scaling of correlation functions, we finally analyze the renormalization of the partial gap around zero momentum resulting from an applied magnetic field. This partial gap precisely corresponds to the helical regime susceptible to the formation of MBS in a superconducting hybrid device [206]. We find that hole-hole interactions lead to a sizable enhancement of the gap (thus implying more stable MBS in an interacting system), which is furthermore strongly anisotropic.

The outline of this chapter is as follows. In Sec. 6.2 we introduce the effective 1D Hamiltonians describing holes in Ge/Si NWs interacting via Coulomb repulsion and distill an effective lowest-energy Hamiltonian. We bosonize the latter in Sec. 6.3 and, in Sec. 6.4, analyze the exponents of the correlation functions regarding the dependence on the applied electric field and NW parameters. In Sec. 6.5, we examine the partial gap opened by an external magnetic field and its dependence on the electric field and the direction of the magnetic field. For technical details we refer to App. E.

6.2 Model

1D hole Hamiltonian

As a first step, we derive an effective theory for the single subband regime of a Ge/Si core/shell NW in the presence of Coulomb interactions. Our starting point is a more complex model [23] for a NW with core (shell) radius R (R_s) aligned with the z axis of the coordinate system, and exposed to an electric field perpendicular to the NW axis, $\mathbf{E} = E_\perp(\cos \varphi_E, \sin \varphi_E, 0)$. A possibly applied magnetic field will be added in a later step. The non-interacting part of this setup is well described by an effective quasi-1D Hamiltonian $H_0 = \int dz \mathcal{H}_0$ with

$$\mathcal{H}_0 = \Psi^\dagger(z) [\mathcal{H}_{\text{LK}} + \mathcal{H}_{\text{strain}} + \mathcal{H}_{\text{R}} + \mathcal{H}_{\text{DR}} - \mu] \Psi(z) , \quad (6.1)$$

where μ denotes the chemical potential, and with \mathcal{H}_0 being written in the basis $\{\Psi_{g_+}(z), \Psi_{g_-}(z), \Psi_{e_+}(z), \Psi_{e_-}(z)\}$. The indices g_\pm, e_\pm comprise the band (g, e) and pseudospin ($+, -$) labels, and the annihilation operators are given by $\Psi_i(z) = \sum_{k_z} e^{ik_z z} c_{i,k_z}$, with c_{i,k_z} being the annihilation operator of a hole state i with momentum k_z along the NW. The Luttinger-Kohn and strain Hamiltonian densities read $\mathcal{H}_{\text{LK}} + \mathcal{H}_{\text{strain}} = A_+(k_z) + A_-(k_z)\tau_z + Ck_z\tau_y\sigma_x$, with

τ_i and σ_i being the Pauli matrices acting in the band and pseudo-spin space, respectively. Here, $A_{\pm}(k_z, \eta) \equiv \hbar^2 k_z^2 (m_g^{-1} \pm m_e^{-1})/4 \pm \Delta/2$, with Planck's constant \hbar , and with effective masses $m_g \simeq m_0/(\gamma_1 + 2\gamma_s)$ and $m_e = m_0/(\gamma_1 + \gamma_s)$. The bare electron mass is denoted by m_0 , and γ_1 and γ_s are the Luttinger parameters in spherical approximation. For Ge, $\gamma_1 = 13.35$ and $\gamma_s = 5.11$ [147]. The level splitting between the g_{\pm} and e_{\pm} states is $\Delta \equiv \Delta_{\text{LK}} + \Delta_{\text{strain}}(\eta)$ with relative shell thickness $\eta \equiv (R_s - R)/R$, confinement induced $\Delta_{\text{LK}} = 0.73\hbar^2/(m_0 R^2)$ and the strain dependent splitting $\Delta_{\text{strain}}(\eta) \simeq 0 - 30$ meV. The off-diagonal coupling with coupling constant $C = 7.26\hbar^2/(m_0 R)$ is a direct consequence of the strong atomic level SOI. The direct Rashba SOI, $\mathcal{H}_{\text{DR}} = eU E_{\perp} (\tau_x \sigma_z \cos \varphi_E - \tau_y \sin \varphi_E)$, where $U = 0.15R$, results from direct, dipolar coupling of \mathbf{E} to the charge of the hole. The conventional Rashba SOI reads $\mathcal{H}_{\text{R}} = \alpha_R E_{\perp} [S(\tau_x \sigma_z \cos \varphi_E - \tau_y \sin \varphi_E) + B_+(k_z) + B_-(k_z)\tau_z]$, with $B_{\pm}(k_z) \equiv k_z T (\sigma_x \sin \varphi_E + \sigma_y \cos \varphi_E)/2 \mp 3k_z (\sigma_x \sin \varphi_E - \sigma_y \cos \varphi_E)/8$, where $T = 0.98$, $S = 0.36/R$, and $\alpha_R = -0.4 \text{ nm}^2 e$ with elementary charge e . Note that $eU/(\alpha_R S) \simeq -1.1R^2 \text{ nm}^{-2}$, hence \mathcal{H}_{DR} dominates \mathcal{H}_{R} by one to two orders of magnitude for $R = 5 - 10$ nm. Diagonalizing the full (4×4) matrix Hamiltonian H_0 yields the eigenenergies $E_{g'_+}$, $E_{g'_-}$, $E_{e'_+}$ and $E_{e'_-}$. The associated annihilation operators are $\Psi_{g'_+}(z)$, $\Psi_{g'_-}(z)$, $\Psi_{e'_+}(z)$, and $\Psi_{e'_-}(z)$, which are linear combinations of the original annihilation operators introduced below Eq. (6.1). The coefficients of the linear combinations depend strongly on the NW parameters R and Δ , and both magnitude and direction of \mathbf{E} . In the following, we assume the chemical potential to be placed below the bottom of the upper bands e'_{\pm} , and therefore focus on the low-energy Hamiltonian in the subspace spanned by $\{\Psi_{g'_+}(z), \Psi_{g'_-}(z)\}$.

Coulomb interaction

Next, we generalize this Hamiltonian to the interacting case. For our concrete microscopic model, we assume the holes to interact via Coulomb repulsion, and take the latter to be screened by mirror charges in the nearby gates. The associated potential for a hole located at \mathbf{r} interacting with a hole located at \mathbf{r}' in the presence of a mirror charge at \mathbf{r}_{mc} is given by

$$V(\mathbf{r}, \mathbf{r}', \mathbf{r}_{\text{mc}}) = \frac{e^2}{4\pi\epsilon_0\epsilon_r} \left[\frac{1}{|\mathbf{r} - \mathbf{r}'|} - \frac{1}{|\mathbf{r} - \mathbf{r}_{\text{mc}}|} \right], \quad (6.2)$$

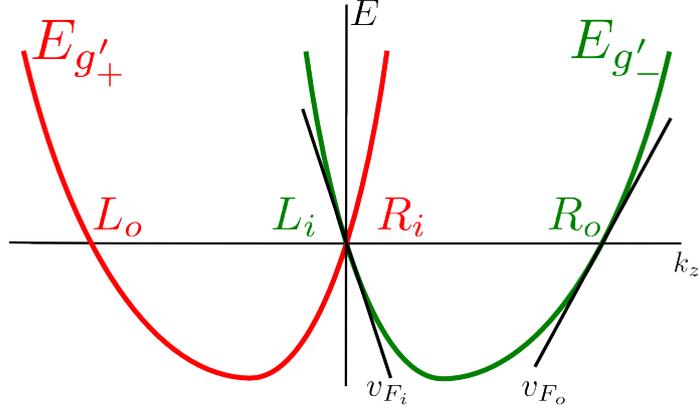


Abbildung 6.1: Sketch of the low-energy dispersions $E_{g'_+}$ and $E_{g'_-}$ as functions of the momentum k_z along the NW for a finite field E_\perp . The Fermi velocities v_{F_i} and v_{F_o} for the inner and outer modes differ in the general case, i.e., $v_{F_i} \neq v_{F_o}$.

with vacuum permittivity ε_0 , and relative permittivity ε_r . For Ge, $\varepsilon_r \approx 16$ [211]. In the initial (4×4) basis, the interaction Hamiltonian thus reads

$$H_c = \frac{1}{2} \sum_{ijkl} \iint dz dz' \Psi_i^\dagger(z) \Psi_j^\dagger(z') \times \left[\int dq V_{1D}^{ijkl}(q) e^{iq[z-z']} \right] \Psi_k(z') \Psi_l(z), \quad (6.3)$$

with $i, j, k, l = g_\pm, e_\pm$, and q being the wavevector along the NW. The interaction matrix elements $V_{1D}^{ijkl}(q)$ of H_c are obtained by integrating out the transverse part of $V(\mathbf{r}, \mathbf{r}', \mathbf{r}_{\text{mc}})$ using the three-dimensional wave functions of holes in Ge/Si NWs derived in Ref. [23]. A more detailed sketch of this calculation is given in Appendix E.1. Finally, we project the full (4×4) interaction Hamiltonian H_c onto the diagonalized low energy subspace E'_{g_\pm} , thus arriving at the interacting effective model for the single subband regime of a Ge/Si core/shell NW.

6.3 Bosonization

The low energy excitations of this interacting 1D system are given by collective bosonic density waves rather than individual fermionic quasiparticles [81]. To distill the related Luttinger liquid Hamiltonian, we linearize the non-interacting part of the spectrum, depicted in Fig. 6.1, around the Fermi points. In this process, we only retain low energy excitations by introducing a momentum cutoff \hbar/α relative to the Fermi points, where α denotes the short distance

cutoff length. Because of the SOI, the pseudospin bands g'_+ and g'_- are split in momentum space. We decompose the operators $\Psi_{g'_\pm}(z)$ into right (R_j) and left (L_j) moving modes associated with the low energy excitations close to the inner ($j = i$) and outer ($j = o$) Fermi points, $\Psi_{g'_+}(z) \simeq R_i(z)e^{ik_{F_i}z} + L_o(z)e^{-ik_{F_o}z}$ and $\Psi_{g'_-}(z) \simeq R_o(z)e^{ik_{F_o}z} + L_i(z)e^{-ik_{F_i}z}$, where the inner and outer Fermi wave numbers are $k_{F_{i,o}}$. The slopes of the spectrum at these points define the Fermi velocities v_{F_i} and v_{F_o} . These differ because the admixing of the higher energy bands e_\pm renders the bands g'_\pm non-parabolic. Since we are eventually interested in the renormalization of the partial gap opened by a small magnetic field, we furthermore choose the chemical potential to be pinned to the crossing point of $E_{g'_+}$ and $E_{g'_-}$. We emphasize, however, that our model is valid for arbitrary values of μ , with the exception of μ being close to the bottom of the band, where the non-linearity of the spectrum becomes important for the low-energy excitations.

While the projection of the non-interacting Hamiltonian H_0 on the low-energy modes $R_{i,o}$ and $L_{i,o}$ simply reads $H_0 \approx \int dz \sum_{s=i,o} v_{F_s} (R_s^\dagger \partial_z R_s - L_s^\dagger \partial_z L_s)$, the interaction Hamiltonian H_c demands a more careful treatment. We project H_c on the low-energy modes $R_{i,o}$ and $L_{i,o}$, thereby dropping rapidly oscillating terms, and classify the remaining $V_{1D}^{ijkl}(q)$ according to the standard g -ology [81]. This translates $V_{1D}^{ijkl}(q)$ to the interaction matrix elements g_{n_f} with indices $n = 1, 2, 4$, and $f = i, o, io$, which couple only inner (i), only outer (o), or inner and outer (io) modes. Note that we observe several matrix elements corresponding to g_1 processes coupling the inner and outer modes, we label them $g_{1_{ioj}}$, $j = 1, 2, 3, 4$, in order of appearance. With these definitions, the projection of H_c reads $H_c = \int dz (\mathcal{H}_1 + \mathcal{H}_2 + \mathcal{H}_4)$, with

$$\mathcal{H}_2 = g_{2_i} \rho_{R_i} \rho_{L_i} + g_{2_o} \rho_{L_o} \rho_{R_o} + g_{2_{io}} (\rho_{L_i} \rho_{R_o} + \rho_{L_o} \rho_{R_i}), \quad (6.4)$$

$$\mathcal{H}_4 = \frac{g_{4_i}}{2} (\rho_{R_i}^2 + \rho_{L_i}^2) + \frac{g_{4_o}}{2} (\rho_{R_o}^2 + \rho_{L_o}^2) \quad (6.5)$$

$$+ g_{4_{io}} (\rho_{R_i} \rho_{R_o} + \rho_{L_i} \rho_{L_o}),$$

$$\mathcal{H}_1 = 2g_I (R_i^\dagger L_i^\dagger L_o R_o + \text{h.c.}) \quad (6.6)$$

$$- g_{1_{io1}} (\rho_{R_i} \rho_{L_o} + \rho_{R_o} \rho_{L_i}) - g_{1_{io2}} (\rho_{L_o} \rho_{L_i} + \rho_{R_o} \rho_{R_i}).$$

where $g_I = (g_{1_{io3}} - g_{1_{io4}})/2$, and with $\rho_{r_j} = r_j^\dagger r_j$ ($r = R, L$). Note that we have dropped the terms proportional to g_{1_i} and g_{1_o} because their matrix elements vanish, while we obtain $g_{2_f} = g_{4_f}$, $g_{1_{io1}} = g_{1_{io4}}$, and $g_{1_{io2}} = -g_{1_{io3}}$.

We thus find that as usual [81], the Coulomb repulsion gives rise to several terms proportional to squares of the fermionic densities ρ_{r_j} , plus the term proportional to g_I . We bosonize these interaction terms by ex-

pressing the fermionic single-particle operators as $r_s = U_{r,s}(\sqrt{2\pi\alpha})^{-1} \times e^{-i/2[(1+s)(r\phi_i - \theta_i) + (1-s)(r\phi_o - \theta_o)]}$, where $r = R, L \equiv +1, -1$ labels the chirality, and $s = i, o \equiv +1, -1$ denotes the inner/outer-pseudospin, while $U_{r,s}$ are Klein factors (unessential for our discussion). The bosonic fields ϕ_s relate to the integrated density of $s = i, o$ particles, while the canonically conjugate fields θ_s are proportional to their current. In terms of the bosonic fields, the Hamiltonian takes the form $H = \int dz (\Psi_\phi^\dagger \mathcal{H}_\phi \Psi_\phi + \Psi_\theta^\dagger \mathcal{H}_\theta \Psi_\theta) / 2\pi + \int dz g_I \cos[2(\theta_o - \theta_i)] / (\pi\alpha)^2$, where $\Psi_\phi = (\partial_z \phi_o, \partial_z \phi_i)^T$, $\Psi_\theta = (\partial_z \theta_o, \partial_z \theta_i)^T$, and

$$\mathcal{H}_\phi = \begin{pmatrix} v_{F_o} + \frac{g_{4_o} + g_{2_o}}{2\pi} & \frac{g_{4_{io}} + g_{2_{io}} - g_{1_{io1}} - g_{1_{io2}}}{2\pi} \\ \frac{g_{4_{io}} + g_{2_{io}} - g_{1_{io1}} - g_{1_{io2}}}{2\pi} & v_{F_i} + \frac{g_{4_i} + g_{2_i}}{2\pi} \end{pmatrix}, \quad (6.7a)$$

$$\mathcal{H}_\theta = \begin{pmatrix} v_{F_o} + \frac{g_{4_o} - g_{2_o}}{2\pi} & \frac{g_{4_{io}} - g_{2_{io}} + g_{1_{io1}} - g_{1_{io2}}}{2\pi} \\ \frac{g_{4_{io}} - g_{2_{io}} + g_{1_{io1}} - g_{1_{io2}}}{2\pi} & v_{F_i} + \frac{g_{4_i} - g_{2_i}}{2\pi} \end{pmatrix}. \quad (6.7b)$$

The quadratic sector of the Hamiltonian can be diagonalized by a canonical transformation, resulting in effective low-energy degrees of freedom with velocities u_p and u_m (see Appendix E.2), while the sine-Gordon term $\sim g_I$ is analyzed using a standard perturbative renormalization group (RG) approach [81]. Because we choose to fix the chemical potential at the crossing point of $E_{g'_+}$ and $E_{g'_-}$, our calculation is restricted to sufficiently large electric fields E_\perp such that g_I can be treated as a perturbation ($2g_I / (u_p + u_m) \ll 1$). For smaller E_\perp one of the velocities, u_m , vanishes, and the dimensionless g_I becomes non-perturbatively large. With this restriction in mind, we find that g_I is an RG irrelevant perturbation in the regime described by our calculation.

6.4 Exponents of the correlation functions

After integrating the RG flow of g_I to weak coupling, we evaluate various correlation functions $\langle O_j^\dagger(r) O_j(0) \rangle$ for the charge and spin density waves ($j = \text{CDW, SDW}$), and the singlet and triplet superconducting fluctuations ($j = \text{SS, TS}$) [81] (see Appendix E.2), where the spin is the pseudospin distinguishing the bands g_\pm' (as detailed in Appendix E.2, the correlation functions for $\text{SDW}_{x,y}$, SS , and TS_z comprise two terms with slightly different exponents). The scaling exponents of these correlation functions are depicted in Fig. 6.2 as functions of the applied field E_\perp for one concrete set of NW parameters, and exhibit only a weak dependence on E_\perp (the same is found for other NW parameters). In Fig. 6.3, we furthermore plot the scaling exponents for twelve concrete sets of system parameters at a fixed field E_\perp . In general, our microscopic model predicts that the exponents of the correlation functions show a

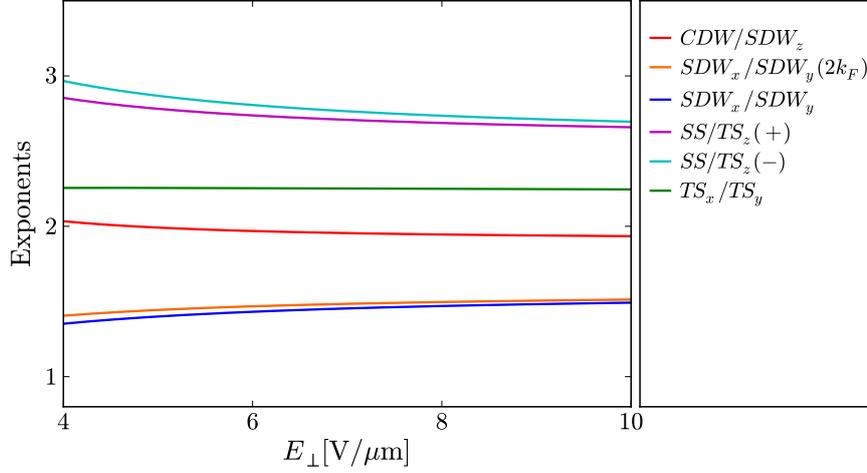


Abbildung 6.2: The exponents of the correlation functions as functions of E_{\perp} for $R = 10$ nm and $\Delta = 8$ meV in the regime where g_I can be treated as perturbation. We fix $\varphi_E = 3\pi/2$ and $\mathbf{r}_{\text{mc}} = (0, |\mathbf{r}_{\text{mc}}|, 0)$ with $|\mathbf{r}_{\text{mc}}| = 100$ nm.

strong dependence on the microscopic NW parameters R and Δ , determined by the core and shell radii. The scaling exponents differ substantially from 2, their non-interacting value, thus indicating strong interaction effects in Ge/Si core/shell NWs. Exponents differing the most from 2 are found for the NW parameter set with the smallest R , indicating that thin NWs show the strongest interactions. We note that when the field E_{\perp} is tuned to sufficiently small values such that the system is pushed outside the perturbative regime, the bosonic RG calculation exhibits a Wentzel-Bardeen singularity [212–215]. As a crosscheck for the absence of singularities in the regime well-described by our calculation, we have performed a fermionic one-loop RG analysis [216, 217], which reproduces the non-singular behavior of the scaling exponents in the perturbative regime. In the E_{\perp} -range where also the fermionic calculation is not valid, the presence or absence of a singularity in the one-loop calculation depends strongly on the chosen NW parameters. For more details, we refer the reader to Appendix E.3.

6.5 Renormalization of the partial gap

As a final example for interaction effects in Ge/Si core/shell NWs, we now turn to the rescaling of the gap opened by a small magnetic field $\mathbf{B} = (B_{\perp} \cos \varphi_E, B_{\perp} \sin \varphi_E, B_z)$. This gap, giving rise to the helical regime susceptible to the formation of MBS, is known to be enlarged by Coulomb interaction

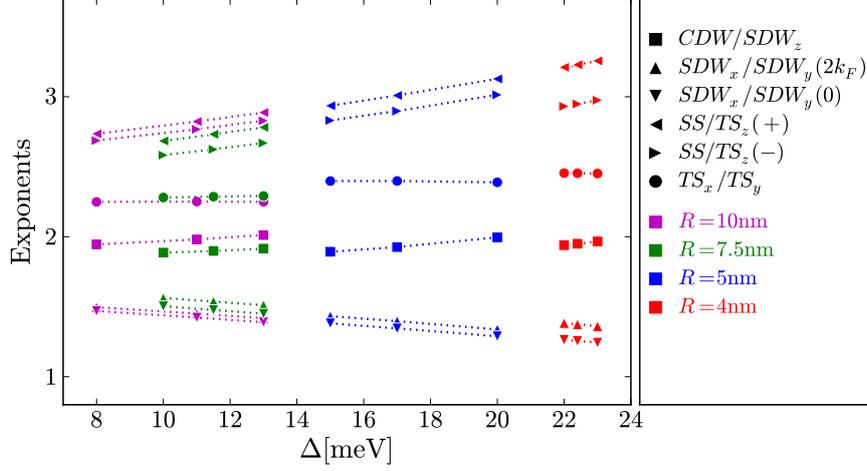


Abbildung 6.3: The exponents of the correlation functions as functions of Δ for four different core radii, $R = 4$ nm (red), $R = 5$ nm (blue), $R = 7.5$ nm (green), and $R = 10$ nm (magenta), where $E_{\perp} = 8$ V/ μm at fixed $\varphi_E = 3\pi/2$ and $\mathbf{r}_{\text{mc}} = (0, |\mathbf{r}_{\text{mc}}|, 0)$ with $|\mathbf{r}_{\text{mc}}| = 100$ nm. For a fixed R and increasing Δ , all exponents besides the ones for the CDW/SDW $_z$ and the TS $_x$ /TS $_y$ become increasingly different from their non-interacting value, 2. The dotted lines are guide to the eyes.

in an electronic Rashba NW [218, 219]. To analyze this effect in our concrete microscopic model with hole-hole interactions, we first introduce the magnetic field Hamiltonian density $\mathcal{H}_B = \mathcal{H}_{B,Z} + \mathcal{H}_{B,\text{orb}}$ in the original fermionic (4×4) basis of \mathcal{H}_0 with $\mathcal{H}_{B,Z} = [C_+ + C_- \tau_z] \sigma_z + [D_+ + D_- \tau_z] \sigma_x \cos \varphi_E - [D_- + D_+ \tau_z] \sigma_y \sin \varphi_E$ and $\mathcal{H}_{B,\text{orb}} = F_z \tau_x \sigma_y + F_{\perp} [\tau_y \cos \varphi_E + \tau_x \sigma_z \sin \varphi_E]$. Here, $C_{\pm} = \mu_B B_z (F \pm G)/2$, $D_{\pm} = \mu_B B_{\perp} (K \pm M)/2$, $F_z = \mu_B B_z D k_z$ and $F_{\perp} = \mu_B B_{\perp} L k_z$ with $F = 1.56$, $G = -0.06$, $K = 2.89$, $M = 2.56$, $D = 2.38R$ and $L = 8.04R$ [23]. We focus on a magnetic field \mathbf{B} in the plane defined by \mathbf{E} and the NW axis since a field perpendicular to this plane does not give rise to the helical regime relevant for MBS, but rather to a spin-polarized state. To bring this field to its bosonized form, we first transform \mathcal{H}_B according to the unitary transformation that diagonalizes the fermionic (4×4) Hamiltonian, and then project it to the lower bands. This yields a Hamiltonian density of the form $\mathcal{H}'_B = \mu_B [g_z B_z \sigma_x + g_{\perp} B_{\perp} \sigma_y]$, with effective g factors g_z and g_{\perp} , and where $\sigma_{x,y,z}$ acts on the pseudospin distinguishing g'_{\pm} . We finally bosonize \mathcal{H}'_B , and obtain

$$\mathcal{H}'_B = \frac{1}{\pi\alpha} \Delta_Z(\vartheta_B) \cos[2\phi_i - \varphi_B], \quad (6.8)$$

with $\Delta_Z(\vartheta_B) = \mu_B (g_z^2 B^2 \cos^2 \vartheta_B + g_{\perp}^2 B^2 \sin^2 \vartheta_B)^{1/2}$, $B_{\perp} = B \sin \vartheta_B$, $B_z = B \cos \vartheta_B$, and $\tan \varphi_B = g_z B_z / (g_{\perp} B_{\perp})$. This sine-Gordon term obeys the RG

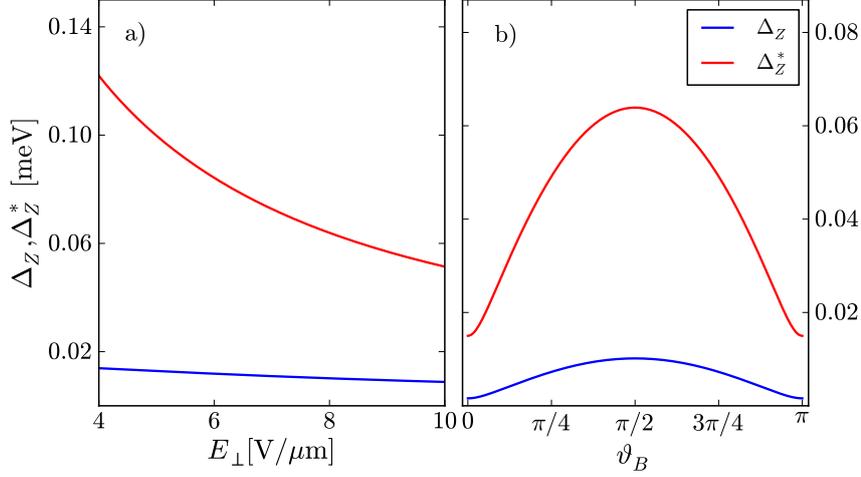


Abbildung 6.4: The bare and rescaled helical gaps Δ_Z and Δ_Z^* for $B = 0.1$ T (a) as functions of E_\perp for $\vartheta_B = \pi/2$ and (b) as functions of ϑ_B for $E_\perp = 8$ V/ μm . We use the NW parameters $R = 7.5$ nm and $\Delta = 13$ meV and fix $\varphi_E = 3\pi/2$ and $\mathbf{r}_{\text{mc}} = (0, |\mathbf{r}_{\text{mc}}|, 0)$ with $|\mathbf{r}_{\text{mc}}| = 100$ nm.

equation $d\Delta_Z/dl = (2 - g_B)\Delta_Z(l)$, where the interaction dependent scaling dimension g_B follows from the diagonalized Hamiltonian. Due to the presence of Coulomb repulsion, we find that g_B is always smaller than its non-interacting value $g_0 = 1$, such that the gap is enhanced by hole-hole interactions. We can thus conclude that hole-hole interactions would stabilize a MBS in the presence of proximity-induced superconductivity, similar to proximitized Rashba NWs for electrons [220, 221]. The RG flow is integrated until the running $\Delta_Z(l)$ grows to the value $\Delta_Z(l)/(\hbar v_{F_i}/\alpha) \sim 1$ [81], signaling the opening of the helical gap. In physical units, this gap has the size $\Delta_Z^* = \Delta_Z^0 (\hbar v_{F_i}/(2\Delta_Z^0 \alpha))^{(1-g_B)/(2-g_B)}$ [219]. In Fig. 6.4 a), we plot both Δ_Z and Δ_Z^* as functions of E_\perp for $B_\perp = 0.1$ T and $B_z = 0$ T, with $\alpha = 5.65$ Å being the lattice constant of Ge [6]. We find that Δ_Z^* depends much stronger on E_\perp than Δ_Z . This can be attributed to the large changes in v_{F_i} for decreasing E_\perp . In Fig. 6.4 b), we finally display Δ_Z and Δ_Z^* for fixed B and E_\perp as functions of ϑ_B , i.e., the direction of \mathbf{B} with respect to the NW, and find that both Δ_Z and Δ_Z^* are strongly anisotropic.

6.6 Conclusions

In this chapter, we have addressed and quantified the effects of hole-hole interactions and their Luttinger liquid description in Ge/Si core/shell NWs, where

we focused on the single subband regime most relevant for the emergence of MBS. We derived the Luttinger liquid description of the NW, and calculated the interaction dependent scaling exponents of various correlation functions. We showed a weak dependence of the scaling exponents on the magnitude of an applied electric field and a strong dependence on the NW parameters. Furthermore, the exponents revealed strong interaction effects since they differ substantially from their non-interacting value with thin NWs showing the strongest deviations. To show the experimental relevance of our results, we analyzed the renormalization of the partial gap around zero momentum resulting from an applied magnetic field which is considerably enhanced by the hole-hole interactions. Additionally, we found that the gap is strongly anisotropic. Regarding the emergence of MBS in the helical regime of superconducting hybrid device, the enhancement of the gap implies more stable MBS in an interacting system.

In conclusion, hole-hole interactions show sizable effects in Ge/Si core/shell NWs and may lead to the stabilization of emerging MBS by enhancing the partial gap.

Acknowledgments

We thank Kevin van Hoogdalem and Christoph Kloeffel for useful discussions, and acknowledge funding from the Swiss NF, NCCR QSIT and through the EC FP7-ICT initiative under project SiSPIN No 323841.

Majorana fermions in Ge/Si hole nanowires

Adapted from:

F. Maier, J. Klinovaja and D. Loss,
‘Majorana fermions in Ge/Si hole nanowires’,
Phys. Rev. B **90**, 195421 (2014).

We consider Ge/Si core/shell nanowires with hole states coupled to an s -wave superconductor in the presence of electric and magnetic fields. We employ a microscopic model that takes into account material-specific details of the band structure such as strong and electrically tunable Rashba-type spin-orbit interaction and g factor anisotropy for the holes. In addition, the proximity-induced superconductivity Hamiltonian is derived starting from a microscopic model. In the topological phase, the nanowires host Majorana fermions with localization lengths that depend strongly on both the magnetic and electric fields. We identify the optimal regime in terms of the directions and magnitudes of the fields in which the Majorana fermions are the most localized at the nanowire ends. In short nanowires, the Majorana fermions hybridize and form a subgap fermion whose energy is split away from zero and oscillates as a function of the applied fields. The period of these oscillations could be used to measure the dependence of the spin-orbit interaction on the applied electric field and the g factor anisotropy.

7.1 Introduction

Quasiparticles with non-Abelian statistics are considered as auspicious candidates for topological quantum computing [97]. Among these, Majorana fermions (MFs), particles that are their own anti-particles, received a large amount of attention during the last years [98, 206]. MFs are predicted to occur in different systems such as fractional quantum Hall systems [95, 97], topological insulators [222–228], nanowires with strong Rashba [86–89] or synthetic [229, 230] spin-orbit interaction (SOI), p -wave superconductors [231], RKKY systems [232–234], and graphene-like systems [235–239]. Recent experiments on MFs [90–94, 240] were performed in Rashba nanowires (NWs) since this type of setup is relatively easy to realize. The majority of these experiments use InSb or InAs NWs because they are presumed to have strong SOI and large g factors, which are necessary prerequisites for the emergence of Majorana bound states in such wires [86, 87]. However, the direct measurement of the SOI strength in one-dimensional NWs is a challenging task [27] and has not yet been performed in the materials mentioned above. In this chapter we focus on a promising alternative, Ge/Si core/shell NWs carrying holes in the Ge core, in which an exceptionally strong electric-field-highly-tunable Rashba SOI is expected [23] and in which the first signatures of a strong SOI were identified experimentally [129].

Ge/Si core/shell NWs, cylindrical NWs with a Ge core and Si shell, attracted a lot of attention recently [122–126, 130–132]. These NWs can be grown with high precision, i.e., with core diameters between 5 – 100 nm and shell thicknesses between 1–10 nm. Due to the large valence band offset between Ge and Si, a one-dimensional (1D) hole gas forms in the core of the NW [123, 142]. The p -type symmetry of the hole Bloch states gives rise to a total angular momentum $J = 3/2$, which results in an unusually large, and electrically tunable Rashba-type SOI [23]. Furthermore, the holes show high mobilities [124, 131], long mean free paths [123], and Coulomb interaction strongly influences their properties [241]. Longitudinal confinement in these NWs results in tunable single and double QDs [126] with anisotropic and confinement-dependent g factors [127, 128], in long relaxation [132] and coherence times [208] as well as in short SOI lengths [207]. Moreover, strongly anisotropic tunable g factors and long spin phonon relaxation times [209] were predicted as well as the usability for quantum information processing based on hole spin qubits [210]. Note that strongly anisotropic and electrically tunable g factors were also observed in SiGe nanocrystals [242, 243]. Most importantly for our work, externally ap-

plied strong magnetic fields allow one to access a helical regime [23], which in combination with the experimentally demonstrated proximity-induced s -wave superconductivity [125] makes Ge/Si core/shell NWs promising candidates to generate MFs.

In the present chapter, we explore the properties of MFs in Ge/Si core/shell NWs starting from a microscopic model [23] that captures the specific NW characteristics such as g factor anisotropy and the dependence of the induced Rashba SOI on the direction and magnitude of the electric field. We extend this microscopic model to account on the same level for a proximity-induced superconductivity, which couples hole states with opposite orbital and angular momentum. We especially focus on the tunability of the SOI that allows us to access the regimes of strong and weak SOI independently of the applied magnetic field and analyze the localization lengths of the MF wave functions in the NW regarding their dependence on magnitude and direction of the applied electric and magnetic fields. The shortest localization lengths can be expected when the fields are tuned to intermediate magnitudes. Due to the g factor anisotropy we predict the shortest localization lengths for the magnetic field pointing perpendicular to the NW axis. In a NW of finite length, the MFs localized at two NW ends overlap [244] and hybridize into an ordinary fermion which is, generally, at non-zero energy. This energy demonstrates an oscillatory behavior [245, 246] as function of the applied electric and magnetic fields that might be used to determine the coupling constants to the electromagnetic field. Finally, we mention in passing that while we focus here on Ge/Si core-shell nanowires, we expect our analysis also to apply (at least qualitatively) to similar structures such as Ge hat-shape-nanowires grown on Si [133].

The outline of the chapter is as follows. In Sec. 7.2, we introduce the effective microscopic 1D model and derive the proximity-induced superconducting coupling of NW hole states. In Sec. 7.3, we determine the localization lengths of MFs for a semi-infinite NW in both the strong and the weak SOI regime and identify field configurations for which the shortest localization lengths can be expected. Lastly, we focus on the energies of hybridized MFs in finite NWs in Sec. 7.4. We present our conclusions in Sec. 7.5. Technical details are deferred to App. F.

7.2 Nanowire Hamiltonian for holes

In this section, we describe the geometry of the system and describe the directions of the applied fields for which MFs can be expected. We introduce

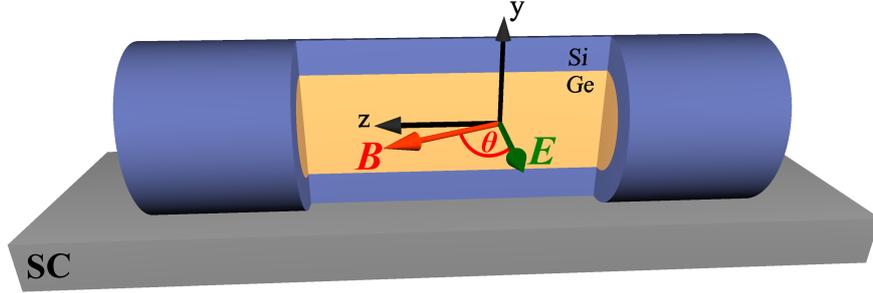


Abbildung 7.1: Sketch of a Ge/Si core/shell NW (cylinder) placed on top of an s -wave superconductor (SC) to induce proximity pairing of the holes in the NW core. The NW axis is chosen to point along the z axis. The applied electric field $\mathbf{E} = (E_x, 0, 0)$ is parallel to the x axis, while the applied magnetic field $\mathbf{B} = (B_x, 0, B_z) \equiv B(\cos\theta, 0, \sin\theta)$ is in the xz plane.

the microscopic model [23] describing holes confined to the core of Ge/Si core/shell NWs and derive an effective lowest-energy subband Hamiltonian and the associated spectrum. Next, we employ a superconductivity pairing Hamiltonian introduced for holes close to the valence band edge in bulk material [89] and derive the corresponding 1D Hamiltonian within the framework of the microscopic model and project this on the subspace of the lowest-energy subband Hamiltonian.

Setup

Throughout this chapter, we consider holes confined to the core of a Ge/Si core/shell NW with core (shell) radius R (R_s) that is positioned on top of an s -wave superconductor as sketched in Fig. 7.1. The NW axis is assumed to point along the z axis. We restrict ourselves to field configurations in which the electric field $\mathbf{E} = (E_x, 0, 0)$ points perpendicular to the NW axis and is parallel to the surface of the superconductor and in which the magnetic field $\mathbf{B} = (B_x, 0, B_z) \equiv B(\cos\theta, 0, \sin\theta)$ is confined to the plane spanned by \mathbf{E} and the NW axis. In this case, the SOI vector, generated by the applied electric field \mathbf{E} , points along the y axis and is always perpendicular to \mathbf{B} . As shown before [86, 87], such a configuration is optimal for generating MFs in NWs. We note that we focus here on the case where the SOI (and the electric field \mathbf{E}) is uniform along the NW. For the effects of a non-uniform SOI we refer to Ref. [247].

Microscopic Hamiltonian

The two hole bands closest to the valence band edge in a Ge/Si core/shell NW are described by an effective 4×4 Hamiltonian [23]

$$H = \sum_{ij} \int dz \Psi_i^\dagger(z) (\mathcal{H}_{ij} + \mu \delta_{ij}) \Psi_j(z), \quad (7.1)$$

with Hamiltonian density

$$\mathcal{H} = \mathcal{H}_{\text{LK}} + \mathcal{H}_{\text{strain}} + \mathcal{H}_{\text{DR}} + \mathcal{H}_{\text{R}} + \mathcal{H}_{B,Z} + \mathcal{H}_{B,\text{orb}}, \quad (7.2)$$

given in the basis $\{\Psi_{g_+}(z), \Psi_{g_-}(z), \Psi_{e_+}(z), \Psi_{e_-}(z)\}$. Here, μ is a tunable chemical potential, and δ_{ij} is the Kronecker delta. The fermionic annihilation operators $\Psi_i(z) = \sum_{k_z} e^{ik_z z} c_{i,k_z}$ can be rewritten in momentum space in terms of c_{i,k_z} , which are the fermionic annihilation operators of a hole state $i \in \{g_\pm, e_\pm\}$ with momentum k_z along the NW. The index g, e refers to the ground and excited bands, and the index \pm refers to the pseudospin.

The Luttinger-Kohn and strain Hamiltonian densities are given by

$$\mathcal{H}_{\text{LK}} + \mathcal{H}_{\text{strain}} = A_+(k_z) + A_-(k_z)\tau_z + Ck_z\tau_y\sigma_x, \quad (7.3)$$

where τ_i and σ_i denote the Pauli matrices for band (g, e) and pseudospin index ($+, -$), respectively. Here, $A_\pm(k_z, \eta) \equiv \hbar^2 k_z^2 (m_g^{-1} \pm m_e^{-1})/4 \pm \Delta/2$, with Planck's constant \hbar and effective masses $m_g \simeq m_0/(\gamma_1 + 2\gamma_s)$ and $m_e = m_0/(\gamma_1 + \gamma_s)$ with m_0 denoting the bare electron mass and γ_1 and γ_s representing the Luttinger parameters in spherical approximation. For Ge, $\gamma_1 = 13.35$ and $\gamma_s = 5.11$ [147]. The level splitting is $\Delta \equiv \Delta_{\text{LK}} + \Delta_{\text{strain}}(\eta)$ with confinement induced $\Delta_{\text{LK}} = 0.73\hbar^2/(m_0R^2)$ and the strain dependent splitting $\Delta_{\text{strain}}(\eta) \simeq 0 - 30$ meV, where the latter depends on the relative shell thickness $\eta \equiv (R_s - R)/R$. The off-diagonal terms, being proportional to the coupling constant $C = 7.26\hbar^2/(m_0R)$, result directly from the strong SOI at the atomic level. The direct Rashba SOI,

$$\mathcal{H}_{\text{DR}} = eUE_x\tau_x\sigma_z, \quad U = 0.15R, \quad (7.4)$$

originates from the direct dipolar coupling of the hole charge to the applied electric field E_x . The conventional Rashba SOI reads

$$\mathcal{H}_{\text{R}} = \alpha_R E_x [S\tau_x\sigma_z + B_+(k_z) + B_-(k_z)\tau_z], \quad (7.5)$$

with $B_\pm(k_z) \equiv k_z T/2\sigma_y \pm 3/8k_z\sigma_y$, where $T = 0.98$, $S = 0.36/R$, and $\alpha_R = -0.4 \text{ nm}^2 e$ with elementary charge e . The parameters S and U of the direct

and conventional SOI, respectively, are related by $eU/(\alpha_R S) \simeq -1.1R^2\text{nm}^{-2}$, hence \mathcal{H}_{DR} dominates \mathcal{H}_R by one to two orders of magnitude for $R = 5\text{--}10\text{ nm}$ [23].

Finally, we include the effect of an applied magnetic field $\mathbf{B} = (B_x, 0, B_z) = B(\cos\theta, 0, \sin\theta)$ by introducing the Hamiltonian densities

$$\mathcal{H}_{B,Z} = [C_+ + C_-\tau_z]\sigma_z + [D_+ + D_-\tau_z]\sigma_x, \quad (7.6)$$

$$\mathcal{H}_{B,\text{orb}} = F_z\tau_x\sigma_y + F_x\tau_y. \quad (7.7)$$

Here, $C_{\pm} = \mu_B B_z/2(F \pm G)$, $D_{\pm} = \mu_B B_x/2(K \pm M)$, $F_z = \mu_B B_z D k_z$ and $F_x = \mu_B B_x L_B k_z$ with $F = 1.56$, $G = -0.06$, $K = 2.89$, $M = 2.56$, $D = 2.38R$ and $L_B = 8.04R$ [23].

Low-energy 2×2 Hamiltonian

In this subsection, we derive an effective lowest-energy subband Hamiltonian for the holes by effectively decoupling the g_{\pm} and e_{\pm} bands introduced above in Sec. 7.2. To achieve this, we perform a Schrieffer-Wolff transformation [6, 248] (SWT) which block-diagonalizes the Hamiltonian and subsequently allows one to truncate the lowest-energy subspace. In general, a SWT is given by a transformation of the form $H \rightarrow \tilde{H} = e^{-S} H e^S$, where S is an anti-Hermitian operator ($S^\dagger = -S$). However, we utilize the SWT in a perturbative manner and begin by subdividing the Hamiltonian density \mathcal{H} into a leading order term $\mathcal{H}_0 = A_+(0) + A_-(0)\tau_z$ and a perturbation $\mathcal{H}' = \mathcal{H} - \mathcal{H}_0$. This choice is justified since the strain induced splitting of the g_{\pm} and e_{\pm} subspaces is by far the largest energy scale present in the system. The perturbing term is further divided into a diagonal (\mathcal{H}_d) and off-diagonal part (\mathcal{H}_{od}) with respect to the two considered subspaces g_{\pm} and e_{\pm} , $\mathcal{H}' = \mathcal{H}_d + \mathcal{H}_{od}$. Next, we construct the operator S such that the SWT rotates \mathcal{H}_{od} into an approximately block-diagonal form. We also expand $e^S \approx 1 + S + S^2/2$ and then approximate S to lowest order by $S \approx S_1$, where S_1 is determined by $[S_1, \mathcal{H}_0] = \mathcal{H}_{od}$. As a result, the approximate block-diagonal Hamiltonian density $\tilde{\mathcal{H}} \approx \mathcal{H}_0 + \mathcal{H}_d - [S_1, \mathcal{H}_{od}] + [S_1, [S_1, \mathcal{H}_0]]/2$ is exact to second order in $(\mathcal{H}_{od})_{ij}/\Delta \ll 1$, where $(\mathcal{H}_{od})_{ij}$ denotes the matrix elements coupling the g_{\pm} and e_{\pm} subspaces. This corresponds to conditions restricting the magnitudes of the applied fields: $Ck_z/\Delta \ll 1$, $eUE_x/\Delta \ll 1$, $\mu_B B_x L k_z/\Delta \ll 1$, and $\mu_B B_z D k_z/\Delta \ll 1$. After truncating, the effective lowest-energy Hamiltonian

is given by $\tilde{H}_{g'} = \sum_{i,j=g'_\pm} \int dz \Psi_i (\tilde{\mathcal{H}}_{g'})_{ij} \Psi_j$, with density

$$\tilde{\mathcal{H}}_{g'} = \begin{pmatrix} \frac{\hbar^2}{2m_{\text{eff}}} k_z^2 - \mu + \mu_B B_z g_z & \mu_B B_x g_x - i E_x k_z \alpha_{\text{eff}} \\ \mu_B B_x g_x + i E_x k_z \alpha_{\text{eff}} & \frac{\hbar^2}{2m_{\text{eff}}} k_z^2 - \mu - \mu_B B_z g_z \end{pmatrix} \quad (7.8)$$

in the associated low-energy basis $\{\Psi_{g'_+}, \Psi_{g'_-}\}$. The new annihilation operators are linear combinations of the original operators introduced below Eq. (7.2), where the associated admixing coefficients depend strongly on the NW parameters R and Δ and on the magnitude and direction of \mathbf{E} and \mathbf{B} .

In Eq. (7.8), we identify an effective kinetic term $\propto m_{\text{eff}}^{-1}$, an effective SOI term $\propto \alpha_{\text{eff}}$, and two terms $\propto g_x, g_z$ describing the effective coupling to the magnetic field,

$$\alpha_{\text{eff}} = T\alpha + \frac{2}{\Delta} C(eU + S\alpha), \quad \frac{\hbar^2}{2m_{\text{eff}}} \approx \frac{\hbar^2}{2m_g} - \frac{C^2}{\Delta}, \quad (7.9)$$

$$g_x = K - \frac{2}{\Delta} L_B C k_z^2, \quad g_z = G - \frac{2}{\Delta} D C k_z^2. \quad (7.10)$$

We note that m_{eff} has an additional weak dependence on \mathbf{B} which is neglected here. Furthermore, we see that the effective g factors $g_i = g_{i0} + g_{i2} k_z^2$ ($i = x, z$) differ strongly in magnitude, which leads to anisotropy, and, in addition, they depend on the momentum k_z .

The Hamiltonian $\tilde{H}_{g'}$ describes the lowest-energy subbands g'_\pm , where all coupling terms to the higher bands are taken into account by introducing effective g factors and SOI coupling. We note that the Hamiltonian density $\tilde{\mathcal{H}}_{g'}$ resembles closely the Hamiltonian densities introduced in other works [86, 87, 249] to describe electrons in Rashba SOI NWs in the presence of a magnetic field. However, the dependence on the direction and strength of \mathbf{E} and \mathbf{B} is much more involved in the case of Ge/Si core/shell NWs.

The spectrum of $\tilde{H}_{g'}$ is given by

$$E_{u,d}(k_z) = \frac{\hbar^2 k_z^2}{2m_{\text{eff}}} \pm \sqrt{E_x^2 \alpha_{\text{eff}}^2 k_z^2 + \Delta_Z^2}, \quad (7.11)$$

where $\Delta_Z^2 = \mu_B^2 (B_x^2 g_x^2 + B_z^2 g_z^2)$ and the index u (d) marks the upper (lower) energy band. The Fermi wavevector k_F is found from the condition $E_d(k_z) = 0$ and is given by

$$k_F = \pm \sqrt{2\tilde{k}_{so}^2 + \sqrt{4\tilde{k}_{so}^4 + \tilde{k}_Z^4}}, \quad (7.12)$$

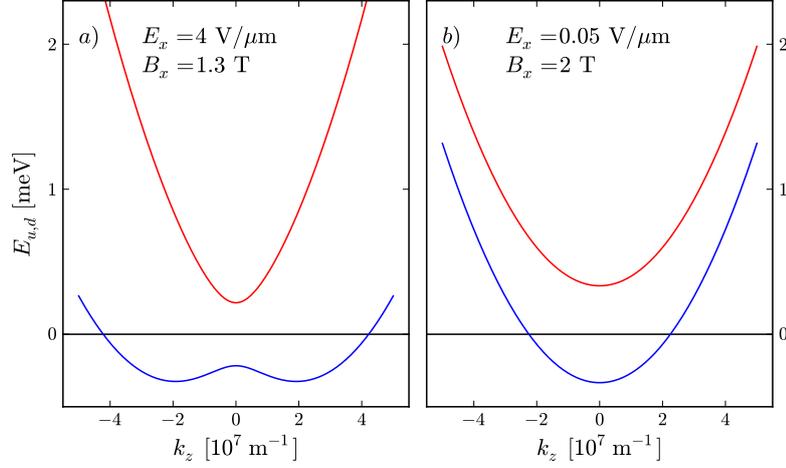


Abbildung 7.2: The lowest-energy spectra $E_u(k_z)$ (red) and $E_d(k_z)$ (blue) as functions of the momentum k_z (a) in the strong SOI regime and (b) in the weak SOI regime. The respective magnitudes of the applied fields are given as insets. The magnetic field \mathbf{B} is chosen along the x axis (like the \mathbf{E} field). The used NW parameters are $R = 7.5$ nm and $\Delta = 23$ meV.

with components

$$\tilde{k}_{so}^2 = \frac{E_x^2 \alpha_{\text{eff}}^2 - 4C/\Delta [B_z^2 DG + B_x^2 KL_B] \mu_B^2}{\hbar^4/m_{\text{eff}}^2 - 16(C/\Delta)^2 [B_z^2 D^2 + B_x^2 L_B^2] \mu_B^2}, \quad (7.13)$$

$$\tilde{k}_Z^4 = \frac{4 [B_z^2 G^2 + B_x^2 K^2] \mu_B^2}{\hbar^4/m_{\text{eff}}^2 - 16(C/\Delta)^2 [B_z^2 D^2 + B_x^2 L_B^2] \mu_B^2}. \quad (7.14)$$

To obtain this result, we have taken into account the full k_z dependence of the g factors, hence we cannot use the effective parameters g_x and g_z as they themselves depend on k_z [see Eq. (7.10)]. Using the definitions above, we introduce the SOI energy $\tilde{\Delta}_{so} = E_x \alpha_{\text{eff}} \tilde{k}_{so}/2$. This allows us to distinguish between the strong SOI regime ($k_F/\tilde{k}_{so} \approx 2$), where the SOI energy dominates over the Zeeman energy, and the weak SOI regime ($k_F/\tilde{k}_Z \approx 1$), where the Zeeman energy dominates over the SOI energy. In Fig. 7.2, we plot the bands $E_{u,d}(k_z)$ for two sets of finite electric and magnetic fields: one in the strong [Fig. 7.2 (a)] and one in the weak [Fig. 7.2 (b)] SOI regime. We compared numerically the exact spectrum with the approximate one for the configurations considered in Fig. 7.2 and found good agreement.

Superconductivity: pairing Hamiltonian

In this section, we derive an effective Hamiltonian describing the proximity induced superconductivity in the lowest subband g' . The proximity-induced

superconducting pairing gap $\Delta_{sc}^{\text{exp}} \approx 235 \mu\text{eV}$ was observed experimentally in Ge/Si core/shell NWs [124]. Pairing Hamiltonians describing superconductivity for hole states in semiconductors were also discussed before in several theoretical works [89, 250, 251]. Here, we start from a pairing Hamiltonian allowing for coupling between bulk hole states with opposite orbital and angular momentum [89],

$$H_{SC} = \int d^3r \left[\Delta_{3/2} \Psi_{3/2}^\dagger \Psi_{-3/2}^\dagger + \Delta_{1/2} \Psi_{1/2}^\dagger \Psi_{-1/2}^\dagger + \text{H.c.} \right], \quad (7.15)$$

where the fermionic operators Ψ_{m_j} annihilate bulk hole states with angular momentum $j = 3/2$ and $m_j = \pm 3/2, \pm 1/2$ and which are coupled by the respective superconducting pairing potentials $\Delta_{3/2}$ and $\Delta_{1/2}$. We assume that $\Delta_{3/2}$ is real but employ $\Delta_{1/2} = |\Delta_{1/2}|e^{i\varphi_{sc}}$ to account for a possible complex superconducting phase. We use H_{SC} to derive an effective pairing Hamiltonian within the framework of the microscopic model (see Sec. 7.2) by modifying the procedure outlined in Ref. [23]. By extending the basis of the microscopic model given below Eq. (7.2) accordingly, we derive an effective 1D particle-hole basis.¹ Furthermore, we use the explicit three-dimensional wave functions of the hole states in the NW [23] and calculate the matrix elements of the effective 1D superconducting Hamiltonian by integrating out the transverse part. Finally, we transform the resulting Hamiltonian by the SWT introduced in Sec. 7.2 and truncate the lowest-energy particle-hole subspace with Nambu space representation $\Psi_{ph} = (\Psi_{g'_+}, \Psi_{g'_-}, \Psi_{g'_+}^\dagger, \Psi_{g'_-}^\dagger)$. In this representation, the effective lowest-energy subband superconducting pairing Hamiltonian is given by $\tilde{H}_{SC} = \frac{1}{2} \int \Psi_{ph}^\dagger \tilde{\mathcal{H}}_{SC} \Psi_{ph}$ with

$$\tilde{\mathcal{H}}_{SC} = \begin{pmatrix} 0 & 0 & 0 & i\Delta_{sc} \\ 0 & 0 & -i\Delta_{sc} & 0 \\ 0 & i\Delta_{sc}^* & 0 & 0 \\ -i\Delta_{sc}^* & 0 & 0 & 0 \end{pmatrix}, \quad (7.16)$$

where $i\Delta_{sc} = 0.01\Delta_{3/2} - 0.5|\Delta_{1/2}|e^{i\varphi_{sc}}$. We combine $\tilde{\mathcal{H}}_{SC}$ with $\tilde{\mathcal{H}}_{g'}$, where the latter is extended to the particle-hole subspace Ψ_{ph} , and obtain an effective Bogoliubov-de-Gennes Hamiltonian (explicitly given in Appendix F.1). The

¹To avoid confusion between various holes, please note that the hole mentioned here actually denotes the conjugate hole.

spectrum of this Hamiltonian is given by

$$E^2 = \left(\frac{\hbar^2 k_z^2}{2m_{\text{eff}}} \right)^2 + E_x^2 k_z^2 \alpha_{\text{eff}}^2 + \Delta_Z^2 + |\Delta_{sc}|^2 \pm 2 \sqrt{\left(\frac{\hbar^2 k_z^2}{2m_{\text{eff}}} \right)^2 (E_x^2 k_z^2 \alpha_{\text{eff}}^2 + \Delta_Z^2) + |\Delta_{sc}|^2 \Delta_Z^2}. \quad (7.17)$$

At $k_z = 0$, we find that Eq. (7.17) reduces to $E^2 = (|\Delta_{sc}| \pm \Delta_Z)^2$, and the topological gap is given by

$$\Delta_- = |\Delta_{sc}| - \Delta_Z. \quad (7.18)$$

The system is in the non-topological phase for $\Delta_- > 0$ and in the topological phase for $\Delta_- < 0$ [86, 87, 249].

7.3 Tunability of the Majorana fermion localization length

Next, we focus on the MF wave functions and associated localization lengths assuming that the two MFs are well-localized at the ends of a Ge/Si core/shell NW and do not overlap with each other. To obtain independent solutions for the MF wave functions at both ends, we simplify the calculations by assuming a semi-infinite NW originating, let's say, at $z = 0$. For topological computational schemes, one generally strives for small localization lengths and, thus, well localized MFs. We analyze the tunability of the localization lengths as functions of magnitude and direction of the applied fields \mathbf{E} and \mathbf{B} and determine the regime in which the localization lengths are the shortest.

Strong SOI

First, we focus on the strong SOI regime, where $\Delta_{so} \gg \Delta_Z$ with $\Delta_{so} = \alpha_{\text{eff}} E_x k_{so}/2$ and $k_{so} = m_{\text{eff}} \alpha_{\text{eff}} E_x / \hbar^2$. Here, the Fermi wave number is given by $k_F^s = 2k_{so}$, and the associated Fermi velocity is $v_F^s = \alpha_{\text{eff}} E_x / \hbar$. In this regime, the main effect of the applied magnetic field is the opening of a gap at $k_z = 0$, thus we are allowed to drop the k_z dependence of the g factors [see Eqs. (7.10)] and to use the following approximation for the Zeeman splitting $\Delta_Z \approx \Delta_Z^0 e^{i\theta_B^0} = \mu_B (B_x g_{x0} + i B_z g_{z0})$. To derive the MF wave functions [249], we first linearize the spectrum around the Fermi points $k_z = 0$ (interior branch of the spectrum) and $k_z = \pm k_F^s$ (exterior branch of the spectrum) and express the fermionic operators in terms of slowly varying left- and right

movers L_{\pm} and R_{\pm} where the indices \pm label the two pseudospin directions for a quantization axis pointing along the SOI induced by the electric field E_x . As a result, the Hamiltonian splits into two independent parts. The exterior branch is described by

$$\mathcal{H}^e = i\hbar v_F^s \eta_0 \nu_z \partial_z + \frac{1}{2} [i\Delta_{sc}(\eta_x + i\eta_y)\nu_y + \text{H.c.}], \quad (7.19)$$

which is written in the basis $(L_+, R_-, L_+^\dagger, R_-^\dagger)$. Here, the Pauli matrices η_i (ν_i), $i = 0, x, y, z$, act in particle-hole (left- and right-mover) subspace. The interior branch is described by

$$\begin{aligned} \mathcal{H}^i = & -i\hbar v_F^s \eta_0 \nu_z \partial_z + \frac{1}{2} [i\Delta_{sc}(\eta_x + i\eta_y)\nu_y + \text{H.c.}] \\ & - \Delta_Z^0 (\cos \vartheta_B^0 \eta_0 \nu_y + \sin \vartheta_B^0 \eta_z \nu_x), \end{aligned} \quad (7.20)$$

which is given in the basis $(R_+, L_-, R_+^\dagger, L_-^\dagger)$. As shown before, a localized zero energy state, MF, exists in the topological phase $\Delta_Z^0 > |\Delta_{sc}|$. The associated MF wave function is a sum of two contributions [249], $\hat{\Phi}_s(z) = \hat{\Phi}_s^e(z) + \hat{\Phi}_s^i(z)$, originating from the exterior and interior branches (for an explicit expression see App. F.2), which are of the form

$$\hat{\Phi}_s^e(z) \propto e^{-z/\xi_s^e}, \quad \hat{\Phi}_s^i(z) \propto e^{-z/\xi_s^i}, \quad (7.21)$$

with the localization lengths given by

$$\xi_s^e = \frac{\alpha_{\text{eff}} |E_x|}{|\Delta_{sc}|}, \quad \xi_s^i = \frac{\alpha_{\text{eff}} |E_x|}{|\Delta_-|}. \quad (7.22)$$

Both ξ_s^e and ξ_s^i depend linearly on the magnitude of the applied electric field E_x , thus weaker fields result in smaller localization lengths. Furthermore, ξ_s^i shows an implicit dependence on the magnitude and direction of \mathbf{B} in the denominator via $\Delta_- = |\Delta_{sc}| - \Delta_Z^0$. The localization length diverges when Δ_Z^0 approaches $|\Delta_{sc}|$, which happens when the topological gap closes and the system becomes gapless. In Fig. 7.3, we plot ξ_s^e and ξ_s^i as functions of the angle θ enclosed by \mathbf{B} and the x axis (see Fig. 7.1). We see that as soon as \mathbf{B} has a non-zero component parallel to the NW, ξ_s^i increases until it diverges at the point where the topological gap closes and the system goes into the topologically trivial phase. This effect roots in the strong anisotropy of the g factor in Δ_Z^0 which leads to a quick closing of the topological gap as soon as θ deviates from zero. Furthermore, increasing the magnitude of \mathbf{B} while still being in the strong SOI regime, such that $|\Delta_-| > |\Delta_{sc}|$, i.e., $\Delta_Z^0 \geq 2|\Delta_{sc}|$, results in $\xi_s^i < \xi_s^e$ for a certain range of θ . Thus, in this regime, the localization length of the MF wave functions, $\xi = \max\{\xi_s^i, \xi_s^e\}$, is independent of the magnetic field.

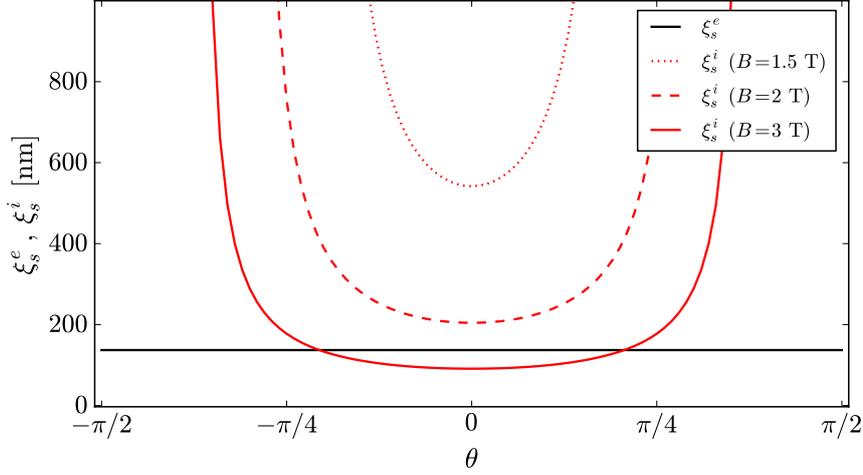


Abbildung 7.3: Localization lengths ξ_s^e and ξ_s^i as functions of the angle θ defined by $\mathbf{B} = B(\cos \theta, 0, \sin \theta)$, for $E_x = 4 \text{ V}/\mu\text{m}$ and for different magnitudes of B . As soon as θ deviates from 0, ξ_s^i increases until its value diverges when the topological gap closes. Furthermore, increasing B above a threshold value given by $|\Delta_-| = |\Delta_{sc}|$, i.e., $\Delta_Z^0 \geq 2|\Delta_{sc}|$, results in $\xi_s^i < \xi_s^e$ for a certain range of θ . Since ξ_s^e is independent of \mathbf{B} , its value appears as a constant in the plot. We use the NW parameters $R = 7.5 \text{ nm}$ and $\Delta = 23 \text{ meV}$ and assume a superconductivity pairing potential of $\Delta_{sc} = 200 \mu\text{eV}$.

Weak SOI

Next, we focus on the weak SOI regime in which $\Delta_{so} \ll \Delta_Z$. We find that $\Delta_Z \sim \Delta_Z^0$ is still a good approximation for magnetic fields up to $B \sim 5\text{T}$. This allows us to simplify Eq. (7.12). As a result, the Fermi wave number is given by $k_F^w \approx \sqrt{2m_{\text{eff}}\Delta_Z^0/\hbar}$, and the associated Fermi velocity reads $v_F^w = \sqrt{2\Delta_Z^0/m_{\text{eff}}}$. By treating the SOI as a weak perturbation, we find the eigenstates of the particle Hamiltonian around the Fermi points k_F^w and linearize the particle-hole Hamiltonian in the basis constructed of these states. We find

$$\mathcal{H}^{(e)} = -i\hbar v_F^w \eta_0 \nu_z \partial_z + \frac{1}{2} \left[\bar{\Delta}_{sc}^* i e^{-i\vartheta_B^0} (\eta_x + i\eta_y) \nu_y + \text{H.c.} \right], \quad (7.23)$$

which is represented in the basis $(R, L, R^\dagger, L^\dagger)$, with $R(L)$ being the right-mover (left-mover) in the weak SOI regime. As already found in Ref. [249], the effective coupling due to superconductivity is suppressed by a factor $k_{so}/k_F^w \ll 1$, resulting in an effective superconducting coupling term $|\bar{\Delta}_{sc}| = 2|\Delta_{sc}|k_{so}/k_F^w$. This can be understood from the fact that without the SOI, the pseudospins of the states at the Fermi points are perfectly aligned and only the weakly perturbing SOI term tilts them into a slightly non-parallel configuration that enables a superconducting pairing. The localized MF wave function is again a sum of two contributions, $\hat{\Phi}_w(z) = \hat{\Phi}_w^{(e)}(z) + \hat{\Phi}_w^{(i)}(z)$ (for

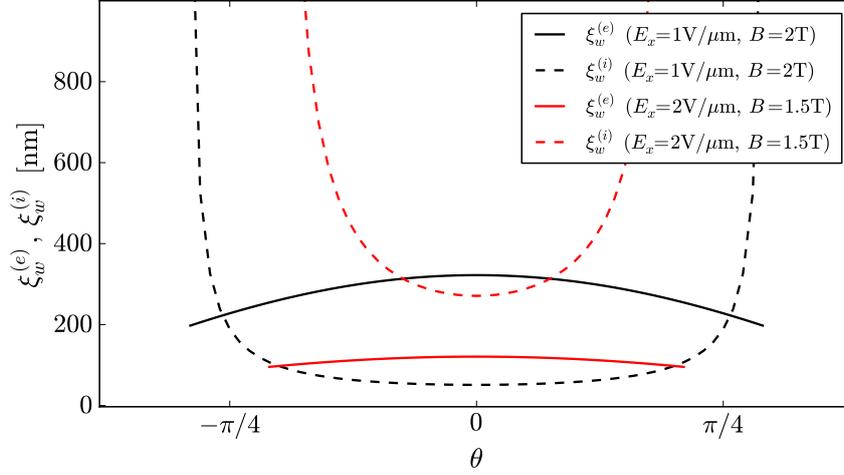


Abbildung 7.4: Localization lengths $\xi_w^{(e)}$ and $\xi_w^{(i)}$ as functions of the angle θ defined by $\mathbf{B} = B(\cos \theta, 0, \sin \theta)$, for different magnitudes of E_x and B . Here we use the combinations $E_x = 1 \text{ V}/\mu\text{m}$ and $B = 2 \text{ T}$ (blue), $E_x = 2 \text{ V}/\mu\text{m}$ and $B = 1.5 \text{ T}$ (red). As soon as θ deviates from 0, $\xi_w^{(i)}$ increases until its value diverges when the topological gap closes. In contrast to ξ_s^e (see Fig. 7.3), $\xi_w^{(e)}$ now shows a dependence on θ . Here, we use the same values for the NW parameters and superconducting pairing parameter as in Fig. 7.3.

an explicit expression see App. F.2), which are of the form

$$\hat{\Phi}_w^{(e)}(z) \propto e^{-z/\xi_w^{(e)}}, \quad \hat{\Phi}_w^{(i)}(z) \propto e^{-z/\xi_w^{(i)}}, \quad (7.24)$$

with localization lengths given by

$$\begin{aligned} \xi_w^{(e)} &= \sqrt{\frac{2\Delta_Z^0}{m_{\text{eff}}|\Delta_{sc}|}} \frac{\hbar}{|\Delta_{sc}|} = \frac{\Delta_Z^0}{|\Delta_{sc}|} \frac{\hbar^2}{m_{\text{eff}}\alpha_{\text{eff}}|E_x|}, \\ \xi_w^{(i)} &= \frac{\alpha_{\text{eff}}|E_x|}{|\Delta_-|}. \end{aligned} \quad (7.25)$$

We see that the localization lengths depend quite differently on the strength of the SOI determined by E_x , $\xi_w^{(e)} \propto 1/|E_x|$ and $\xi_w^{(i)} \propto |E_x|$. Furthermore, in contrast to the strong SOI regime, both localization lengths depend on the magnitude and direction of \mathbf{B} . In Fig. 7.4, we plot $\xi_w^{(e)}$ and $\xi_w^{(i)}$ as functions of the angle θ enclosed by \mathbf{B} and the x axis, for various combinations of E_x and B . We observe that the dependence of $\xi_w^{(e)}$ on θ is much weaker than the θ dependence of $\xi_w^{(i)}$, e.g., $\xi_w^{(e)}$ does not diverge when the topological gap closes. Furthermore, depending on the relative magnitude of the fields, we can find both, $\xi_w^{(e)} > \xi_w^{(i)}$ and $\xi_w^{(e)} < \xi_w^{(i)}$.

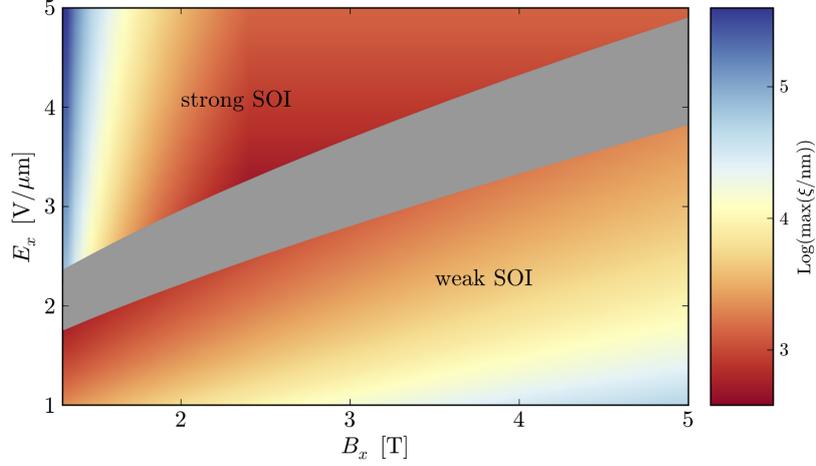


Abbildung 7.5: Logarithm (color coded) of the dominating localization length, $\xi = \max\{\xi_s^e, \xi_s^i\}$ and $\xi_w^{(e)}$, in the strong and weak SOI regime, respectively, as functions of the applied fields E_x and \mathbf{B} . For simplicity we restrict ourselves to $\mathbf{B} = (B_x, 0, 0)$. The diagonal gray area approximately denotes the transitional regime between regions of strong and weak SOI. Here, we use the same values for the NW parameters and superconducting pairing parameter as in Fig. 7.3.

Optimal experimental regime

As shown above, the magnitude and direction of the applied fields determine the localization lengths of the MF wave functions, see Figs. 7.3 and 7.4. In experiments, it is crucial to tune the applied fields such that obtained MFs are well separated and the localization lengths are as short as possible. To identify the optimal field regime, we display the logarithm of the maximal localization length for the given magnitudes of the applied fields in Fig. 7.5. In the weak SOI regime, we furthermore have to take into account that the part of the wave function decaying with the localization length $\xi_s^{(i)}$ is additionally suppressed by a factor $k_{so}/k_F^w \ll 1$ and thus can be neglected. To simplify the analysis, we fix the direction of the magnetic field to be perpendicular to the NW, $\mathbf{B} = (B_x, 0, 0)$. Here, we are motivated by the fact that this configuration corresponds to the shortest localization lengths in the strong SOI regime. The range of B_x is chosen such that we remain in the topological regime throughout. We see that when applying large E_x while keeping B_x small or when applying large B_x while keeping E_x small, the localization lengths are not the shortest possible. Hence it is most favorable to choose an intermediate regime in which both fields take rather moderate values and the Zeeman energy and the SOI energy are comparable with each other.

7.4 Finite nanowires: hybridized Majorana fermions

So far we have focused on a semi-infinite NW that, when being brought into the topological phase, hosts a zero-energy MF at the end. However, in any realistic system, the NWs are of finite length L and host two MFs: one MF at each end. These MFs could overlap and hybridize if their localization lengths are comparable with the NW length. This results in the emergence of an ordinary fermion which, in general, possesses a non-zero energy [245, 246]. In this section, we examine the dependence of this fermionic energy on the magnitude of the applied fields in the strong and weak SOI regime. We assume that the NW stretches from $z = 0$ to $z = L$ and search for hybridized wave functions that satisfy vanishing boundary conditions at both ends of the NW. We note that we focus here on the direct overlap between two MF wave functions and neglect a possible hybridization mediated by bulk superconducting states [252].

Strong SOI

In this section, we explore the energy of hybridized MFs in the strong SOI regime. First, we solve the Schrödinger equations $\mathcal{H}^e \phi^e = E_n^s \phi^e$ and $\mathcal{H}^i \phi^i = E_n^s \phi^i$ for arbitrary $E_n^s > 0$ (for the Hamiltonian densities see Sec. 7.3). Since the NW is of finite length, both the decaying and growing eigenfunctions are normalizable and may contribute to the final hybridized wave function. We obtain a set of eight eigenfunctions ϕ_j^e and ϕ_j^i , $j = 1, \dots, 4$, where the ϕ_j^e show an oscillatory behavior proportional to $e^{\pm ik_F^s z}$. We search for a non-trivial linear combination of these eigenfunctions, $\Phi_{\text{hyb}}^s(z) = \sum_j (a_j^e \phi_j^e + a_j^i \phi_j^i)$, that satisfies the boundary conditions $\Phi_{\text{hyb}}^s(z = 0) = \Phi_{\text{hyb}}^s(z = L) = 0$. In the considered regime, E_n^s is given by a quite involved implicit equation which we omit displaying here.

We provide numerical results for several specific sets of applied fields and plot E_n^s as a function of E_x in Fig. 7.6. For all field configurations, we observe an oscillatory behavior of E_n^s with increasing amplitude as E_x increases. In addition, depending on the magnitude of the applied magnetic field, the curves may show a non-zero offset that increases with E_x . This feature is the most pronounced for small magnetic fields close to the point where the topological gap closes.

These results can be explained easily when remembering the zero energy

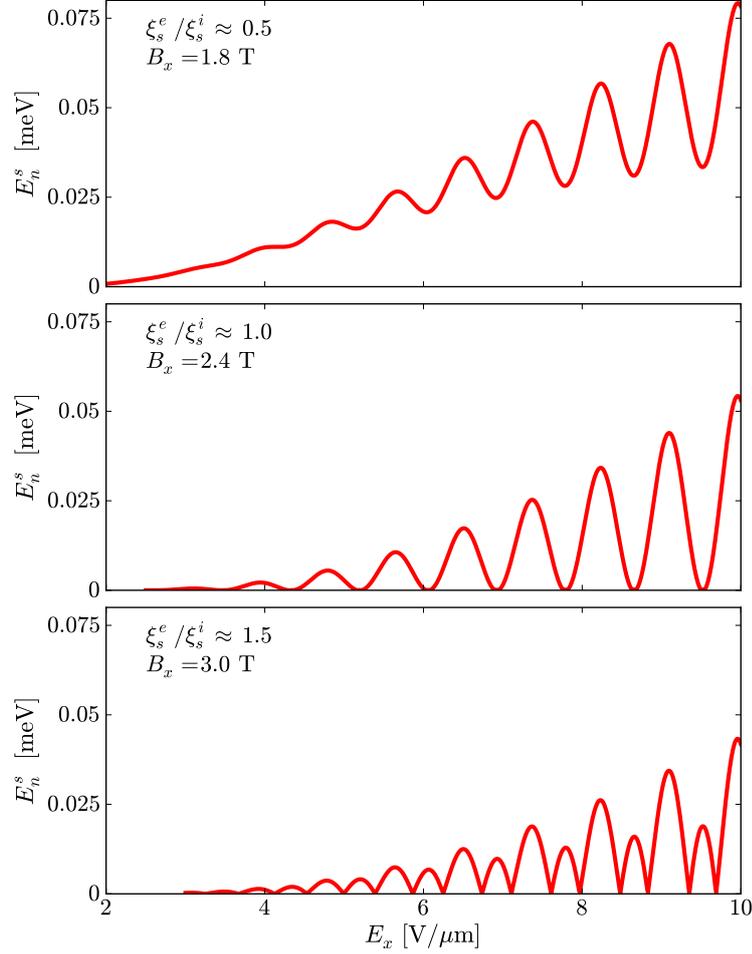


Abbildung 7.6: The fermion energy E_n^s in the strong SOI regime as a function of the electric field E_x for different magnitudes of the applied magnetic field $\mathbf{B} = (B_x, 0, 0)$, see the insets. We consider three different ratios of the localization lengths ξ_s^e/ξ_s^i . If the contribution of the interior branches is dominant, $\xi_s^i > \xi_s^e$, E_n^s shows an increasing offset from zero with weak superimposed oscillations on top of it. If the contribution of the exterior branches is dominant, $\xi_s^e > \xi_s^i$, E_n^s shows an increasing offset from zero with strong superimposed oscillations on the top of it such that E_n^s periodically returns to zero. Here, we assume a superconducting pairing potential $\Delta_{sc} = 200 \mu\text{eV}$ and use the NW parameters $R = 7.5 \text{ nm}$, $\Delta = 23 \text{ meV}$ and $L = 0.7 \mu\text{m}$.

MF wave function which is a linear combination of oscillating (exterior branch, ξ_s^e) and non-oscillating (interior branch, ξ_s^i) wave functions (see Sec. 7.3). This result remains valid for very small energies E_n^s , thus the lengthscales governing the growth and decay of the eigenstates $\phi_j^{e,i}$ are comparable to ξ_s^e and ξ_s^i . If the localization length is set by the non-oscillating interior branch part, $\xi_s^e/\xi_s^i \ll 1$

(see the insets in Fig. 7.6), E_n^s monotonically splits away from zero with superimposed weak oscillations. On the contrary, if the localization length is set by the strongly oscillating exterior branch part, $\xi_s^e/\xi_s^i \geq 1$, E_n^s oscillates strongly and even goes back to zero. Thus, depending on the ratio of the localization lengths ξ_s^e and ξ_s^i which can be tuned by changing the magnitude or the direction of the applied magnetic field with respect to the NW (see Fig. 7.3), the offset of E_n^s can be tuned. The period of the superimposed oscillations is independent of the magnitude of B_x since the ϕ_j^e cause oscillations with a period $\delta E_x = \hbar^2\pi/(m_{\text{eff}}\alpha_{\text{eff}}L)$. Using the latter relation, the strength of the SOI can be determined from the oscillation period.

Weak SOI

In the weak SOI regime, we apply the same procedure as described in Sec. 7.4. Here, we employ the Hamiltonian $\mathcal{H}^{(e)}$ given in Eq. (7.23) and solve the Schrödinger equation $\mathcal{H}^{(e)}\phi^{(e)} = E_n^w\phi^{(e)}$ for an arbitrary $E_n^w > 0$. The four eigenstates $\phi_j^{(e)}$, $j = 1, \dots, 4$, are combined into a non-trivial linear combination, $\Phi_{\text{hyb}}^w(z) = \sum_j b_j^{(e)}\phi_j^{(e)}$, that satisfies the boundary conditions $\Phi_{\text{hyb}}^w(z=0) = \Phi_{\text{hyb}}^w(z=L) = 0$. This leads to an implicit condition for E_n^w ,

$$\left[\frac{\sqrt{\bar{\Delta}_{sc}^2 - E_n^w}}{\bar{\Delta}_{sc}} \right]^2 = \frac{2 \sinh^2 \left[\frac{L\sqrt{\bar{\Delta}_{sc}^2 - E_n^w}}{v_F^w \hbar} \right]}{\cosh \left[\frac{2L\sqrt{\bar{\Delta}_{sc}^2 - E_n^w}}{v_F^w \hbar} \right] - \cos(2k_F^w L)}. \quad (7.26)$$

This implicit equation can be transformed to an explicit relation for E_n^w by assuming that $E_n^w \ll \bar{\Delta}_{sc}$,

$$E_n^w \approx \bar{\Delta}_{sc} |\sin(k_F^w L)| e^{-L/\xi_w^{(e)}}, \quad (7.27)$$

which shows an oscillatory behavior of E_n^w as a function of k_F^w , where the latter is a function of \mathbf{B} . In Fig. 7.7, we plot E_n^w as a function of $\mathbf{B} = (B_x, 0, 0)$ for a weak electric field E_x where we obtained E_n^w once by solving Eq. (7.26) numerically and once by using the explicit relation given in Eq. (7.27). Both results agree well, especially for small B_x . We see that E_n^w oscillates and the energy of the fermion composed of two overlapping MFs periodically comes back to zero [245, 246]. The periodicity of the oscillation is given by

$$\delta\Delta_Z^0 \approx \frac{\pi\hbar}{L} \sqrt{\frac{2\Delta_Z^0}{m_{\text{eff}}}}, \quad (7.28)$$

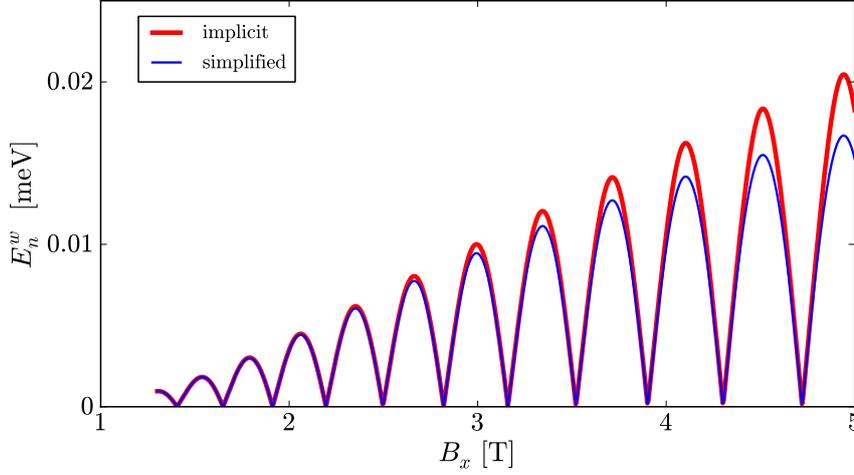


Abbildung 7.7: The oscillating energy E_n^w as a function of $\mathbf{B} = (B_x, 0, 0)$. We display both the results from solving the implicit Eq. (7.26) numerically (red) and the simplified solution given in Eq. (7.27) (blue) and find good agreement. We assume a weak electric field $E_x = 0.5 \text{ V}/\mu\text{m}$ and a proximity induced superconducting pairing potential $\Delta_{sc} = 200 \mu\text{eV}$. We use the NW parameters $R = 7.5 \text{ nm}$, $\Delta = 23 \text{ meV}$ and $L = 2 \mu\text{m}$.

and depends on the g factor and hence on the direction of the magnetic field. As a result, the change in the period as a function of the magnetic field direction could be used to measure the g factor anisotropy.

Changing the strength of the applied electric field E_x does not affect the period of the oscillation, however, examining Eq. (7.27) in more detail shows that a stronger field E_x yields a smaller amplitude of the splitting.

7.5 Conclusion

In this chapter, we utilized a concrete microscopic model to study MFs confined to Ge/Si core/shell NWs. To this end, we derived an effective 1D lowest subband hole Hamiltonian, which also includes the superconducting pairing and takes into account specifics of Ge/Si core/shell NWs such as the g factor anisotropy and the electric field dependence of the induced Rashba SOI. We have determined the MF localization lengths in the strong and in the weak SOI regime and examined their dependence on the direction of the magnetic field with respect to the NW. In general, we found that intermediate magnitudes of electric and magnetic fields lead to the shortest localization lengths of the MF wave functions. Additionally, we examined finite NWs, where two MFs localized at the NW ends overlap and form an ordinary fermion. This hybridization results in a fermion whose energy oscillates as a function of the

electric field (magnetic field) in the strong (weak) SOI regime. The possibility to control the overlap of MFs by tuning only electric fields could be used to perform topologically non-protected operations on Majorana fermion that are necessary to realize universal quantum computation [206].

From our results we conclude that Ge/Si core/shell NWs are a promising system regarding the emergence of MFs due to the high control over the SOI strength. In addition, we note that these NWs are also excellent candidates for parafermion setups which require even stronger SOI and substantial electron-electron interactions [253–255]. In addition, the lowest energy subband Hamiltonian derived in this chapter can provide the basis for further investigation of arrays of Ge/Si NWs. Such arrays could also be used to study quantum Hall effect [256–260], topological superconductor [261, 262], and quantum spin Hall effect [263] in the anisotropic limit.

Acknowledgments

We thank Christoph Kloeffel for helpful discussions. We acknowledge support from the Swiss NSF, NCCR QSIT, through the EC FP7-ICT initiative under project SiSPIN No 323841, and the Harvard Quantum Optical Center.

Appendix

Supplementary information for Chapter 2: 'Effect of strain on hyperfine-induced hole-spin decoherence in quantum dots'

A.1 Hamiltonian - Explicit form

In Chapter 2, we use the 8×8 Kane Hamiltonian as given in Ref. [6], Appendix C, and a harmonic confinement potential. For completeness, we display here the general structure and relevant parts. The Kane Hamiltonian is given by

$$H_K = \begin{pmatrix} K_{11} & K_1 & K_2 & K_3 \\ K_1^\dagger & K_{22} & K_4 & K_5 \\ K_2^\dagger & K_4^\dagger & K_{33} & K_6 \\ K_3^\dagger & K_5^\dagger & K_6^\dagger & K_{44} \end{pmatrix}, \quad (\text{A.1})$$

of which the blocks

$$\begin{aligned} K_{22} &= \begin{pmatrix} A & 0 \\ 0 & A \end{pmatrix}, & K_4 &= \sqrt{3} \begin{pmatrix} 2C & D \\ D^* & -2C^* \end{pmatrix}, \\ K_1^\dagger &= \begin{pmatrix} -B & 0 \\ 0 & B^* \end{pmatrix}, & K_5 &= \sqrt{6} \begin{pmatrix} -C & -D \\ D^* & -C^* \end{pmatrix}, \end{aligned} \quad (\text{A.2})$$

are relevant for the calculations. The single entries are denoted by $A = -\hbar^2/(2m_0)[(\gamma_1 + \gamma_2)(k_x^2 + k_y^2) + (\gamma_1 - 2\gamma_2)k_z^2]$, $B = 1/\sqrt{2}P(k_x - ik_y)$, $C = \hbar^2/(2m_0)\gamma_3k_z(k_x - ik_y)$, and $D = \hbar^2/(2m_0)[\gamma_2(k_x^2 - k_y^2) - 2i\gamma_3k_xk_y]$, with \hbar being Planck's constant, m_0 being the bare electron mass and γ_i , $i = 1, 2, 3$, denoting the Luttinger parameters. In H_K , terms proportional to C_k , B_{7v} and B_{8v}^\pm were omitted due to their smallness [64, 104]. The harmonic confinement potential

$$V_{\text{conf},j}(\mathbf{r}) = \left(\frac{m_{j,\perp}\omega_{j,\perp}^2}{2}z^2 + \frac{m_{j,\parallel}\omega_{j,\parallel}^2}{2}(x^2 + y^2) \right) \mathbf{1}_{2 \times 2} \quad (\text{A.3})$$

is defined by the confinement lengths L and a via $\omega_{j,\perp} = \hbar/(m_{j,\perp}a^2)$ and $\omega_{j,\parallel} = \hbar/(m_{j,\parallel}L^2)$. The effective masses in the single bands are given by $m_{\text{CB},\perp/\parallel} = m'$, $m_{\text{HH/LH},\perp} = m_0/(\gamma_1 \mp 2\gamma_2)$, $m_{\text{HH/LH},\parallel} = m_0/(\gamma_1 \pm \gamma_2)$ and $m_{\text{SO},\perp/\parallel} = m_0/\gamma_1$. $\mathbb{1}_{2\times 2}$ denotes the 2×2 unit matrix. Table 2.1 in the main text lists the material parameters of InAs we use in the calculations as input for the 8×8 Hamiltonian $H_{\text{K}} + V_{\text{conf}} + H_{\epsilon}$.

A.2 Continuum limit of the memory kernel

For the second and fourth order in a homonuclear system rotating with ω_n we find [113]

$$\Sigma^{(2)}(s + i\omega_n) \simeq -\frac{c_+ + c_-}{4\omega_n} \sum_k |A_k^\pm|^2, \quad (\text{A.4})$$

$$\Sigma^{(4)}(s + i\omega_n) \simeq -i \frac{c_+ c_-}{4\omega_n^2} \sum_{k_1, k_2} \frac{|A_{k_1}^\pm|^2 |A_{k_2}^\pm|^2}{s + i(A_{k_1}^z - A_{k_2}^z)} \quad (\text{A.5})$$

where we dropped the strain dependence of $A_k^{\pm,z} = A_k^{\pm,z}(\epsilon)$ for readability. In both equations, $c_\pm = I(I+1) - \langle\langle m(m \pm 1) \rangle\rangle$, where I is the nuclear spin, $m = -I, \dots, I$ and the brackets $\langle\langle \dots \rangle\rangle$ indicate averaging over all eigenvalues m of I_k^z . By taking the continuum limit $v_0 \sum_k = \int d^3r$ we replace the sums by integrals. The strain-dependent frequency shift $\Delta\omega = -\text{Re}[\Sigma^{(2)}(s + i\omega_n)] \sim 10^{-18} \text{eV}^2/\omega_n$ can be evaluated for Eqs. (2.7) and (2.8) in a straightforward fashion. A recalculation of the result of Ref. [104] gives exact shape of $1/T_2$ after some transformations of its original form. Starting from

$$\Sigma^{(4)}(s + i\omega_n) \simeq -i \frac{c_+ c_-}{4\omega_n^2} \sum_{k_1, k_2} \frac{|A_{k_1}^\pm|^2 |A_{k_2}^\pm|^2}{s + i(A_{k_1}^z - A_{k_2}^z)}, \quad (\text{A.6})$$

we first simplify by inserting the z averaged coupling, justified by $L \gg a$ and then performing the two-dimensional continuum limit. In the resulting two-dimensional equation we shift to polar coordinates $x_j = r_j \cos \varphi_j$ and $y_j = r_j \sin \varphi_j$. After the angular integration we rescale the radial variables by replacing $r_j = r_{jj}L$. In the resulting integral we substitute $e^{-r_{11}^2} = x$, $r_{11}^4 = (\ln x)^2$, $e^{-r_{22}^2} = y$ and $r_{22}^4 = (\ln y)^2$ and take only the leading term:

$$\begin{aligned} \Sigma^{(4)}(s + i\omega_n) \simeq & -i \frac{c_+ c_- |A_\pm|^4}{4\omega_n^2 A_z} \int_0^1 \int_0^1 dx dy \\ & \times \frac{(\ln x)^2 (\ln y)^2 xy}{s/A_z + i(x - y)}, \end{aligned} \quad (\text{A.7})$$

where $A_z = A_z(\epsilon)$ and A_\pm denotes the sum of all $A_{\pm,j,j'}(\epsilon)$ contributing to the leading term. To calculate the decoherence rate, we have to take into account that $1/T_2 = -\text{Im}[\Sigma(i\omega_n + i\Delta\omega - 0^+)]$ and hence consider

$$\begin{aligned} \Sigma^{(4)}(i\omega_n + i\Delta\omega - 0^+) &\simeq -i \frac{c_+c_-|A_\pm|^4}{4\omega_n^2 A_z} \int_0^1 \int_0^1 dx dy \\ &\times \frac{(\ln x)^2 (\ln y)^2 xy}{(i\Delta\omega - 0^+)/A_z + i(x-y)}. \end{aligned} \quad (\text{A.8})$$

Since we are only interested in the imaginary part of the equation, we use the relation

$$\lim_{\chi \rightarrow 0} \frac{1}{\zeta \pm i\chi} = \mathcal{P} \frac{1}{\zeta} \mp i\pi\delta(\zeta), \quad (\text{A.9})$$

where χ, ζ are real numbers and \mathcal{P} indicates that in any following integration of the above expression the principle value of the integral has to be taken. We find

$$\begin{aligned} \text{Im}[\Sigma^{(4)}(i\omega_n + i\Delta\omega - 0^+)] &\simeq -\frac{c_+c_-|A_\pm|^4}{4\omega_n^2 A_z} \int_0^1 \int_0^1 dx dy (\ln x)^2 x \\ &\times (\ln y)^2 y (-\pi)\delta(x-y + \Delta\omega/A_z), \end{aligned} \quad (\text{A.10})$$

from which follows

$$\frac{1}{T_2} = -\text{Im}[\Sigma^{(4)}(i\omega_n + i\Delta\omega - 0^+)] \quad (\text{A.11})$$

$$\begin{aligned} &= \pi \frac{c_+c_-}{4\omega_n^2} \frac{|A_\pm|^4}{|A_z|} \int_0^1 \int_0^1 dx dy xy \\ &\times (\ln x)^2 (\ln y)^2 \delta(x-y - \Delta\omega/|A_z|) \end{aligned} \quad (\text{A.12})$$

$$\begin{aligned} &= \pi \frac{c_+c_-}{4\omega_n^2} \frac{|A_\pm|^4}{|A_z|} \int_0^1 dx [\ln x]^2 [\ln(x-\eta)]^2 \\ &\times x(x-\eta)\Theta(x-\eta)\Theta(1-x-\eta), \end{aligned} \quad (\text{A.13})$$

where we use $A_z = -|A_z|$ and replace $\eta = \Delta\omega/|A_z|$ in the final step. We arrive at the following expression for the decoherence time

$$\frac{1}{T_2} = \pi \frac{c_+c_-}{4\omega_n^2} \frac{|A_\pm|^4}{|A_z|} \int_\eta^1 dx x [\ln x]^2 (x-\eta) [\ln(x-\eta)]^2, \quad (\text{A.14})$$

which can be evaluated numerically for any $\eta < 1$.

Supplementary information for Chapter 3: 'Tunable g factor and phonon-mediated hole spin relaxation in Ge/Si nanowire quantum dots'

B.1 Effective 1D Hamiltonian

Here we display the effective 1D Hamiltonians used in Eqs. (3.2) and (3.3) of the main text. An extended derivation of these terms can be found in Ref. [23]. We use the basis $\{g_+, g_-, e_+, e_-\}$, where the exact form of the states $g_\pm(x, y)$ and $e_\pm(x, y)$ is given in Ref. [23]. The diagonal elements of the Luttinger-Kohn (LK) Hamiltonian and the strain induced splitting is combined in

$$H_{\text{LKd}} + H_{\text{strain}} = \begin{pmatrix} \frac{\hbar^2 k_z^2}{2m_g} & 0 & 0 & 0 \\ 0 & \frac{\hbar^2 k_z^2}{2m_g} & 0 & 0 \\ 0 & 0 & \frac{\hbar^2 k_z^2}{2m_e} + \Delta & 0 \\ 0 & 0 & 0 & \frac{\hbar^2 k_z^2}{2m_e} + \Delta \end{pmatrix}, \quad (\text{B.1})$$

where $\hbar k_z$ is the momentum operator along the wire and $m_g \simeq m_0/(\gamma_1 + 2\gamma_s)$ and $m_e = m_0/(\gamma_1 + \gamma_s)$ are the effective masses along z . Here, γ_1 and γ_s are the Luttinger parameters in spherical approximation and m_0 denotes the bare electron mass. $\Delta \equiv \Delta_{\text{LK}} + \Delta_{\text{strain}}(\gamma)$ denotes the level splitting between g_\pm and e_\pm , $\gamma \equiv (R_s - R)/R$ is the relative shell thickness, and R (R_s) is the core (shell) radius. $\Delta_{\text{LK}} = 0.73\hbar^2/(m_0 R^2)$ and the strain dependent energy splitting can take values $\Delta_{\text{strain}}(\gamma) \simeq 0 - 30$ meV. The magnetic field $\mathbf{B} =$

$(B_x, 0, B_z) \equiv |\mathbf{B}|(\sin \theta, 0, \cos \theta)$ interacts via the Zeeman coupling

$$H_{B,Z} = \mu_B \begin{pmatrix} B_z G & B_x K & 0 & 0 \\ B_x K & -B_z G & 0 & 0 \\ 0 & 0 & B_z F & B_x M \\ 0 & 0 & B_x M & -B_z F \end{pmatrix}, \quad (\text{B.2})$$

where we set $B_y = 0$ due to cylindrical symmetry. Here, μ_B is the Bohr magneton and the parameters take the numerical values $G = -0.06$, $K = 2.89$, $M = 2.56$ and $F = 1.56$. From the LK Hamiltonian additional off-diagonal coupling terms arise and we find

$$H_{\text{LK}_{\text{od}}} = \begin{pmatrix} 0 & 0 & 0 & -iCk_z \\ 0 & 0 & -iCk_z & 0 \\ 0 & iCk_z & 0 & 0 \\ iCk_z & 0 & 0 & 0 \end{pmatrix}, \quad (\text{B.3})$$

with coupling constant $C = 7.26\hbar^2/(m_0R)$. To describe interactions with the electric field $\mathbf{E} = (E_x, E_y, 0) = |\mathbf{E}|(\cos \varphi_{\text{el}}, \sin \varphi_{\text{el}}, 0)$, we introduce the shorthand notation $\tilde{E} = |\mathbf{E}|e^{i\varphi_{\text{el}}}$. The effective conventional Rashba SOI interaction reads

$$H_{\text{R}} = \alpha \begin{pmatrix} 0 & -i\tilde{E}k_z T & \tilde{E}S & 0 \\ i\tilde{E}^*k_z T & 0 & 0 & -\tilde{E}^*S \\ \tilde{E}^*S & 0 & 0 & -\frac{3}{4}i\tilde{E}^*k_z \\ 0 & -\tilde{E}S & \frac{3}{4}i\tilde{E}k_z & 0 \end{pmatrix} \quad (\text{B.4})$$

with $T = 0.98$ and $S = 0.36/R$ and $\alpha = -0.4 \text{ nm}^2 e$. Although fully taken into account, H_{R} turns out to be negligible for the typical parameters and electric fields considered here (see Eq. (B.6)). The direct, dipolar coupling to \mathbf{E} is given by

$$H_{\text{DR}} = eU \begin{pmatrix} 0 & 0 & \tilde{E} & 0 \\ 0 & 0 & 0 & -\tilde{E}^* \\ \tilde{E}^* & 0 & 0 & 0 \\ 0 & -\tilde{E} & 0 & 0 \end{pmatrix}, \quad (\text{B.5})$$

where the parameter $U = 0.15R$ scales linearly in R . We note that the parameters S and U of H_{R} and H_{DR} are related by

$$\frac{eU}{\alpha S} \simeq -1.1 \frac{R^2}{\text{nm}^2}, \quad (\text{B.6})$$

hence H_{DR} dominates H_{R} by one to two orders of magnitude for radii between $R = 5 - 10 \text{ nm}$. Lastly, the interaction of the magnetic field via the orbital

motion is given by

$$H_{B,\text{orb}} = i\mu_B \begin{pmatrix} 0 & 0 & -B_x L k_z & -B_z D k_z \\ 0 & 0 & B_z D k_z & -B_x L k_z \\ B_x L k_z & -B_z D k_z & 0 & 0 \\ B_z D k_z & B_x L k_z & 0 & 0 \end{pmatrix} \quad (\text{B.7})$$

with $L = 8.04R$ and $D = 2.38R$.

B.2 Effective 1D phonon Hamiltonian

Starting from the spherical Bir-Pikus Hamiltonian (see Eq. (3.7) of the main text), we derive an effective hole phonon coupling Hamiltonian for each phonon mode λ . This is done by integrating out the transverse components of the matrix elements of the states $g_{\pm}(x, y)$ and $e_{\pm}(x, y)$. To improve readability, we introduce an effective phonon annihilation operator $\tilde{b}_{\lambda} = e^{iqz} b_{q,\lambda}(t) = e^{iqz} e^{-i\omega_{\lambda}(q)t} b_{q,\lambda}$.

The transversal phonon mode T couples as

$$H_T = \sum_q a_1 \begin{pmatrix} 0 & 0 & 0 & \tilde{b}_T - \tilde{b}_T^{\dagger} \\ 0 & 0 & -\tilde{b}_T + \tilde{b}_T^{\dagger} & 0 \\ 0 & \tilde{b}_T - \tilde{b}_T^{\dagger} & 0 & 0 \\ -\tilde{b}_T + \tilde{b}_T^{\dagger} & 0 & 0 & 0 \end{pmatrix}, \quad (\text{B.8})$$

and the dilatational mode L gives

$$H_L = \sum_q \begin{pmatrix} a_2(\tilde{b}_L + \tilde{b}_L^{\dagger}) & 0 & 0 & ia_3(\tilde{b}_L - \tilde{b}_L^{\dagger}) \\ 0 & a_2(\tilde{b}_L + \tilde{b}_L^{\dagger}) & ia_3(\tilde{b}_L - \tilde{b}_L^{\dagger}) & 0 \\ 0 & ia_3(\tilde{b}_L - \tilde{b}_L^{\dagger}) & a_4(\tilde{b}_L + \tilde{b}_L^{\dagger}) & 0 \\ ia_3(\tilde{b}_L - \tilde{b}_L^{\dagger}) & 0 & 0 & a_4(\tilde{b}_L + \tilde{b}_L^{\dagger}) \end{pmatrix}. \quad (\text{B.9})$$

For the two flexural modes $F_{\pm 1}$, we find

$$H_{F_{\pm 1}} = \sum_q ia_5 \begin{pmatrix} 0 & 0 & \tilde{b}_{F_{\pm 1}}^{\dagger} & 0 \\ 0 & 0 & 0 & \tilde{b}_{F_{\pm 1}} \\ -\tilde{b}_{F_{\pm 1}} & 0 & 0 & 0 \\ 0 & -\tilde{b}_{F_{\pm 1}}^{\dagger} & 0 & 0 \end{pmatrix} \quad (\text{B.10})$$

and

$$H_{F-1} = \sum_q i a_5 \begin{pmatrix} 0 & 0 & -\tilde{b}_{F-1} & 0 \\ 0 & 0 & 0 & -\tilde{b}_{F-1}^\dagger \\ \tilde{b}_{F-1}^\dagger & 0 & 0 & 0 \\ 0 & \tilde{b}_{F-1} & 0 & 0 \end{pmatrix}. \quad (\text{B.11})$$

Here, the a_i , $i = 1, 2, 3, 4, 5$, are real, q -dependent prefactors. The complete effective hole phonon coupling $H_{\text{h-ph}}$ is then given by

$$H_{\text{h-ph}} = \sum_\lambda H_\lambda = H_\Gamma + H_L + H_{F+1} + H_{F-1}. \quad (\text{B.12})$$

Supplementary information for Chapter 4: 'Nuclear spin diffusion mediated by heavy hole hyperfine non-collinear interactions'

C.1 Effective heavy hole states in a self-assembled quantum dots

In this section, we introduce the 4×4 $\mathbf{k} \cdot \mathbf{p}$ Hamiltonians describing valence band states in zincblende semiconductors confined to strained quantum dots with applied external magnetic field. Furthermore, we calculate the hybridized lowest-energy eigenstates of the heavy-hole subsystem which are subject to light-hole mixing [64, 104, 264].

The Hamiltonians [6] are written in terms of the spin-3/2 matrices J_i , $i = x, y, z$, which are given in a basis of angular momentum eigenstates $|J, M\rangle$. Here, the heavy hole band corresponds to $M = \pm 3/2$ and the light hole band to $M = \pm 1/2$. We choose the basis of the bulk Hamiltonians to be $\{|u_{3/2}\rangle, |u_{1/2}\rangle, |u_{-1/2}\rangle, |u_{-3/2}\rangle\}$, where the $|u_M\rangle$ are products of P -symmetric orbital angular momentum eigenstates ($|P_\pm\rangle, |P_z\rangle$) and spin states ($|\uparrow\rangle, |\downarrow\rangle$) [6]: $|u_{\pm 3/2}\rangle = \mp 1/\sqrt{2} |P_\pm\rangle |\uparrow, \downarrow\rangle$ and $|u_{\pm 1/2}\rangle = 1/\sqrt{6} (|2P_z, P_\pm\rangle |\uparrow\rangle \mp |P_+, 2P_z\rangle |\downarrow\rangle)$.

In the bulk semiconductor, the heavy and light hole states are given by the Luttinger-Kohn Hamiltonian

$$\begin{aligned}
 H_k = & -\frac{\hbar^2}{2m_0} (\gamma_1 k^2 - 2\gamma_2 ((J_x^2 - 1/3 J^2) k_x^2 + \text{c.p.})) \\
 & + \frac{\hbar^2}{2m_0} 4\gamma_3 (\{J_x, J_y\} \{k_x, k_y\} + \text{c.p.}) \\
 & + \frac{2}{\sqrt{3}} C_k (\{J_x, J_y^2 - J_z^2\} k_x + \text{c.p.}),
 \end{aligned} \tag{C.1}$$

where we have defined $\{A, B\} = (AB + BA)/2$, c.p. denotes cyclic permutation, $\hbar k_i = -i\hbar\partial_i$, $i = x, y, z$, is the momentum operator, $k^2 = k_x^2 + k_y^2 + k_z^2$ and $J^2 = J_x^2 + J_y^2 + J_z^2$. The Luttinger parameters are given by γ_l , $l = 1, 2, 3$ and C_k is a consequence of the spin-orbit interaction with higher bands. We denote the diagonal part of H_k by $H_{k,0}$.

We include strain by taking into account

$$H_\varepsilon = D_d \text{Tr}\varepsilon + 2/3 D_u ((J_x^2 - 1/3 J^2)\varepsilon_{xx} + \text{c.p.}) + (C_4(\varepsilon_{yy} - \varepsilon_{zz})J_x k_x + \text{c.p.}), \quad (\text{C.2})$$

where we have only considered diagonal elements of the strain tensor ε , ε_{ii} , $i = x, y, z$. D_d and D_u denote vector potentials and the constant C_4 is defined in Ref. [107]. We refer to the diagonal, k_i -independent part of H_ε as $H_{\varepsilon,0}$.

A magnetic field, $\mathbf{B} = \nabla \times \mathbf{A} = (0, 0, B_z)$, pointing along the growth direction of the quantum dot, is included by adding two more terms to the Hamiltonian [265, 266]. The first term is found by replacing $\mathbf{k} \rightarrow \mathbf{k} + e\mathbf{A}$ in $H_k + H_\varepsilon$ in a semi-classical manner. This yields the implicit magnetic field dependence given by the vector potential \mathbf{A} . We keep only terms linear in \mathbf{A} and define

$$H_{mc} = e\mathbf{A} \cdot \mathbf{v}, \quad (\text{C.3})$$

where $\mathbf{v} = \partial(H_k + H_\varepsilon)/\partial\mathbf{k}$ is the velocity operator. We note that proper operator ordering is still enforced. The second term is the magnetic interaction term

$$H_B = -2\mu_B (\kappa J_z B_z + q J_z^3 B_z), \quad (\text{C.4})$$

where κ is the isotropic and q the anisotropic part of the hole g factor.

We model a flat, cylindric quantum dot by choosing a three-dimensional harmonic confinement potential,

$$V_c = \begin{pmatrix} V_{c,\text{HH}} & 0 & 0 & 0 \\ 0 & V_{c,\text{LH}} & 0 & 0 \\ 0 & 0 & V_{c,\text{LH}} & 0 \\ 0 & 0 & 0 & V_{c,\text{HH}} \end{pmatrix}, \quad (\text{C.5})$$

with

$$V_{c,b}(\mathbf{r}) = -\frac{1}{2}m_{b,\perp}\omega_{b,\perp}^2 z^2 - \frac{1}{2}m_{b,\parallel}\omega_{b,\parallel}^2 (x^2 + y^2), \quad (\text{C.6})$$

where $b = \text{HH, LH}$ detones heavy and light hole. We assume the origin of the coordinate system to be located at the center of the quantum dot. The confinement energies $\omega_{b,\parallel} = \hbar/(m_{b,\parallel}L_b^2)$ and $\omega_{b,\perp} = \hbar/(m_{b,\perp}a_b^2)$ are defined

by the confinement lengths L_b and a_b ($L_b \gg a_b$). The corresponding effective masses in the single bands are given by $m_{\text{HH/LH},\perp} = m_0/(\gamma_1 \mp 2\gamma_2)$ and $m_{\text{HH/LH},\parallel} = m_0/(\gamma_1 \pm \gamma_2)$.

The quantum dot states are then described by

$$H_{\text{qd}} = H_k + H_\varepsilon + H_{mc} + H_B + V_c, \quad (\text{C.7})$$

and the used parameter values can be found in Table C.1. A realistic strain configuration for cylindric InAs quantum dots can be found in Ref. [13]. We divide H_{qd} into a leading order term $H_{\text{qd},0} = H_{k,0} + H_{\varepsilon,0} + V_c$ and a perturbation $H_{\text{qd},1}$, where $H_{k,0}$ and $H_{\varepsilon,0}$ denote the diagonal terms of H_k and H_ε . We directly map the Hamiltonian $H_{k,0} + V_c$ onto a three dimensional anisotropic harmonic oscillator whose eigenenergies E_b in band b are given by

$$E_b = -\hbar\omega_{b,\perp} \left(n_z + \frac{1}{2} \right) - \hbar\omega_{b,\parallel} (n_x + n_y + 1). \quad (\text{C.8})$$

The associated eigenfunctions are the usual three dimensional harmonic oscillator eigenfunctions [see, e.g., Ref. [267]] $\phi_{b,\mathbf{n}_s}(\mathbf{r})$, where $\mathbf{n} = (n_x, n_y, n_z)$ is a vector of the associated quantum numbers. We choose the basis states of $H_{\text{qd},0}$ to be products of type

$$|\Psi_{m_j}^{\mathbf{n}}\rangle = \phi_b^{\mathbf{n}_s}(\mathbf{r}) |u_{m_j}\rangle. \quad (\text{C.9})$$

We are interested in the two lowest-energy states in the heavy hole band, $|\Psi_{3/2}^{\mathbf{n}_{s_0}}\rangle$ and $|\Psi_{-3/2}^{\mathbf{n}_{s_0}}\rangle$ ($\mathbf{n}_0 = (0,0,0)$). We decouple these states from the higher energy states of H_{qd} by a Schrieffer-Wolff transformation [101], $\tilde{H}_{\text{qd}} = e^{-S} H_{\text{qd}} e^S$. We perform the transformation up to second order in $(H_{\text{qd},1})_{ij}/\Delta E \ll 1$, where $(H_{\text{qd},1})_{ij}$ denotes the matrix elements coupling $|\Psi_{3/2}^{\mathbf{n}_{s_0}}\rangle$ and $|\Psi_{-3/2}^{\mathbf{n}_{s_0}}\rangle$ to the higher energy states and ΔE is the energy splitting between the associated subspaces. The approximate lowest energy eigenstates are given by

$$|\tilde{\Psi}_{\pm 3/2}^{\mathbf{n}_{s_0}}\rangle = \mathcal{N}_{\pm 3/2, \mathbf{n}_{s_0}} \sum_{M, \mathbf{n}_s} c_{M, \mathbf{n}_s} |\Psi_M^{\mathbf{n}_s}\rangle, \quad (\text{C.10})$$

where $\mathcal{N}_{\pm 3/2, \mathbf{n}_{s_0}}$ denotes the normalization. The coefficients c_{M, \mathbf{n}_s} depend on quantum dot parameters, such as confinement, strain, dot material, and on the external magnetic field.

C.2 Effective hyperfine interactions of heavy holes

In this section, we calculate the coupling between the effective lowest-energy states $|\tilde{\Psi}_{3/2}^{\mathbf{n}_{s_0}}\rangle$ and $|\tilde{\Psi}_{-3/2}^{\mathbf{n}_{s_0}}\rangle$ via the hyperfine interaction in InAs (GaAs) quantum dots. We follow the procedure outlined in Refs. [64, 104].

	GaAs	InAs		GaAs	InAs
γ_1	6.85	20.40	C_k	[eVÅ] -0.0034	-0.0112
γ_2	2.10	8.30	D_d	[eV] -1.16 [108]	-1.0 [108]
γ_3	2.90	9.10	D_u	[eV] 3.0	2.7
κ	1.1 [268]	7.68 [268]	C_4	[eVÅ] 6.8 [269]	7.0 [269]
q	0.01 [270]	0.04 [147]	a	[Å] 5.65	6.05

Tabelle C.1: List of the used material parameters. All parameters were taken from Ref. [6] if not stated otherwise.

The hyperfine interaction Hamiltonians for an electron located at \mathbf{r} in the field of a nucleus at \mathbf{r}_k consists of three terms, the Fermi contact hyperfine interaction (H_{HF}^c), the anisotropic hyperfine interaction (H_{HF}^a) and the coupling of the orbital angular momentum to the nuclear spin (H_{HF}^L). The three terms read ($\hbar = 1$) [62]

$$H_{\text{HF}}^c = \frac{\mu_0}{4\pi} \frac{8\pi}{3} \gamma_S \gamma_{j_k} \mathbf{S} \cdot \mathbf{I}_k \delta(\mathbf{r}_k), \quad (\text{C.11})$$

$$H_{\text{HF}}^a = \frac{\mu_0}{4\pi} \gamma_S \gamma_{j_k} \frac{3(\mathbf{n}_k \cdot \mathbf{S})(\mathbf{n}_k \cdot \mathbf{I}_k) - \mathbf{S} \cdot \mathbf{I}_k}{r_k^3 (1 + d/r_k)}, \quad (\text{C.12})$$

$$H_{\text{HF}}^L = \frac{\mu_0}{4\pi} \gamma_S \gamma_{j_k} \frac{\mathbf{L}_k \cdot \mathbf{I}_k}{r_k^3 (1 + d/r_k)}. \quad (\text{C.13})$$

Here $\gamma_S = 2\mu_B$ and $\gamma_{j_k} = g_{j_k} \mu_N$ with the Bohr (nuclear) magneton μ_B (μ_N) and g_{j_k} is the nuclear g factor of isotopic species j_k . We have defined the relative coordinate of the electron with respect to the k th nucleus by $\mathbf{r}_k = \mathbf{r} - \mathbf{r}_k$, its relative direction by $\mathbf{n}_k = \mathbf{r}_k / r_k$, and $d \simeq Z \times 1.5 \times 10^{-15}$ m, and Z is the charge of the nucleus. The spin and orbital angular-momentum operators are denoted by \mathbf{S} and $\mathbf{L}_k = \mathbf{r}_k \times \mathbf{p}$.

The Bloch states are written in terms of orbital angular momentum and spin states as introduced in Sec. C.1. We approximate the orbital angular momentum eigenstates as linear combinations of atomic eigenfunctions [110] $u_j(\mathbf{r}) = \alpha \psi_{In,Ga}^{nlm}(\mathbf{r} + \mathbf{d}/2) + \sqrt{1 - \alpha^2} \psi_{As}^{Alm}(\mathbf{r} - \mathbf{d}/2)$. Here, α is the electron distribution between the two atoms and $\psi^{nlm}(\mathbf{r}) = R_{nl}(r) Y_l^m(\vartheta, \varphi)$ are hydrogenic eigenfunctions with quantum numbers n , l , and m . The radial part of the wave function depends on the effective central charge Z_{eff} of the nuclei where we use values for free atoms [111, 112]. The position of the hole with respect to a nuclei located in the Wigner-Seitz cell at $\pm \mathbf{d}/2$ is denoted $\mathbf{r} \pm \mathbf{d}/2$, where $\mathbf{d} = a_{\text{In(Ga)As}}(1, 1, 1)/4$ is the In(Ga)-As bonding vector defined by the respective lattice constant $a_{\text{In(Ga)As}}$. The bonding character of the valence band is expressed by the $+$ sign, and $\int_{\text{WS}} d^3r |u_{m_j}(\mathbf{r})|^2 = 2$ enforces normalizati-

on [63]. Here, the subscript WS indicates that the integral is evaluated over the Wigner-Seitz cell. For the numerical evaluation of the integral we consider a Wigner-Seitz cell as a sphere of radius one half of the As-As atom distance, centered in the middle of the bond connecting In(Ga) with As.

To calculate the hyperfine interaction of different basis states with all nuclear spins, we have to evaluate $\sum_k \langle \Psi_M^{\mathbf{n}s}(\mathbf{r}) | H_{\text{HF}}^c + H_{\text{HF}}^a + H_{\text{HF}}^L | \Psi_{M'}^{\mathbf{n}s'}(\mathbf{r}) \rangle$. We note that the envelopes $\phi_b^{\mathbf{n}s}(\mathbf{r})$ vary slowly across a single Wigner-Seitz cell, whereas the dominant part of the hyperfine interaction is given within a single Wigner-Seitz cell and the long-ranged part of the hyperfine interactions spreading across the boundaries of the Wigner-Seitz cell leads only to minor corrections [64]. Hence we can write the hyperfine interaction as $\sum_k (\phi_b^{\mathbf{n}s}(\mathbf{r}_k))^* \phi_{b'}^{\mathbf{n}s'}(\mathbf{r}_k) \langle u_M^k | H_{\text{HF}}^c + H_{\text{HF}}^a + H_{\text{HF}}^L | u_{M'}^k \rangle_{\text{WS}}$. We numerically evaluate the matrix elements $\langle u_M^k | H_{\text{HF}}^c + H_{\text{HF}}^a + H_{\text{HF}}^L | u_{M'}^k \rangle_{\text{WS}}$ and write them in matrix form using the basis $\{|u_{3/2}^k\rangle, |u_{1/2}^k\rangle, |u_{-1/2}^k\rangle, |u_{-3/2}^k\rangle\}$. By averaging our results over the nuclear abundance ν_i of each atomic species i , we find

$$H_{\text{HF}} \approx A_{\text{hf}}^h \begin{pmatrix} -I_z & -0.52I_- & 0 & 0 \\ -0.52I_+ & -0.46I_z & -0.65I_- & 0 \\ 0 & -0.65I_+ & 0.46I_z & -0.52I_- \\ 0 & 0 & -0.52I_+ & I_z \end{pmatrix} \quad (\text{C.14})$$

where $A_{\text{hf}}^h \sim 1.58 \mu\text{eV}$ ($1.21 \mu\text{eV}$) is the InAs (GaAs) hyperfine coupling constant. Using H_{HF} we can derive an effective hyperfine Hamiltonian for the lowest-energy states $|\tilde{\Psi}_{\pm 3/2}^{\mathbf{n}s_0}\rangle$. We find for an InAs quantum dot subject to $B_z = 5\text{T}$ with $\varepsilon_{xx} = \varepsilon_{yy} = -\varepsilon_{zz} = -0.06$, $L_{\text{LH}} = 1.5L_{\text{HH}}$, and $a_{\text{LH}} = 1.5a_{\text{HH}}$

$$\begin{aligned} H_{\text{HF}}^h &= A_z^h S_z^h I_z + A_{\perp,1}^h S_+^h I_- + A_{\perp,1}^{h*} S_-^h I_+ \\ &\quad + A_{\perp,2}^h S_+^h I_+ + A_{\perp,2}^{h*} S_-^h I_- + A_{\text{nc}}^h S_z^h I_+ \\ &\quad + A_{\text{nc}}^{h*} S_z^h I_- + A_{\text{nc}s}^h S_+ I_z + A_{\text{nc}s}^{h*} S_- I_z, \end{aligned} \quad (\text{C.15})$$

with $A_z^h \simeq -7.89 \cdot 10^{-7} \text{eV}$, $A_{\perp,1}^h \simeq -4.13 \cdot 10^{-10} i$, $A_{\perp,2}^h \simeq -6.38 \cdot 10^{-10}$, $A_{\text{nc}s}^h \simeq -5.03 \cdot 10^{-10} (1 + i)$, and $A_{\text{nc}}^h \simeq -1.58 \cdot 10^{-9} (1 - i)$.

C.3 Effective Hamiltonian for optical nuclear spin pumping via bright excitons

The Hamiltonian describing the dynamics of the system is given by

$$H(t) = H_0 + H_L(t) + H_Z^{\text{nuc}} + H_{\text{HF}}^e + H_{\text{HF}}^h. \quad (\text{C.16})$$

The Hamiltonian H_0 describes the free evolution of the exciton states, $H_L(t)$ is the time-dependent laser Hamiltonian, H_Z^{nuc} describes the nuclear Zeeman interaction, and H_{HF}^e and H_{HF}^h are the hyperfine Hamiltonians for electrons and holes. We have

$$H_0 = E_{\downarrow\uparrow} |\downarrow\uparrow\rangle \langle\downarrow\uparrow| + E_{\uparrow\downarrow} |\uparrow\downarrow\rangle \langle\uparrow\downarrow| + E_{\uparrow\uparrow} |\uparrow\uparrow\rangle \langle\uparrow\uparrow| + E_{\downarrow\downarrow} |\downarrow\downarrow\rangle \langle\downarrow\downarrow|, \quad (\text{C.17})$$

where

$$\begin{aligned} E_{\downarrow\uparrow} &= E_X + \gamma_2 B^2 + \frac{\delta_0}{2} + \frac{1}{2} \sqrt{\delta_1^2 + (g_e - 3g_h)^2 \mu_B^2 B^2} \\ E_{\uparrow\downarrow} &= E_X + \gamma_2 B^2 + \frac{\delta_0}{2} - \frac{1}{2} \sqrt{\delta_1^2 + (g_e - 3g_h)^2 \mu_B^2 B^2} \\ E_{\uparrow\uparrow} &= E_X + \gamma_2 B^2 - \frac{\delta_0}{2} + \frac{1}{2} \sqrt{\delta_2^2 + (g_e + 3g_h)^2 \mu_B^2 B^2} \\ E_{\downarrow\downarrow} &= E_X + \gamma_2 B^2 - \frac{\delta_0}{2} - \frac{1}{2} \sqrt{\delta_2^2 + (g_e + 3g_h)^2 \mu_B^2 B^2}. \end{aligned} \quad (\text{C.18})$$

Here, E_X is the energy required to excite an exciton (band-gap energy), $\gamma_2 B_z^2$ is the diamagnetic shift [271], with γ_2 the diamagnetic constant and B the z -component of the external magnetic field, μ_B is the Bohr magneton, and g_e (g_h) is the electron (hole) Landé g factor. The fine structure of excitons [174] results in an energy splitting δ_0 between bright and dark exciton subspaces, δ_1 between bright excitons, and δ_2 between dark excitons.

The nuclear Zeeman Hamiltonian is given by

$$H_n^Z = g_n \mu_n B I_z, \quad (\text{C.19})$$

with g_n the nuclear Landé g factor and μ_n the nuclear Bohr magneton. The time-dependent laser Hamiltonian can be written as

$$H_L(t) = \hbar\Omega \left(e^{i\omega_L t} |0\rangle \langle\downarrow\uparrow| + e^{-i\omega_L t} |\downarrow\uparrow\rangle \langle 0| \right), \quad (\text{C.20})$$

where Ω and ω_L are respectively the Rabi and laser frequencies. The electronic hyperfine Hamiltonian within the homogeneous coupling approximation is given by,

$$H_{\text{HF}}^e = A^e \left(S_z I_z + \frac{1}{2} (S_+ I_- + S_- I_+) \right). \quad (\text{C.21})$$

The average hyperfine coupling strength is denoted by A^e . S_z and I_z describe respectively the z -component of the electron spin and total nuclear spin. We have also introduced electronic and nuclear spin ladder operators, $S_{\pm} = S_x \pm iS_y$ and $I_{\pm} = I_x \pm iI_y$. The effective hyperfine Hamiltonian for heavy holes

can be written,

$$H_{\text{HF}}^{\text{h}} = A_z^{\text{h}} S_z^{\text{h}} I_z + A_{\perp,1}^{\text{h}} S_+^{\text{h}} I_- + A_{\perp,1}^{\text{h}*} S_-^{\text{h}} I_+ + A_{\perp,2}^{\text{h}} S_+^{\text{h}} I_+ \\ + A_{\perp,2}^{\text{h}*} S_-^{\text{h}} I_- + A_{\text{nc}}^{\text{h}} S_z^{\text{h}} I_+ + A_{\text{nc}}^{\text{h}*} S_z^{\text{h}} I_-, \quad (\text{C.22})$$

where S_i^{h} ($i = z, \pm$) are pseudospin operators for the heavy hole states.

To get rid of the explicit time-dependence in H_{L} , we perform a similarity transformation $H \rightarrow e^{i\xi t}(H - \xi)e^{-i\xi t}$, with $\xi = E_{\downarrow\uparrow} + \hbar\Delta$ and Δ is the laser detuning. This transformation leaves both hyperfine and nuclear Zeeman Hamiltonians unchanged, whereas H_0 becomes

$$H_0 \rightarrow H'_0 = \frac{\hbar\Delta}{2} (-|0\rangle\langle 0| + |\downarrow\uparrow\rangle\langle\downarrow\uparrow|) + \left(\frac{\hbar\Delta}{2} + E_{\downarrow\uparrow}^{\uparrow\downarrow}\right) |\uparrow\downarrow\rangle\langle\uparrow\downarrow| \\ + \left(\frac{\hbar\Delta}{2} + E_{\downarrow\uparrow}^{\uparrow\uparrow}\right) |\uparrow\uparrow\rangle\langle\uparrow\uparrow| + \left(\frac{\hbar\Delta}{2} + E_{\downarrow\uparrow}^{\downarrow\downarrow}\right) |\downarrow\downarrow\rangle\langle\downarrow\downarrow|, \quad (\text{C.23})$$

with $E_j^i = E_i - E_j$. For the laser Hamiltonian, after performing the similarity transformation, we also make the rotating wave approximation and neglect fast counter-oscillating terms, we find ($H_{\text{L}} \rightarrow H'_{\text{L}}$),

$$H_{\text{L}}(t) \rightarrow H'_{\text{L}} = \hbar\Omega (|0\rangle\langle\downarrow\uparrow| + |\downarrow\uparrow\rangle\langle 0|). \quad (\text{C.24})$$

The total Hamiltonian in the rotating frame and within the rotating wave approximation is thus given by

$$H' = H'_0 + H'_{\text{L}} + H_{\text{n}}^{\text{Z}} + H_{\text{HF}}^{\text{e}} + H_{\text{HF}}^{\text{h}}. \quad (\text{C.25})$$

We further eliminate the flip-flop terms of Hamiltonians Eqs. (C.21) and (C.22) by applying a Schrieffer-Wolf transformation [101, 248] to H' ,

$$H' \rightarrow \tilde{H} = e^S H' e^{-S} = \sum_{j=0}^{\infty} \frac{[S, H']^{(j)}}{j!}, \quad (\text{C.26})$$

where we have defined the recursive relation

$$[S, H']^{(0)} = H', \\ [S, H']^{(1)} = [S, H'], \\ [S, H']^{(j)} = [S, [S, H']^{(j-1)}]. \quad (\text{C.27})$$

We perform the transformation with

$$\begin{aligned}
S = \frac{1}{2} \left[\frac{A^e}{E_{\downarrow\uparrow}^{\uparrow\uparrow}} I_- |\uparrow\uparrow\rangle \langle\downarrow\uparrow| + \frac{A^e}{E_{\downarrow\downarrow}^{\uparrow\downarrow}} I_- |\uparrow\downarrow\rangle \langle\downarrow\downarrow| + \frac{A^e}{E_{\uparrow\downarrow}^{\downarrow\downarrow}} I_+ |\downarrow\downarrow\rangle \langle\uparrow\downarrow| \right. \\
+ \frac{A^e}{E_{\uparrow\uparrow}^{\downarrow\uparrow}} I_+ |\downarrow\uparrow\rangle \langle\uparrow\uparrow| + \frac{A_{\perp,1}^h}{E_{\downarrow\downarrow}^{\downarrow\uparrow}} I_- |\downarrow\uparrow\rangle \langle\downarrow\downarrow| + \frac{A_{\perp,1}^h}{E_{\uparrow\downarrow}^{\uparrow\uparrow}} I_- |\uparrow\uparrow\rangle \langle\uparrow\downarrow| \\
+ \frac{A_{\perp,1}^{h*}}{E_{\uparrow\uparrow}^{\uparrow\downarrow}} I_+ |\uparrow\downarrow\rangle \langle\uparrow\uparrow| + \frac{A_{\perp,1}^{h*}}{E_{\downarrow\downarrow}^{\downarrow\uparrow}} I_+ |\downarrow\downarrow\rangle \langle\downarrow\uparrow| + \frac{A_{\perp,2}^h}{E_{\downarrow\downarrow}^{\downarrow\uparrow}} I_+ |\downarrow\uparrow\rangle \langle\downarrow\downarrow| \\
\left. + \frac{A_{\perp,2}^h}{E_{\uparrow\uparrow}^{\uparrow\downarrow}} I_+ |\uparrow\uparrow\rangle \langle\uparrow\downarrow| + \frac{A_{\perp,2}^{h*}}{E_{\uparrow\uparrow}^{\uparrow\downarrow}} I_- |\uparrow\downarrow\rangle \langle\uparrow\uparrow| + \frac{A_{\perp,2}^{h*}}{E_{\downarrow\downarrow}^{\downarrow\uparrow}} I_- |\downarrow\downarrow\rangle \langle\downarrow\uparrow| \right], \quad (\text{C.28})
\end{aligned}$$

and obtain by keeping only terms that are first order in A^e or A_i^h the following Hamiltonian,

$$\begin{aligned}
\tilde{H} = H'_0 + H'_L + H_Z^{\text{nuc}} + A^e S_z I_z + A_z^h S_z^h I_z + A_{\text{nc}}^h S_z^h (I_+ + I_-) \\
+ \frac{\hbar\Omega}{2} \frac{A^e}{E_{\downarrow\uparrow}^{\uparrow\uparrow}} (I_+ |0\rangle \langle\uparrow\uparrow| + I_- |\uparrow\uparrow\rangle \langle 0|) \\
+ \frac{\hbar\Omega}{2E_{\downarrow\uparrow}^{\downarrow\uparrow}} \left(A_{\perp,1}^h I_- |0\rangle \langle\downarrow\downarrow| + A_{\perp,1}^{h*} I_+ |\downarrow\downarrow\rangle \langle 0| \right) \\
+ \frac{\hbar\Omega}{2E_{\downarrow\uparrow}^{\downarrow\uparrow}} \left(A_{\perp,2}^h I_+ |0\rangle \langle\downarrow\downarrow| + A_{\perp,2}^{h*} I_- |\downarrow\downarrow\rangle \langle 0| \right). \quad (\text{C.29})
\end{aligned}$$

The three last terms in Eq. (C.29) describe hyperfine assisted spin-forbidden optical transitions. These terms are only relevant when the laser detuning is close to resonance either with $|\uparrow\uparrow\rangle$ or $|\downarrow\downarrow\rangle$ [176]. Thus, for Δ close to zero the coherent dynamics of excitons and nuclear spins can be described by

$$H = H'_0 + H'_L + H_Z^{\text{nuc}} + A^e S_z I_z + A_z^h S_z^h I_z + A_{\text{nc}}^h S_z^h (I_+ + I_-). \quad (\text{C.30})$$

Supplementary information for Chapter 5: 'Anisotropic g factor in InAs self-assembled quantum dots'

D.1 Trial wave functions

The Schrödinger equation of a particle confined to a square with sides of length a ,

$$-\frac{\hbar^2}{2m_0} \left(\frac{d^2}{dx^2} + \frac{d^2}{dy^2} \right) \psi^\square(x, y) = E^\square \psi^\square(x, y), \quad (\text{D.1})$$

with boundary conditions $\psi^\square(x, y) = 0$ for $x = 0$, $y = 0$, $x = a$ or $y = a$, has the well-known solution:

$$\psi_{mn}^\square(x, y) = \frac{2}{a} \sin\left(\frac{m\pi}{a}x\right) \sin\left(\frac{n\pi}{a}y\right), \quad (\text{D.2})$$

$$E_{mn}^\square = \frac{\hbar^2\pi^2}{2m_0a^2} (m^2 + n^2). \quad (\text{D.3})$$

The wave function of a particle confined in an isosceles triangle obtained by cutting the square along the diagonal, $\psi^\Delta(x, y)$, is constructed by symmetric and asymmetric linear combination of degenerate solutions to the square problem, ψ_{mn}^\square and ψ_{nm}^\square [202], and we find

$$\psi_{mn}^{\Delta s} = \frac{1}{\sqrt{2}} (\psi_{mn}^\square + \psi_{nm}^\square), \quad (\text{D.4})$$

$$\psi_{mn}^{\Delta a} = \frac{1}{\sqrt{2}} (\psi_{mn}^\square - \psi_{nm}^\square), \quad (\text{D.5})$$

where $\psi_{mn}^{\Delta s}$ ($\psi_{mn}^{\Delta a}$) vanishes at $x + y = a$ for $m + n$ odd (even). The general wave function takes the form

$$\psi_{mn}^\Delta = \frac{1}{\sqrt{2}} (\psi_{mn}^\square + (-1)^{m+n+1} \psi_{nm}^\square), \quad (\text{D.6})$$

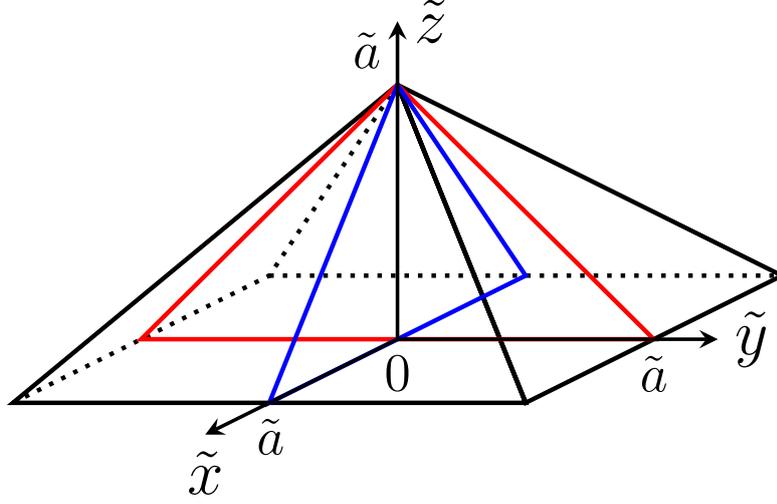


Abbildung D.1: We span the pyramid volume by multiplying two upright isosceles triangles (red and blue). Note that $\tilde{\mathbf{r}}$ and \tilde{a} correspond to \mathbf{r} and a in the main text, respectively. Figure provided by Robert Zielke.

with $m, n = 1, 2, 3, \dots$ and $m \neq n$ to prevent the construction of a vanishing wave function $\psi_{mm}^\Delta = 0$. We apply a coordinate transformation characterized by $x = -[\tilde{x} + (\tilde{y} - \tilde{a})]/2\sqrt{2}$ and $y = [\tilde{x} - (\tilde{y} - \tilde{a})]/2\sqrt{2}$ in order to bring the triangle into upright position, i.e., the apex of the triangle is centered above the base, and find

$$\psi_{mn}^\Delta(\tilde{x}, \tilde{y}) = -\psi_{mn}^\Delta\left(\frac{\tilde{x} + (\tilde{y} - \tilde{a})}{2\sqrt{2}}, \frac{\tilde{x} - (\tilde{y} - \tilde{a})}{2\sqrt{2}}\right), \quad (\text{D.7})$$

with $m, n = 1, 2, 3, \dots$, $m \neq n$, and $\tilde{a} = a/\sqrt{2}$.

Starting from the solution to the two-dimensional Schrödinger equation, we construct an ansatz or trial wave function that is not an eigenfunction of the three-dimensional (3D) Schrödinger equation but nonetheless fulfills the boundary conditions of the pyramid and expected symmetries. We span the 3D volume of the pyramid with the product of two upright triangles, see Fig. D.1, and find the wave function

$$\begin{aligned} \psi_{\mathbf{m}}(\tilde{\mathbf{r}}) &= c \psi_{m_x m_z}^\Delta(\tilde{x}, \tilde{z}) \psi_{m_y m_z}^\Delta(\tilde{y}, \tilde{z}) \\ &= c \prod_{\xi=\tilde{x}, \tilde{y}} \left[\sin(\alpha_\xi \xi^+) \sin(\alpha_z \xi^-) \right. \\ &\quad \left. - (-1)^{m_\xi + m_z} \sin(\alpha_z \xi^+) \sin(\alpha_\xi \xi^-) \right], \end{aligned} \quad (\text{D.8})$$

with $\tilde{\mathbf{r}} = (\tilde{x}, \tilde{y}, \tilde{z})$, $c = \csc(\pi\tilde{z})/N_{\mathbf{m}}$, $\alpha_i = m_i\pi/\tilde{a}$, $m_i = 1, 2, 3, \dots$, $m_x \neq m_z$, $m_y \neq m_z$, $\mathbf{m} = (m_x, m_y, m_z)$, $\xi^\pm = \xi \pm (\tilde{z} - \tilde{a})/2$, and $N_{\mathbf{m}}$ such that the

integral over the pyramid volume yields $\int d^3\tilde{r} |\psi_{\mathbf{m}}(\tilde{\mathbf{r}})|^2 \equiv 1$. Note that we have added the term $\csc(\pi\tilde{z})$ in order to restore the asymptotes at the apex and the base to the correct power law behavior in z that were altered by taking the product $\psi_{m_x m_z}^\Delta \psi_{m_y m_z}^\Delta$. This factor is essential for obtaining s - and p -wave like states. The energies of state $\psi_{\mathbf{m}}$ are given by

$$E_{\mathbf{m}} = \frac{\hbar^2}{2m_0} \langle \psi_{\mathbf{m}}(\tilde{\mathbf{r}}) | (-i\nabla)^2 | \psi_{\mathbf{m}}(\tilde{\mathbf{r}}) \rangle. \quad (\text{D.9})$$

For notational simplicity we use $\psi_{\mathbf{m}} \equiv \psi_{m_x m_y m_z}$. We note that the states $\psi_{m_x m_x m_z}$ and $\psi_{m_z m_z m_x}$ coincide by construction and that $\psi_{m_x m_y m_z}$ and $\psi_{m_y m_x m_z}$ are degenerate.

As mentioned above, $\psi_{\mathbf{m}}$ is not an eigenfunction of the 3D Schrödinger equation. However, the boundary conditions are fulfilled. In addition, the energies $E_{\mathbf{m}}$ are smaller than the eigenenergies of known analytical solutions provided that the correct boundary conditions at the base of the pyramid are taken into account [193]. Furthermore, the set of eigenfunctions reported in Ref. [193] is incomplete and in particular lacks the ground state and states with a non-vanishing particle density (of s -wave type) at the center of the pyramid. In contrast, our trial wave functions form a complete set including states with s - and p -wave character. Despite the fact that $\psi_{\mathbf{m}}$ is not an eigenfunction, we conclude that our trial wave functions provide a good starting point for analytical investigations of pyramidal quantum dots.

D.2 Material parameters

We choose the notation for the parameters exactly as given in Ref. [6]. See Table D.1.

E_g	[eV]	0.418	q		0.39
Δ_0	[eV]	0.380	C_1	[eV]	-5.08 [6, 108]
P	[eVÅ]	9.197	D_d	[eV]	1. [6, 108]
C_k	[eVÅ]	-0.0112	D_u	[eV]	2.7
m^*	$[m_0]$	0.0229	D'_u	[eV]	3.18
g^*		-14.9	C_2	[eV]	1.8 [108, 272]
γ_1		20.40	D'		-2. ¹
γ_2		8.30	C_4	[eVÅ]	11.3 [109, 269]
γ_3		9.10	C_5	[eVÅ]	103.3 [109, 269]
B_{8v}^+	[eVÅ ²]	-3.393	C'_5	[eVÅ]	76.9 [107]
B_{8v}^-	[eVÅ ²]	-0.09511	a_{InAs}	[nm]	6.0583
B_{7v}	[eVÅ ²]	-3.178	a_{GaAs}	[nm]	5.65325
κ		7.60	ν_{InAs}		0.35 [275]

Tabelle D.1: Material parameters used in this chapter. If not stated otherwise, the parameters were taken from Ref. [6].

¹Due to lack of experimentally validated InAs parameters, we use InSb values which are assumed to be close to InAs values [273, 274].

Supplementary information for Chapter 6: 'Strongly interacting holes in Ge/Si nanowires'

E.1 Calculation of the screened Coulomb matrix elements

To calculate the effective 1D, momentum dependent interaction matrix elements $V_{1D}^{ijkl}(q)$ introduced in Eq. (6.3) of the main text, we use the transverse part of the real space wave functions of holes confined to the Ge core of the NW [23], $\phi_{g_{\pm}}(\mathbf{r}_{\perp}) = g_{\pm}(r, \varphi)$ and $\phi_{e_{\pm}}(\mathbf{r}_{\perp}) = e_{\pm}(r, \varphi)$, where \mathbf{r}_{\perp} denotes the transverse part of \mathbf{r} . Due to the hard wall confinement assumed for the derivation of $\phi_{g_{\pm}}(\mathbf{r}_{\perp})$ and $\phi_{e_{\pm}}(\mathbf{r}_{\perp})$, the wave functions are proportional to functions of the type $J_n(r)$, where J_n denotes the n th Bessel function of the first kind. The interaction matrix elements are given by integrals of form

$$V_{1D}^{ijkl}(q) = \iint_{\text{NW}_{\perp}} d\mathbf{r}_{\perp} d\mathbf{r}'_{\perp} \phi_i^{\dagger}(\mathbf{r}_{\perp}) \phi_j^{\dagger}(\mathbf{r}'_{\perp}) V(\mathbf{r}, \mathbf{r}', \mathbf{r}_{\text{mc}}) \phi_k(\mathbf{r}'_{\perp}) \phi_l(\mathbf{r}_{\perp}), \quad (\text{E.1})$$

with $i, j, k, l = g_{\pm}, e_{\pm}$ and $d\mathbf{r}_{\perp} = r dr d\varphi$ ($d\mathbf{r}'_{\perp} = r' dr' d\varphi'$). Here, NW_{\perp} indicates integration over the NW cross section. To perform the integration, we follow the procedure outlined in Ref. [276]. We rewrite the summands of $V(\mathbf{r}, \mathbf{r}', \mathbf{r}_{\text{mc}})$ in terms of discrete Fourier transformations along the NW with wavevector $\mathbf{q} = (0, 0, q)$, which brings the position dependent part of the Coulomb potential to the form

$$\frac{1}{|\mathbf{r} - \mathbf{r}'|} = \frac{1}{\sqrt{(z - z')^2 + a^2}} = \sum_q 2K_0(aq) e^{iq(z-z')}, \quad (\text{E.2})$$

with $a^2 = r^2 + r'^2 - 2rr' \cos(\varphi - \varphi')$, and where $K_m(x)$ denotes the modified Bessel function of second kind. A similar term is obtained for position

dependent part of the screened potential, $1/|\mathbf{r} - \mathbf{r}_{\text{mc}}|$. Equation (E.2) can be simplified further by applying Graf's addition theorem for Bessel functions [277],

$$K_0(aq) = \sum_{m=-\infty}^{\infty} e^{im(\varphi-\varphi')} K_m(qr_>) I_m(qr_<), \quad (\text{E.3})$$

where $r, r' = r_>, r_<$ with $r_> \geq r_<$, while $I_m(x)$ denotes the modified Bessel function of the first kind. We insert the results of Eqs. (E.2) and (E.3) into Eq. (E.1), and integrate out the angular part, $\iint d\varphi d\varphi'$. The remaining non-zero contributions of the sum in Eq. (E.3) are the terms corresponding to $m = 0, \pm 1$. However, this result depends strongly on the exact form of the angular dependence of $\phi_{g\pm}(\mathbf{r}_\perp)$ and $\phi_{e\pm}(\mathbf{r}_\perp)$. The last step, the radial integration $\iint rr' dr dr'$ cannot be performed directly in an analytical manner. To circumvent this, we replace the Bessel functions in Eq. (E.3), and in the wave functions by Taylor expansions around $r, r' = 0$ up to appropriate order. This allows us to evaluate the radial integrals analytically. We have checked numerically that our analytical expressions reproduce the exact result very well.

E.2 Operators and correlation functions in the i, o basis, and transformation to the diagonal basis

For the evaluation of correlation functions, it is helpful to change to a basis in which the matrices \mathcal{H}_ϕ and \mathcal{H}_θ , given in the main text in Eqs. (6.7a) and (6.7b), are diagonal. This can be achieved by the basis change $(\phi_i, \phi_o)^T = W_\phi(\phi_p, \phi_m)^T$ and $(\theta_i, \theta_o)^T = W_\theta(\theta_p, \theta_m)^T$, where W_ϕ and W_θ are matrices with (so far unspecified) real entries $w_{\phi,kl}$ and $w_{\theta,kl}$, and where we have introduced the new fields ϕ_r and θ_r , with $r = p, m$. For this transformation to be canonical, we demand that the new fields obey the commutation relations $[\phi_r(z), \nabla\theta_{r'}(z')] = i\pi\delta_{z,z'}\delta_{r,r'}$ and $[\phi_r(z), \theta_{r'}(z')] = i\pi/2 \text{sgn}(z-z')\delta_{r,r'}$, which fixes 4 of the 8 parameters in W_ϕ and W_θ .

The Hamiltonian densities are transformed as $\tilde{\mathcal{H}}_\phi = (W_\phi)^T \mathcal{H}_\phi W_\phi$ and $\tilde{\mathcal{H}}_\theta = (W_\theta)^T \mathcal{H}_\theta W_\theta$. The requirement that the transformation diagonalizes the Hamiltonian densities fixes two more parameters in W_ϕ and W_θ . The remaining two parameters are finally chosen such that

$$\tilde{\mathcal{H}}_\phi = \tilde{\mathcal{H}}_\theta = \frac{1}{2\pi} \begin{pmatrix} u_p & 0 \\ 0 & u_m \end{pmatrix}, \quad (\text{E.4})$$

with velocities u_p and u_m .

This diagonal basis is particularly convenient if one is interested in evaluating correlation functions of the charge and spin degrees of freedom, where charge and spin are defined in analogy to a Rashba NW (the band E'_{g+} , i.e., the modes L_o and R_i , are thus interpreted as left and right moving modes with spin up, while the band E'_{g-} , i.e., L_i and R_o , are identified with left and right moving spin down modes). The operators describing the integrated charge (ρ) and spin (σ) densities (ϕ_i) and currents (θ_i) are given by

$$\phi_\sigma = -\frac{1}{\sqrt{2}}(\theta_i - \theta_o), \quad \theta_\sigma = -\frac{1}{\sqrt{2}}(\phi_i - \phi_o), \quad (\text{E.5})$$

$$\phi_\rho = \frac{1}{\sqrt{2}}(\phi_i + \phi_o), \quad \theta_\rho = \frac{1}{\sqrt{2}}(\theta_i + \theta_o). \quad (\text{E.6})$$

Using these relations, the operators for the charge density wave (CDW), spin density wave (SDW), singlet superconductivity (SS), and triplet superconductivity (TS) read

$$O_{\text{CDW}}(r) = \frac{1}{\pi\alpha} e^{-ik_{F_o}z} e^{i(\phi_i(r)+\phi_o(r))} \cos[\theta_i(r) - \theta_o(r)], \quad (\text{E.7})$$

$$O_{\text{SDW}}^x(r) = \frac{1}{\pi\alpha} e^{-ik_{F_o}z} e^{i(\phi_i(r)+\phi_o(r))} \cos[\phi_i(r) - \phi_o(r) + k_{F_o}z], \quad (\text{E.8})$$

$$O_{\text{SDW}}^y(r) = \frac{1}{\pi\alpha} e^{-ik_{F_o}z} e^{i(\phi_i(r)+\phi_o(r))} \sin[\phi_i(r) - \phi_o(r) + k_{F_o}z], \quad (\text{E.9})$$

$$O_{\text{SDW}}^z(r) = \frac{i}{\pi\alpha} e^{-ik_{F_o}z} e^{i(\phi_i(r)+\phi_o(r))} \sin[\theta_o(r) - \theta_i(r)], \quad (\text{E.10})$$

$$O_{\text{SS}}(r) = \frac{1}{\pi\alpha} e^{-i(\theta_i(r)+\theta_o(r))} \cos[\theta_i(r) - \theta_o(r)], \quad (\text{E.11})$$

$$O_{\text{TS}}^x(r) = \frac{1}{\pi\alpha} e^{-i(\theta_i(r)+\theta_o(r))} \cos[\phi_i(r) - \phi_o(r) + k_{F_o}z], \quad (\text{E.12})$$

$$O_{\text{TS}}^y(r) = \frac{1}{\pi\alpha} e^{-i(\theta_i(r)+\theta_o(r))} \sin[\phi_i(r) - \phi_o(r) + k_{F_o}z], \quad (\text{E.13})$$

$$O_{\text{TS}}^z(r) = \frac{i}{\pi\alpha} e^{-i(\theta_i(r)+\theta_o(r))} \sin[\theta_o(r) - \theta_i(r)]. \quad (\text{E.14})$$

A detailed discussion of these operators can be found in Ref. [81]. In the

diagonal basis, the associated correlation functions are given by

$$\begin{aligned}\langle O_{\text{CDW}}^\dagger(r)O_{\text{CDW}}(0)\rangle &= \langle O_{\text{SDW}}^{z,\dagger}(r)O_{\text{SDW}}^z(0)\rangle \\ &= \frac{1}{(\pi\alpha)^2}e^{ik_F z}(\alpha/r)^{1/2}(u_{a+}^2+u_{b+}^2+u_{a-}^2+u_{b-}^2),\end{aligned}\quad (\text{E.15})$$

$$\begin{aligned}\langle O_{\text{SDW}}^{x,\dagger}(r)O_{\text{SDW}}^x(0)\rangle &= \langle O_{\text{SDW}}^{y,\dagger}(r)O_{\text{SDW}}^y(0)\rangle \\ &= \frac{1}{4(\pi\alpha)^2}\left[e^{2ik_F z}(\alpha/r)^{1/2}[(u_{a+}-u_{a-})^2+(u_{b+}-u_{b-})^2]\right. \\ &\quad \left. +(\alpha/r)^{1/2}[(u_{a+}+u_{a-})^2+(u_{b+}+u_{b-})^2]\right] \\ &= \langle O_{\text{SDW}}^{y,\dagger}(r)O_{\text{SDW}}^y(0)\rangle_{(2k_F)} + \langle O_{\text{SDW}}^{y,\dagger}(r)O_{\text{SDW}}^y(0)\rangle_{(0)},\end{aligned}\quad (\text{E.16})$$

$$\begin{aligned}\langle O_{\text{SS}}^\dagger(r)O_{\text{SS}}(0)\rangle &= \langle O_{\text{TS}}^{z,\dagger}(r)O_{\text{TS}}^z(0)\rangle \\ &= \frac{1}{4(\pi\alpha)^2}\left[(\alpha/r)^{1/2}[(w_{a+}+w_{a-})^2+(w_{b+}+w_{b-})^2]\right. \\ &\quad \left. +(\alpha/r)^{1/2}[(w_{a+}-w_{a-})^2+(w_{b+}-w_{b-})^2]\right] \\ &= \langle O_{\text{TS}}^{z,\dagger}(r)O_{\text{TS}}^z(0)\rangle_{(+)} + \langle O_{\text{TS}}^{z,\dagger}(r)O_{\text{TS}}^z(0)\rangle_{(-)},\end{aligned}\quad (\text{E.17})$$

$$\begin{aligned}\langle O_{\text{TS}}^{x,\dagger}(r)O_{\text{TS}}^x(0)\rangle &= \langle O_{\text{TS}}^{y,\dagger}(r)O_{\text{TS}}^y(0)\rangle \\ &= \frac{1}{(\pi\alpha)^2}(\alpha/r)^{1/2}(u_{a-}^2+u_{b-}^2+u_{a+}^2+u_{b+}^2),\end{aligned}\quad (\text{E.18})$$

with $u_{a,\pm} = w_{\phi,21} \pm w_{\phi,11}$, $u_{b,\pm} = w_{\phi,22} \pm w_{\phi,21}$, $w_{a,\pm} = w_{\theta,21} \pm w_{\theta,11}$, $w_{b,\pm} = w_{\theta,22} \pm w_{\theta,12}$. Note that the correlation functions for $\text{SDW}_{x,y}$, SS , and TS_z each contain two terms with (slightly) different exponents.

E.3 Divergences outside the perturbative regime and comparison to a fermionic RG approach

As discussed in the main text, the use of a perturbative RG approach for the coupling g_I restricts our analysis to a regime in which the associated dimensionless coupling satisfies $2g_I/(u_p + u_m) \ll 1$. In this regime, g_I is found to be RG irrelevant. When leaving the perturbative regime, we find that the scaling exponents diverge at a finite field E_\perp (solid lines in Fig. E.1). These divergences can be traced back to the fact that the off-diagonal matrix ele-

ments in the Hamiltonian given in Eq. (6.7) are so large that the velocity u_m of the diagonalized Hamiltonian vanishes. The system thus seems to exhibit a Wentzel-Bardeen singularity [212–215]. This apparent divergence, however, occurs outside the perturbative regime, and is thus beyond the range of validity of our calculation (we note that during the RG flow, the quadratic sector of the theory is renormalized by corrections of the order $\mathcal{O}(g_I^2)$, see Ref. [81]).

As an independent cross-check for the absence of singularities in the regime described by our calculation, we compare the scaling exponents of the correlation functions discussed in the main text to the analogous exponents obtained when the system is bosonized only after an initial fermionic one-loop RG treatment, which in particular already describes the flow of g_I to weak coupling. To this end, we start from the fermionic Hamiltonian with the interactions given in Eqs. (6.4) - (6.6), and perform a fermionic one-loop RG analysis following Refs. [216] and [217]. This yields the one-loop RG equations

$$\frac{d\bar{g}_2}{dl} = -\bar{g}_I(l)^2, \quad \frac{d\bar{g}_I}{dl} = -\bar{g}_I(l)\bar{g}_2(l), \quad (\text{E.19})$$

where we have introduced the definitions $\pi\bar{g}_2 = g_{2_o}/(2v_{F_o}) + g_{2_i}/(2v_{F_i}) - 2(g_{2_{io}} - g_{1_{io1}})/(v_{F_o} + v_{F_i})$ and $\pi\bar{g}_I = g_I\sqrt{2(1+\gamma)}/(v_{F_o} + v_{F_i})$, with $\gamma = (v_{F_o} + v_{F_i})^2/(4v_{F_o}v_{F_i})$. Integrating these RG equations yields the fixed point values $\bar{g}_I^* = 0$ and $\bar{g}_2^* = (\bar{g}_2^2(0) - \bar{g}_I^2(0))^{1/2}$ [81], from which we find $g_{2_o}^*$, $g_{2_i}^*$ and $g_{2_{io}}^* - g_{1_{io1}}^*$. We plug these renormalized interactions back into the fermionic Hamiltonian. The bosonization of this renormalized Hamiltonian in turn yields a purely quadratic bosonic theory, which finally allows to calculate the exponents of the various correlation functions just as discussed in the main text.

In the perturbative regime, we find that the qualitative behavior of the scaling exponents is identical for both approaches. Outside the perturbative regime, this is not true. There, the presence or absence of a divergence of the scaling exponents calculated using the fermionic one-loop approach depends on the NW parameters, while the bosonic approach seems to generically exhibit a singularity.

Most importantly, however, we find that - if present - the divergences always appear outside the range of validity of our calculation. This finding is illustrated in Fig. E.1, where we plot the exponents obtained in the bosonic sine-Gordon approach (solid lines), and the exponents obtained when bosonizing after the fermionic one-loop RG treatment (dashed lines). The black vertical lines denote the limits of the perturbative regime, i.e., the black solid

line indicates where

$$\frac{g_I}{\frac{1}{2}(u_p + u_m)} \approx 1, \quad (\text{E.20})$$

while the black dashed line depicts where

$$\bar{g}_2 = \frac{g_{2o}}{2\pi v_{F_o}} + \frac{g_{2i}}{2\pi v_{F_i}} - \frac{2(g_{2io} - g_{1io1})}{\pi(v_{F_o} + v_{F_i})} \approx 1. \quad (\text{E.21})$$

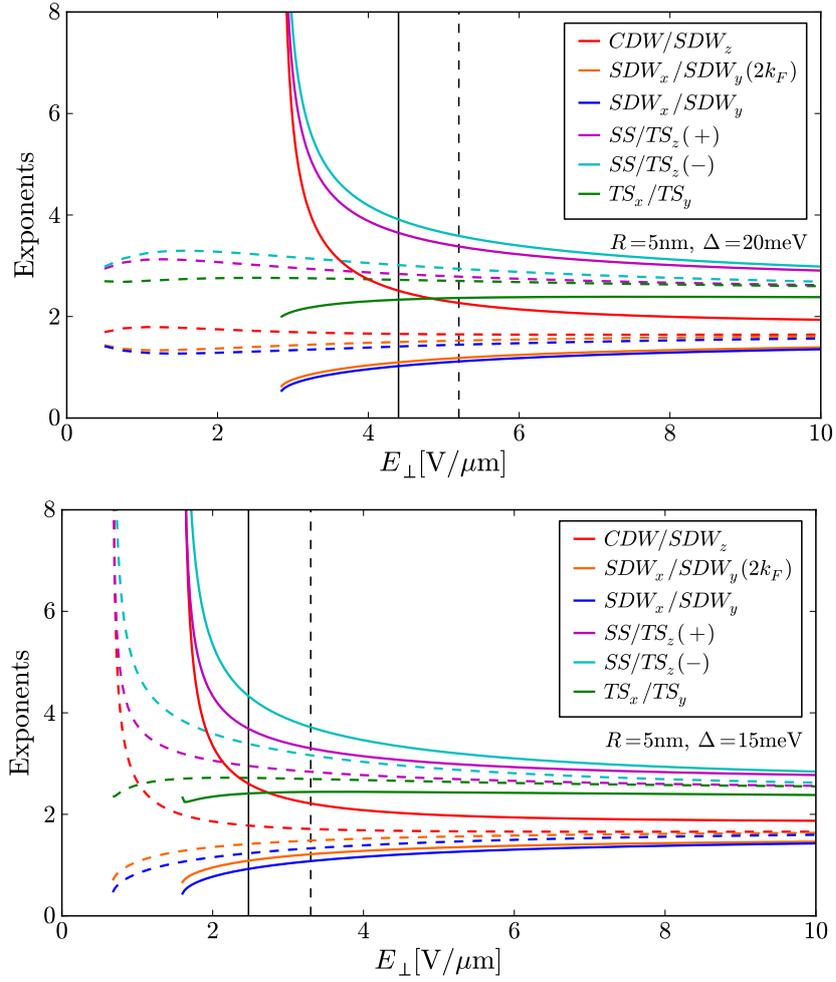


Abbildung E.1: The exponents of the correlation functions for two different sets of NW parameters R and Δ as functions of E_{\perp} , where $\varphi_E = 3\pi/2$ and $\mathbf{r}_{\text{mc}} = (0, |\mathbf{r}_{\text{mc}}|, 0)$ with $|\mathbf{r}_{\text{mc}}| = 100$ nm. We show the exponents obtained by two different RG approaches, a bosonic sine-Gordon RG approach (solid lines), and a fermionic one-Loop RG calculation (dashed lines). The black vertical lines denote where the perturbative regime ends for either of the two RG approaches. In contrast to the bosonic approach, where the scaling exponents always diverge, the presence of a divergence of the scaling exponents for the fermionic approach depends on the NW parameters.

Supplementary information for Chapter 7: 'Majorana fermions in Ge/Si hole nanowires'

F.1 Particle-hole coupling Hamiltonian

In this section, we display the effective Bogoliubov-de-Gennes Hamiltonian for holes in the lowest-energy subband. To allow for a direct comparison with previous results [249], we rotate the lowest-energy basis Ψ_{ph} [introduced above Eq.(7.16)] such that the spin quantization axis lies parallel to the applied electric field E_x and the new particle-hole basis reads $\tilde{\Psi}_{ph} = (\Psi_+, \Psi_-, \Psi_+^\dagger, \Psi_-^\dagger)$, where the \pm denotes the pseudospin of the SOI split subband. The Hamiltonian is given by $\tilde{H}_{ph} = \frac{1}{2} \int \tilde{\Psi}_{ph}^\dagger \tilde{\mathcal{H}}_{ph} \tilde{\Psi}_{ph}$ with Hamiltonian density

$$\tilde{\mathcal{H}}_{ph} = \begin{pmatrix} \frac{\hbar^2 k_z^2}{2m_{\text{eff}}} - \mu + \tilde{\alpha}k_z & i\Delta_Z e^{i\vartheta_B} & 0 & \Delta_{sc} \\ -i\Delta_Z e^{-i\vartheta_B} & \frac{\hbar^2 k_z^2}{2m_{\text{eff}}} - \mu - \tilde{\alpha}k_z & -\Delta_{sc} & 0 \\ 0 & -\Delta_{sc}^* & -\frac{\hbar^2 k_z^2}{2m_{\text{eff}}} + \mu + \tilde{\alpha}k_z & i\Delta_Z e^{-i\vartheta_B} \\ \Delta_{sc}^* & 0 & -i\Delta_Z e^{i\vartheta_B} & -\frac{\hbar^2 k_z^2}{2m_{\text{eff}}} + \mu - \tilde{\alpha}k_z \end{pmatrix}. \quad (\text{F.1})$$

Here, we used the abbreviations $\tilde{\alpha} = E_x \alpha_{\text{eff}}$ and $\Delta_Z e^{i\vartheta_B} = \mu_B (B_x g_x + i B_z g_z)$. A similar Hamiltonian was used in Ref. [249] to derive MF wave functions in NWs with proximity-induced superconductivity. Note that our model additionally includes a complex superconducting pairing potential and a Zeeman term reflecting the anisotropy of the g factor of the NW.

F.2 Wave functions

Here we display the explicit form of the MF wave functions in both the strong and weak SOI regime.

Strong SOI

In the strong SOI regime, the MF wave function introduced above Eq. (7.21) in Sec. 7.3 is given by

$$\hat{\Phi}_s(z) = e^{-i\pi/4} e^{-z/\xi_s^e} \begin{pmatrix} ie^{i\vartheta_B^0/2} e^{ik_F^s z} \\ -ie^{-i\vartheta_B^0/2} e^{-ik_F^s z} \\ e^{-i\vartheta_B^0/2} e^{-ik_F^s z} \\ -e^{i\vartheta_B^0/2} e^{ik_F^s z} \end{pmatrix} + e^{-i\pi/4} e^{-z/\xi_s^i} \begin{pmatrix} -ie^{i\vartheta_B^0/2} \\ ie^{-i\vartheta_B^0/2} \\ -e^{-i\vartheta_B^0/2} \\ e^{i\vartheta_B^0/2} \end{pmatrix}, \quad (\text{F.2})$$

where $\hat{\Phi}_s(z)$ is written in the basis $\tilde{\Psi}_{ph}$ (see Appendix F.1).

Weak SOI

In the weak SOI regime, the MF wave function introduced above Eq. (7.24) in Sec. 7.3 is given by

$$\hat{\Phi}_w(z) = 2e^{-z/\xi_w^{(i)}} \frac{k_{so}}{k_F^w} e^{-i\pi/4} \begin{pmatrix} -ie^{i\vartheta_B^0/2} \\ ie^{-i\vartheta_B^0/2} \\ -e^{-i\vartheta_B^0/2} \\ e^{i\vartheta_B^0/2} \end{pmatrix} + \frac{e^{-z/\xi_w^{(e)}}}{\sqrt{2}} \begin{pmatrix} e^{i\vartheta_B^0/2} \left[\left(1 - \frac{k_{so}}{k_F^w}\right) \left(1 - i\frac{k_{so}}{k_F^w}\right) e^{ik_F^w z} - \left(1 + \frac{k_{so}}{k_F^w}\right) \left(1 + i\frac{k_{so}}{k_F^w}\right) e^{-ik_F^w z} \right] \\ e^{-i\vartheta_B^0/2} \left[\left(1 + \frac{k_{so}}{k_F^w}\right) \left(i + \frac{k_{so}}{k_F^w}\right) e^{ik_F^w z} - \left(1 - \frac{k_{so}}{k_F^w}\right) \left(i - \frac{k_{so}}{k_F^w}\right) e^{-ik_F^w z} \right] \\ e^{-i\vartheta_B^0/2} \left[\left(1 - \frac{k_{so}}{k_F^w}\right) \left(1 + i\frac{k_{so}}{k_F^w}\right) e^{-ik_F^w z} - \left(1 + \frac{k_{so}}{k_F^w}\right) \left(1 - i\frac{k_{so}}{k_F^w}\right) e^{ik_F^w z} \right] \\ e^{i\vartheta_B^0/2} \left[\left(1 + \frac{k_{so}}{k_F^w}\right) \left(-i + \frac{k_{so}}{k_F^w}\right) e^{-ik_F^w z} - \left(1 - \frac{k_{so}}{k_F^w}\right) \left(-i - \frac{k_{so}}{k_F^w}\right) e^{ik_F^w z} \right] \end{pmatrix}, \quad (\text{F.3})$$

where $\hat{\Phi}_w(z)$ is written in the basis $\tilde{\Psi}_{ph}$ (see Appendix F.1). For very weak SOI ($k_{so}/k_F^w \ll 1$) the MF wave function simplifies to

$$\hat{\Phi}_w(z) \approx \sqrt{2} \sin(k_F^w z) e^{-z/\xi_w^{(e)}} \begin{pmatrix} ie^{i\vartheta_B^0/2} \\ -e^{-i\vartheta_B^0/2} \\ -ie^{-i\vartheta_B^0/2} \\ -e^{i\vartheta_B^0/2} \end{pmatrix}. \quad (\text{F.4})$$

Literaturverzeichnis

- [1] P. Y. Yu and M. Cardona, *Fundamentals of Semiconductors* (Springer, Berlin, 1996).
- [2] O. Gywat, H. J. Krenner, and J. Berezovsky, *Spins in optically active quantum dots: concepts and methods* (John Wiley & Sons, 2009).
- [3] K. A. Dick, *Prog. Cryst. Growth Ch.* **54**, 138 (2008).
- [4] N. Wang, Y. Cai, and R. Zhang, *Mater. Sci. Eng. R-Rep.* **60**, 1 (2008).
- [5] S. Barth, F. Hernandez-Ramirez, J. D. Holmes, and A. Romano-Rodriguez, *Prog. Mater. Sci.* **55**, 563 (2010).
- [6] R. Winkler, *Spin-Orbit Coupling Effects in Two-Dimensional Electron and Hole Systems* (Springer, Berlin, 2003).
- [7] J. M. Luttinger, *Phys. Rev.* **102**, 1030 (1956).
- [8] S. Adachi, *Properties of group-IV, III-V and II-VI semiconductors* (John Wiley & Sons, 2005).
- [9] T. Walther, A. G. Cullis, D. J. Norris, and M. Hopkinson, *Phys. Rev. Lett.* **86**, 2381 (2001).
- [10] J. Stangl, V. Holý, and G. Bauer, *Rev. Mod. Phys.* **76**, 725 (2004).
- [11] R. Warburton, B. Miller, C. Dürr, C. Bödefeld, K. Karrai, J. Kotthaus, G. Medeiros-Ribeiro, P. Petroff, and S. Huant, *Phys. Rev. B* **58**, 16221 (1998).
- [12] M. Grundmann, O. Stier, and D. Bimberg, *Phys. Rev. B* **52**, 11969 (1995).

- [13] M. Tadić, F. M. Peeters, K. L. Janssens, M. Korkusiński, and P. Hawrylak, *J. Appl. Phys.* **92**, 5819 (2002).
- [14] S. Seidl, M. Kroner, A. Högele, K. Karrai, R. J. Warburton, A. Badolato, and P. M. Petroff, *Appl. Phys. Lett.* **88**, 203113 (2006).
- [15] F. Ding, R. Singh, J. D. Plumhof, T. Zander, V. Křápek, Y. H. Chen, M. Benyoucef, V. Zwiller, K. Dörr, G. Bester, A. Rastelli, and O. G. Schmidt, *Phys. Rev. Lett.* **104**, 067405 (2010).
- [16] J. Grönqvist, N. Søndergaard, F. Boxberg, T. Guhr, S. Åberg, and H. Q. Xu, *J. Appl. Phys.* **106**, 053508 (2009).
- [17] C. Kloeffel, M. Trif, and D. Loss, *Phys. Rev. B* **90**, 115419 (2014).
- [18] F. J. Ohkawa and Y. Uemura, *J. Phys. Soc. Japan* **37**, 1325 (1974).
- [19] Y. A. Bychkov and E. I. Rashba, *J. Phys. C* **17**, 6039 (1984).
- [20] G. Dresselhaus, *Phys. Rev.* **100**, 580 (1955).
- [21] A. V. Khaetskii and Y. V. Nazarov, *Phys. Rev. B* **64**, 125316 (2001).
- [22] P. Středa and P. Šeba, *Phys. Rev. Lett.* **90**, 256601 (2003).
- [23] C. Kloeffel, M. Trif, and D. Loss, *Phys. Rev. B* **84**, 195314 (2011).
- [24] C. Fasth, A. Fuhrer, L. Samuelson, V. N. Golovach, and D. Loss, *Phys. Rev. Lett.* **98**, 266801 (2007).
- [25] S. Takahashi, R. S. Deacon, K. Yoshida, A. Oiwa, K. Shibata, K. Hirakawa, Y. Tokura, and S. Tarucha, *Phys. Rev. Lett.* **104**, 246801 (2010).
- [26] C. H. L. Quay, T. L. Hughes, J. A. Sulpizio, L. N. Pfeiffer, K. W. Baldwin, K. W. West, D. Goldhaber-Gordon, and R. de Picciotto, *Nature Phys.* **6**, 336 (2010).
- [27] D. Rainis and D. Loss, *Phys. Rev. B* **90**, 235415 (2014).
- [28] R. Hanson, L. P. Kouwenhoven, J. R. Petta, S. Tarucha, and L. M. K. Vandersypen, *Rev. Mod. Phys.* **79**, 1217 (2007).
- [29] D. Loss and D. P. DiVincenzo, *Phys. Rev. A* **57**, 120 (1998).
- [30] D. P. DiVincenzo, *Fortschr. Phys.* **48**, 771 (2000).

- [31] M. Atatüre, J. Dreiser, A. Badolato, A. Högele, K. Karrai, and A. Imamoglu, *Science* **312**, 551 (2006).
- [32] M. Atatüre, J. Dreiser, A. Badolato, and A. Imamoglu, *Nature Phys.* **3**, 101 (2007).
- [33] D. Heiss, S. Schaeck, H. Huebl, M. Bichler, G. Abstreiter, J. J. Finley, D. V. Bulaev, and D. Loss, *Phys. Rev. B* **76**, 241306 (2007).
- [34] M. Mikkelsen, J. Berezovsky, N. Stoltz, L. Coldren, and D. Awschalom, *Nature Phys.* **3**, 770 (2007).
- [35] J. Berezovsky, M. H. Mikkelsen, N. G. Stoltz, L. A. Coldren, and D. D. Awschalom, *Science* **320**, 349 (2008).
- [36] D. Press, T. D. Ladd, B. Zhang, and Y. Yamamoto, *Nature* **456**, 218 (2008).
- [37] B. D. Gerardot, D. Brunner, P. A. Dalgarno, P. Öhberg, S. Seidl, M. Kroner, K. Karrai, N. G. Stoltz, P. M. Petroff, and R. J. Warburton, *Nature* **451**, 441 (2008).
- [38] B. Eble, P. Desfonds, F. Fras, F. Bernardot, C. Testelin, M. Chamarro, A. Miard, and A. Lemaître, *J. Phys.: Conf. Ser.* **210**, 012031 (2010).
- [39] T. M. Godden, S. J. Boyle, A. J. Ramsay, A. M. Fox, and M. S. Skolnick, *Appl. Phys. Lett.* **97**, 061113 (2010).
- [40] D. Press, K. De Greve, P. L. McMahon, T. D. Ladd, B. Friess, C. Schneider, M. Kamp, S. Höfling, A. Forchel, and Y. Yamamoto, *Nature Phot.* **4**, 367 (2010).
- [41] K. De Greve, P. L. McMahon, D. Press, T. D. Ladd, D. Bisping, C. Schneider, M. Kamp, L. Worschech, S. Höfling, A. Forchel, and Y. Yamamoto, *Nature Phys.* **7**, 872 (2011).
- [42] A. Greilich, S. G. Carter, D. Kim, A. Bracker, and D. Gammon, *Nature Phot.* **5**, 702 (2011).
- [43] T. M. Godden, J. H. Quilter, A. J. Ramsay, Y. Wu, P. Brereton, S. J. Boyle, I. J. Luxmoore, J. Puebla-Nunez, A. M. Fox, and M. S. Skolnick, *Phys. Rev. Lett.* **108**, 017402 (2012).

- [44] A. Barenco, C. H. Bennett, R. Cleve, D. P. DiVincenzo, N. Margolus, P. Shor, T. Sleator, J. A. Smolin, and H. Weinfurter, *Phys. Rev. A* **52**, 3457 (1995).
- [45] C. Kloeffel and D. Loss, *Annu. Rev. Cond. Mat. Phys.* **4**, 51 (2013).
- [46] F. H. L. Koppens, C. Buizert, K. J. Tielrooij, I. T. Vink, K. C. Nowack, T. Meunier, L. P. Kouwenhoven, and L. M. K. Vandersypen, *Nature* **442**, 766 (2006).
- [47] M. Pioro-Ladrière, T. Obata, Y. Tokura, Y.-S. Shin, T. Kubo, K. Yoshida, T. Taniyama, and S. Tarucha, *Nature Phys.* **4**, 776 (2008).
- [48] Y. Kato, R. C. Myers, D. C. Driscoll, A. C. Gossard, J. Levy, and D. D. Awschalom, *Science* **299**, 1201 (2003).
- [49] J. Pingenot, C. E. Pryor, and M. E. Flatté, *Appl. Phys. Lett.* **92**, 222502 (2008).
- [50] J. Pingenot, C. E. Pryor, and M. E. Flatté, *Phys. Rev. B* **84**, 195403 (2011).
- [51] A. J. Bennett, M. A. Pooley, Y. Cao, N. Sköld, I. Farrer, D. A. Ritchie, and A. J. Shields, *Nature Commun.* **4**, 1522 (2013).
- [52] V. N. Golovach, M. Borhani, and D. Loss, *Phys. Rev. B* **74**, 165319 (2006).
- [53] D. V. Bulaev and D. Loss, *Phys. Rev. Lett.* **98**, 097202 (2007).
- [54] S. J. Devitt, W. J. Munro, and K. Nemoto, *Rep. Prog. Phys.* **76**, 076001 (2013).
- [55] J. R. Petta, A. C. Johnson, J. M. Taylor, E. A. Laird, A. Yacoby, M. D. Lukin, C. M. Marcus, M. P. Hanson, and A. C. Gossard, *Science* **309**, 2180 (2005).
- [56] M. A. Stroscio and M. Dutta, *Phonons in Nanostructures* (Cambridge University Press, 2001).
- [57] A. N. Cleland, *Foundations of Nanomechanics: From Solid-State Theory to Device Applications* (Springer, Berlin, 2003).
- [58] U. Roessler, *Solid State Theory: An Introduction* (Physica-Verlag, 2009).

- [59] V. N. Golovach, A. Khaetskii, and D. Loss, Phys. Rev. Lett. **93**, 016601 (2004).
- [60] D. V. Bulaev and D. Loss, Phys. Rev. Lett. **95**, 076805 (2005).
- [61] A. Abragam, *The principles of nuclear magnetism* (Oxford University Press, New York, 1961).
- [62] A. M. Stoneham, *Theory of Defects in Solids* (Oxford University Press, New York, 1972).
- [63] W. A. Coish and J. Baugh, Phys. Status Solidi B **8**, 2203 (2009).
- [64] J. Fischer, W. A. Coish, D. V. Bulaev, and D. Loss, Phys. Rev. B **78**, 155329 (2008).
- [65] P. Fallahi, S. T. Yilmaz, and A. Imamoğlu, Phys. Rev. Lett. **105**, 257402 (2010).
- [66] E. A. Chekhovich, A. B. Krysa, M. S. Skolnick, and A. I. Tartakovskii, Phys. Rev. Lett. **106**, 027402 (2011).
- [67] W. A. Coish and D. Loss, Phys. Rev. B **70**, 195340 (2004).
- [68] B. Urbaszek, X. Marie, T. Amand, O. Krebs, P. Voisin, P. Maletinsky, A. Högele, and A. Imamoglu, Rev. Mod. Phys. **85**, 79 (2013).
- [69] E. A. Laird, C. Barthel, E. I. Rashba, C. M. Marcus, M. P. Hanson, and A. C. Gossard, Phys. Rev. Lett. **99**, 246601 (2007).
- [70] J. R. Petta, J. M. Taylor, A. C. Johnson, A. Yacoby, M. D. Lukin, C. M. Marcus, M. P. Hanson, and A. C. Gossard, Phys. Rev. Lett. **100**, 067601 (2008).
- [71] H. Bluhm, S. Foletti, D. Mahalu, V. Umansky, and A. Yacoby, Phys. Rev. Lett. **105**, 216803 (2010).
- [72] J. Danon, I. T. Vink, F. H. L. Koppens, K. C. Nowack, L. M. K. Vandersypen, and Y. V. Nazarov, Phys. Rev. Lett. **103**, 046601 (2009).
- [73] I. T. Vink, K. C. Nowack, F. H. J. Koppens, J. Danon, Y. V. Nazarov, and L. M. K. Vandersypen, Nature Phys. **5**, 764 (2009).
- [74] D. Klauser, W. A. Coish, and D. Loss, Phys. Rev. B **73**, 205302 (2006).

- [75] D. Stepanenko, G. Burkard, G. Giedke, and A. Imamoglu, *Phys. Rev. Lett.* **96**, 136401 (2006).
- [76] A. Greilich, A. Shabaev, D. Yakovlev, A. L. Efros, I. A. Yugova, D. Reuter, A. Wieck, and M. Bayer, *Science* **317**, 1896 (2007).
- [77] D. J. Reilly, J. M. Taylor, J. R. Petta, C. M. Marcus, M. P. Hanson, and A. C. Gossard, *Science* **321**, 817 (2008).
- [78] F. A. Zwanenburg, A. S. Dzurak, A. Morello, M. Y. Simmons, L. C. L. Hollenberg, G. Klimeck, S. Rogge, S. N. Coppersmith, and M. A. Eriksson, *Rev. Mod. Phys.* **85**, 961 (2013).
- [79] G. D. Mahan, *Many-Particle Physics* (Plenum, New York, N.Y., 1990).
- [80] J. Voit, *Reports on Progress in Physics* **58**, 977 (1995).
- [81] T. Giamarchi, *Quantum physics in one dimension* (Clarendon Press, Oxford, 2003).
- [82] N. D. Mermin and H. Wagner, *Phys. Rev. Lett.* **17**, 1133 (1966).
- [83] P. C. Hohenberg, *Phys. Rev.* **158**, 383 (1967).
- [84] J. von Delft and H. Schoeller, *Ann. Phys.* **7**, 225 (1998).
- [85] E. Majorana, *Nuovo Cimento* **5**, 171 (1937).
- [86] R. M. Lutchyn, J. D. Sau, and S. Das Sarma, *Phys. Rev. Lett.* **105**, 077001 (2010).
- [87] Y. Oreg, G. Refael, and F. von Oppen, *Phys. Rev. Lett.* **105**, 177002 (2010).
- [88] J. Alicea, *Phys. Rev. B* **81**, 125318 (2010).
- [89] L. Mao, M. Gong, E. Dumitrescu, S. Tewari, and C. Zhang, *Phys. Rev. Lett.* **108**, 177001 (2012).
- [90] V. Mourik, K. Zuo, S. M. Frolov, S. R. Plissard, E. P. A. M. Bakkers, and L. P. Kouwenhoven, *Science* **336**, 1003 (2012).
- [91] A. Das, Y. Ronen, Y. Most, Y. Oreg, M. Heiblum, and H. Shtrikman, *Nature Phys.* **8**, 887 (2012).

- [92] M. T. Deng, C. L. Yu, G. Y. Huang, M. Larsson, P. Caroff, and H. Q. Xu, *Nano Lett.* **12**, 6414 (2012).
- [93] L. P. Rokhinson, X. Liu, and J. K. Furdyna, *Nature Phys.* **8**, 795 (2012).
- [94] H. O. H. Churchill, V. Fatemi, K. Grove-Rasmussen, M. T. Deng, P. Caroff, H. Q. Xu, and C. M. Marcus, *Phys. Rev. B* **87**, 241401 (2013).
- [95] N. Read and D. Green, *Phys. Rev. B* **61**, 10267 (2000).
- [96] A. Y. Kitaev, *Phys. Uspekhi* **44**, 131 (2001).
- [97] C. Nayak, S. H. Simon, A. Stern, M. Freedman, and S. Das Sarma, *Rev. Mod. Phys.* **80**, 1083 (2008).
- [98] C. Beenakker, *Annu. Rev. Condens. Matter Phys.* **4**, 113 (2013).
- [99] A. Stern and N. H. Lindner, *Science* **339**, 1179 (2013).
- [100] E. Kane, *J. Phys. Chem. Solids.* **1**, 249 (1957).
- [101] J. R. Schrieffer and P. A. Wolff, *Phys. Rev.* **149**, 491 (1966).
- [102] M. Trif, P. Simon, and D. Loss, *Phys. Rev. Lett.* **103**, 106601 (2009).
- [103] D. Brunner, B. D. Gerardot, P. A. Dalgarno, G. Wüst, K. Karrai, N. G. Stoltz, P. M. Petroff, and R. J. Warburton, *Science* **325**, 70 (2009).
- [104] J. Fischer and D. Loss, *Phys. Rev. Lett.* **105**, 266603 (2010).
- [105] B. Eble, C. Testelin, P. Desfonds, F. Bernardot, A. Balocchi, T. Amand, A. Miard, A. Lemaître, X. Marie, and M. Chamarro, *Phys. Rev. Lett.* **102**, 146601 (2009).
- [106] C. Testelin, F. Bernardot, B. Eble, and M. Chamarro, *Phys. Rev. B* **79**, 195440 (2009).
- [107] H. R. Trebin, U. Rössler, and R. Ranvaud, *Phys. Rev. B* **20**, 686 (1979).
- [108] I. Vurgaftman, J. Meyer, and L. Ram-Mohan, *J. Appl. Phys.* **89**, 5815 (2001).
- [109] R. Ranvaud, H. R. Trebin, U. Rössler, and F. H. Pollak, *Phys. Rev. B* **20**, 701 (1979).

- [110] M. Gueron, *Phys. Rev.* **135**, A200 (1964).
- [111] E. Clementi and D. L. Raimondi, *J. Chem. Phys.* **38**, 2686 (1963).
- [112] E. Clementi, D. L. Raimondi, and W. P. Reinhardt, *J. Chem. Phys.* **47**, 1300 (1967).
- [113] W. A. Coish, J. Fischer, and D. Loss, *Phys. Rev. B* **81**, 165315 (2010).
- [114] R. N. Bhargava and M. I. Nathan, *Phys. Rev.* **161**, 695 (1967).
- [115] Y.-J. Doh, J. A. van Dam, A. L. Roest, E. P. A. M. Bakkers, L. P. Kouwenhoven, and S. De Franceschi, *Science* **309**, 272 (2005).
- [116] H. A. Nilsson, P. Caroff, C. Thelander, M. Larsson, J. B. Wagner, L.-E. Wernersson, L. Samuelson, and H. Q. Xu, *Nano Lett.* **9**, 3151 (2009).
- [117] S. Nadj-Perge, S. M. Frolov, E. P. A. M. Bakkers, and L. P. Kouwenhoven, *Nature* **468**, 1084 (2010).
- [118] M. D. Schroer, K. D. Petersson, M. Jung, and J. R. Petta, *Phys. Rev. Lett.* **107**, 176811 (2011).
- [119] S. Nadj-Perge, V. S. Pribiag, J. W. G. van den Berg, K. Zuo, S. R. Plissard, E. P. A. M. Bakkers, S. M. Frolov, and L. P. Kouwenhoven, *Phys. Rev. Lett.* **108**, 166801 (2012).
- [120] K. D. Petersson, L. W. McFaul, M. D. Schroer, M. Jung, J. M. Taylor, A. A. Houck, and J. R. Petta, *Nature* **490**, 380 (2012).
- [121] J. W. G. van den Berg, S. Nadj-Perge, V. S. Pribiag, S. R. Plissard, E. P. A. M. Bakkers, S. M. Frolov, and L. P. Kouwenhoven, *Phys. Rev. Lett.* **110**, 066806 (2013).
- [122] L. J. Lauhon, M. S. Gudiksen, D. Wang, and C. M. Lieber, *Nature* **420**, 57 (2002).
- [123] W. Lu, J. Xiang, B. P. Timko, Y. Wu, and C. M. Lieber, *Proc. Natl. Acad. Sci. USA* **102**, 10046 (2005).
- [124] J. Xiang, A. Vidan, M. Tinkham, R. M. Westervelt, and C. M. Lieber, *Nat. Nanotechnol.* **1**, 208 (2006).
- [125] J. Xiang, W. Lu, Y. Hu, Y. Wu, H. Yan, and C. M. Lieber, *Nature* **441**, 489 (2006).

- [126] Y. Hu, H. O. H. Churchill, D. J. Reilly, J. Xiang, C. M. Lieber, and C. M. Marcus, *Nature Nanotechnol.* **2**, 622 (2007).
- [127] S. Roddaro, A. Fuhrer, C. Fasth, L. Samuelson, J. Xiang, and C. M. Lieber, arXiv:0706.2883 .
- [128] S. Roddaro, A. Fuhrer, P. Brusheim, C. Fasth, H. Q. Xu, L. Samuelson, J. Xiang, and C. M. Lieber, *Phys. Rev. Lett.* **101**, 186802 (2008).
- [129] X.-J. Hao, T. Tu, G. Cao, C. Zhou, H.-O. Li, G.-C. Guo, W. Y. Fung, Z. Ji, G.-P. Guo, and W. Lu, *Nano Lett.* **10**, 2956 (2010).
- [130] H. Yan, H. S. Choe, S. Nam, Y. Hu, S. Das, J. F. Klemic, J. C. Ellenbogen, and C. M. Lieber, *Nature* **470**, 240 (2011).
- [131] J. Nah, D. C. Dillen, K. M. Varahramyan, S. K. Banerjee, and E. Tutuc, *Nano Lett.* **12**, 108 (2012).
- [132] Y. Hu, F. Kuemmeth, C. M. Lieber, and C. M. Marcus, *Nature Nanotechnol.* **7**, 47 (2012).
- [133] J. J. Zhang, G. Katsaros, F. Montalenti, D. Scopece, R. O. Rezaev, C. Mickel, B. Rellinghaus, L. Miglio, S. De Franceschi, A. Rastelli, and O. G. Schmidt, *Phys. Rev. Lett.* **109**, 085502 (2012).
- [134] V. S. Pribiag, S. Nadj-Perge, S. M. Frolov, J. W. G. van den Berg, I. van Weperen, S. R. Plissard, E. P. A. M. Bakkers, and L. P. Kouwenhoven, *Nature Nanotechnol.* **8**, 170 (2013).
- [135] C. B. Simmons, J. R. Prance, B. J. Van Bael, T. S. Koh, Z. Shi, D. E. Savage, M. G. Lagally, R. Joynt, M. Friesen, S. N. Coppersmith, and M. A. Eriksson, *Phys. Rev. Lett.* **106**, 156804 (2011).
- [136] J. R. Prance, Z. Shi, C. B. Simmons, D. E. Savage, M. G. Lagally, L. R. Schreiber, L. M. K. Vandersypen, M. Friesen, R. Joynt, S. N. Coppersmith, and M. A. Eriksson, *Phys. Rev. Lett.* **108**, 046808 (2012).
- [137] B. M. Maune, M. G. Borselli, B. Huang, T. D. Ladd, P. W. Deelman, K. S. Holabird, A. A. Kiselev, I. Alvarado-Rodriguez, R. S. Ross, A. E. Schmitz, M. Sokolich, C. A. Watson, M. F. Gyure, and A. T. Hunter, *Nature* **481**, 344 (2012).

- [138] Z. Shi, C. B. Simmons, D. R. Ward, J. R. Prance, R. T. Mohr, T. S. Koh, J. K. Gamble, X. Wu, D. E. Savage, M. G. Lagally, M. Friesen, S. N. Coppersmith, and M. A. Eriksson, *Phys. Rev. B* **88**, 075416 (2013).
- [139] K. L. Wang, D. Cha, J. Liu, and C. Chen, *Proc. IEEE* **95**, 1866 (2007).
- [140] G. Katsaros, M. Stoffel, F. Fournel, M. Mongillo, V. Bouchiat, F. Lefloch, A. Rastelli, O. G. Schmidt, and S. De Franceschi, *Nature Nanotechnol.* **5**, 458 (2010).
- [141] G. Katsaros, V. N. Golovach, P. Spathis, N. Ares, M. Stoffel, F. Fournel, O. G. Schmidt, L. I. Glazman, and S. De Franceschi, *Phys. Rev. Lett.* **107**, 246601 (2011).
- [142] J.-S. Park, B. Ryu, C.-Y. Moon, and K. J. Chang, *Nano Lett.* **10**, 116 (2010).
- [143] M. Trif, V. N. Golovach, and D. Loss, *Phys. Rev. B* **77**, 045434 (2008).
- [144] M. Kroutvar, Y. Ducommun, D. Heiss, M. Bichler, D. Schuh, G. Abstreiter, and J. Finley, *Nature* **432**, 81 (2004).
- [145] S. Amasha, K. MacLean, I. P. Radu, D. M. Zumbühl, M. A. Kastner, M. P. Hanson, and A. C. Gossard, *Phys. Rev. Lett.* **100**, 046803 (2008).
- [146] J. Dreiser, M. Atatüre, C. Galland, T. Müller, A. Badolato, and A. Imamoglu, *Phys. Rev. B* **77**, 075317 (2008).
- [147] P. Lawaetz, *Phys. Rev. B* **4**, 3460 (1971).
- [148] N. Nishiguchi, *Phys. Rev. B* **50**, 10970 (1994).
- [149] G. L. Bir and G. E. Pikus, *Symmetry and Strain-Induced Effects in Semiconductors* (Wiley, New York, 1974).
- [150] C. P. Slichter, *Principles of Magnetic Resonance* (Springer, Berlin, 1980).
- [151] M. Borhani, V. N. Golovach, and D. Loss, *Phys. Rev. B* **73**, 155311 (2006).
- [152] C. Monroe and J. Kim, *Science* **339**, 1164 (2013).
- [153] M. H. Devoret and R. J. Schoelkopf, *Science* **339**, 1169 (2013).

- [154] D. D. Awschalom, L. C. Bassett, A. S. Dzurak, E. L. Hu, and J. R. Petta, *Science* **339**, 1174 (2013).
- [155] K. Ono, D. G. Austing, Y. Tokura, and S. Tarucha, *Science* **297**, 1313 (2002).
- [156] K. C. Nowack, F. H. L. Koppens, Y. V. Nazarov, and L. M. K. Vandersypen, *Science* **318**, 1430 (2007).
- [157] J. R. Petta, H. Lu, and A. C. Gossard, *Science* **327**, 669 (2010).
- [158] H. Ribeiro, G. Burkard, J. R. Petta, H. Lu, and A. C. Gossard, *Phys. Rev. Lett.* **110**, 086804 (2013).
- [159] A. V. Khaetskii, D. Loss, and L. Glazman, *Phys. Rev. Lett.* **88**, 186802 (2002).
- [160] I. A. Merkulov, A. L. Efros, and M. Rosen, *Phys. Rev. B* **65**, 205309 (2002).
- [161] W. A. Coish and D. Loss, *Phys. Rev. B* **72**, 125337 (2005).
- [162] X. Xu, W. Yao, B. Sun, D. G. Steel, A. S. Bracker, D. Gammon, and L. Sham, *Nature* **459**, 1105 (2009).
- [163] A. Greilich, S. E. Economou, S. Spatzek, D. Yakovlev, D. Reuter, A. Wieck, T. Reinecke, and M. Bayer, *Nature Phys.* **5**, 262 (2009).
- [164] S. M. Clark, K.-M. C. Fu, Q. Zhang, T. D. Ladd, C. Stanley, and Y. Yamamoto, *Phys. Rev. Lett.* **102**, 247601 (2009).
- [165] H. Bluhm, S. Foletti, I. Neder, M. Rudner, D. Mahalu, V. Umansky, and A. Yacoby, *Nature Phys.* **7**, 109 (2011).
- [166] S. G. Carter, S. E. Economou, A. Greilich, E. Barnes, T. Sweeney, A. S. Bracker, and D. Gammon, *Phys. Rev. B* **89**, 075316 (2014).
- [167] W. Yang and L. J. Sham, *Phys. Rev. B* **85**, 235319 (2012).
- [168] X.-F. Shi, *Phys. Rev. B* **87**, 195318 (2013).
- [169] E. Chekhovich, M. Glazov, A. Krysa, M. Hopkinson, P. Senellart, A. Le-maître, M. Skolnick, and A. Tartakovskii, *Nature Phys.* **9**, 74 (2013).

- [170] H. Ribeiro, J. R. Petta, and G. Burkard, *Phys. Rev. B* **82**, 115445 (2010).
- [171] M. Makhonin, K. Kavokin, P. Senellart, A. Lemaître, A. Ramsay, M. Skolnick, and A. Tartakovskii, *Nature Mat.* **10**, 844 (2011).
- [172] L. Gaudreau, G. Granger, A. Kam, G. Aers, S. Studenikin, P. Zawadzki, M. Pioro-Ladriere, Z. Wasilewski, and A. Sachrajda, *Nature Phys.* **8**, 54 (2012).
- [173] M. Munsch, G. Wüest, A. V. Kuhlmann, F. Xue, A. Ludwig, D. Reuter, A. D. Wieck, M. Poggio, and R. J. Warburton, [arXiv:1311.4295](https://arxiv.org/abs/1311.4295).
- [174] M. Bayer, G. Ortner, O. Stern, A. Kuther, A. A. Gorbunov, A. Forchel, P. Hawrylak, S. Fafard, K. Hinzer, T. L. Reinecke, S. N. Walck, J. P. Reithmaier, F. Klopff, and F. Schäfer, *Phys. Rev. B* **65**, 195315 (2002).
- [175] C. Latta, A. Högele, Y. Zhao, A. Vamivakas, P. Maletinsky, M. Kroner, J. Dreiser, I. Carusotto, A. Badolato, D. Schuh, W. Wegscheider, M. Atatüre, and A. Imamoglu, *Nature Phys.* **5**, 758 (2009).
- [176] J. Hildmann, E. Kavousanaki, G. Burkard, and H. Ribeiro, *Phys. Rev. B* **89**, 205302 (2014).
- [177] G. Lindblad, *Commun. Math. Phys.* **48**, 119 (1976).
- [178] M. Bayer, O. Stern, A. Kuther, and A. Forchel, *Phys. Rev. B* **61**, 7273 (2000).
- [179] T. M. Godden, J. H. Quilter, A. J. Ramsay, Y. Wu, P. Brereton, I. J. Luxmoore, J. Puebla, A. M. Fox, and M. S. Skolnick, *Phys. Rev. B* **85**, 155310 (2012).
- [180] J. M. Smith, P. A. Dalgarno, R. J. Warburton, A. O. Govorov, K. Karrai, B. D. Gerardot, and P. M. Petroff, *Phys. Rev. Lett.* **94**, 197402 (2005).
- [181] S. Takahashi, R. S. Deacon, A. Oiwa, K. Shibata, K. Hirakawa, and S. Tarucha, *Phys. Rev. B* **87**, 161302 (2013).
- [182] M. Grundmann, J. Christen, N. N. Ledentsov, J. Böhrer, D. Bimberg, S. S. Ruvimov, P. Werner, U. Richter, U. Gösele, J. Heydenreich, V. M. Ustinov, A. Y. Egorov, A. E. Zhukov, P. S. Kop'ev, and Z. I. Alferov, *Phys. Rev. Lett.* **74**, 4043 (1995).

- [183] S. Ruvimov, P. Werner, K. Scheerschmidt, U. Gösele, J. Heydenreich, U. Richter, N. N. Ledentsov, M. Grundmann, D. Bimberg, V. M. Ustinov, A. Y. Egorov, P. S. Kopev, and Z. I. Alferov, *Phys. Rev. B* **51**, 14766 (1995).
- [184] N. N. Ledentsov, V. A. Shchukin, M. Grundmann, N. Kirstaedter, J. Böhrer, O. Schmidt, D. Bimberg, V. M. Ustinov, A. Y. Egorov, A. E. Zhukov, P. S. Kopev, S. V. Zaitsev, N. Y. Gordeev, Z. I. Alferov, A. I. Borovkov, A. O. Kosogov, S. S. Ruvimov, P. Werner, U. Gösele, and J. Heydenreich, *Phys. Rev. B* **54**, 8743 (1996).
- [185] M. Bayer, P. Hawrylak, K. Hinzer, S. Fafard, M. Korkusinski, Z. R. Wasilewski, O. Stern, and A. Forchel, *Science* **291**, 451 (2001).
- [186] F. Troiani, D. Stepanenko, and D. Loss, *Phys. Rev. B* **86**, 161409 (2012).
- [187] P.-Q. Jin, M. Marthaler, A. Shnirman, and G. Schön, *Phys. Rev. Lett.* **108**, 190506 (2012).
- [188] C. Cohen-Tannoudji, B. Diu, and F. Laloe, *Quantum mechanics. Vol. 1* (Wiley, New York, 1977).
- [189] C. Pryor, M.-E. Pistol, and L. Samuelson, *Phys. Rev. B* **56**, 10404 (1997).
- [190] C. Pryor, *Phys. Rev. B* **57**, 7190 (1998).
- [191] O. Stier, M. Grundmann, and D. Bimberg, *Phys. Rev. B* **59**, 5688 (1999).
- [192] A. De and C. E. Pryor, *Phys. Rev. B* **76**, 155321 (2007).
- [193] P. P. Horley, P. Ribeiro, V. R. Vieira, J. González-Hernández, Y. V. Vorobiev, and L. G. Trápaga-Martínez, *Physica E* **44**, 1602 (2012).
- [194] Y. V. Vorobiev, T. V. Torchynska, and P. P. Horley, *Physica E* **51**, 42 (2013).
- [195] A. V. Nenashev and A. V. Dvurechenskii, *J. Appl. Phys.* **107**, 064322 (2010).
- [196] C. E. Pryor and M. E. Flatté, *Phys. Rev. Lett.* **96**, 026804 (2006).
- [197] C. E. Pryor and M. E. Flatté, *Phys. Rev. Lett.* **99**, 179901 (2007).

- [198] M. Bayer, A. Kuther, A. Forchel, A. Gorbunov, V. B. Timofeev, F. Schäfer, J. P. Reithmaier, T. L. Reinecke, and S. N. Walck, *Phys. Rev. Lett.* **82**, 1748 (1999).
- [199] G. Medeiros-Ribeiro, M. V. B. Pinheiro, V. L. Pimentel, and E. Marega, *Appl. Phys. Lett.* **80**, 4229 (2002).
- [200] S. d'Hollosy, G. Fábíán, A. Baumgartner, J. Nygård, and C. Schönenberger, *AIP Conf. Proc.* **1566**, 359 (2013).
- [201] R. S. Deacon, Y. Kanai, S. Takahashi, A. Oiwa, K. Yoshida, K. Shibata, K. Hirakawa, Y. Tokura, and S. Tarucha, *Phys. Rev. B* **84**, 041302 (2011).
- [202] W.-K. Li, *J. Chem. Educ.* **61**, 1034 (1984).
- [203] J. van Bree, A. Y. Silov, P. M. Koenraad, M. E. Flatté, and C. E. Pryor, *Phys. Rev. B* **85**, 165323 (2012).
- [204] E. E. Vdovin, A. Levin, A. Patan, L. Eaves, P. C. Main, Y. N. Khanin, Y. V. Dubrovskii, M. Henini, and G. Hill, *Science* **290**, 122 (2000).
- [205] P. Stano and P. Jacquod, *Phys. Rev. B* **82**, 125309 (2010).
- [206] J. Alicea, *Rep. Prog. Phys.* **75**, 076501 (2012).
- [207] A. P. Higginbotham, F. Kuemmeth, T. W. Larsen, M. Fitzpatrick, J. Yao, H. Yan, C. M. Lieber, and C. M. Marcus, *Phys. Rev. Lett.* **112**, 216806 (2014).
- [208] A. P. Higginbotham, T. W. Larsen, J. Yao, H. Yan, C. M. Lieber, C. M. Marcus, and F. Kuemmeth, *Nano Lett.* **14**, 3582 (2014).
- [209] F. Maier, C. Kloeffel, and D. Loss, *Phys. Rev. B* **87**, 161305 (2013).
- [210] C. Kloeffel, M. Trif, P. Stano, and D. Loss, *Phys. Rev. B* **88**, 241405 (2013).
- [211] F. A. D'Altroy and H. Y. Fan, *Phys. Rev.* **103**, 1671 (1956).
- [212] G. Wentzel, *Phys. Rev.* **83**, 168 (1951).
- [213] J. Bardeen, *Rev. Mod. Phys.* **23**, 261 (1951).
- [214] D. Loss and T. Martin, *Phys. Rev. B* **50**, 12160 (1994).

- [215] T. Martin, Phys. D **83**, 216 (1995).
- [216] K. A. Muttalib and V. J. Emery, Phys. Rev. Lett. **57**, 1370 (1986).
- [217] A. Schulz, A. De Martino, P. Ingenuovon, and R. Egger, Phys. Rev. B **79**, 205432 (2009).
- [218] B. Braunecker, P. Simon, and D. Loss, Phys. Rev. B **80**, 165119 (2009).
- [219] B. Braunecker, G. I. Japaridze, J. Klinovaja, and D. Loss, Phys. Rev. B **82**, 045127 (2010).
- [220] S. Gangadharaiah, B. Braunecker, P. Simon, and D. Loss, Phys. Rev. Lett. **107**, 036801 (2011).
- [221] E. M. Stoudenmire, J. Alicea, O. A. Starykh, and M. P. Fisher, Phys. Rev. B **84**, 014503 (2011).
- [222] L. Fu and C. L. Kane, Phys. Rev. Lett. **100**, 096407 (2008).
- [223] M. Sato and S. Fujimoto, Phys. Rev. B **79**, 094504 (2009).
- [224] Y. Tanaka, T. Yokoyama, and N. Nagaosa, Phys. Rev. Lett. **103**, 107002 (2009).
- [225] S. Sasaki, M. Kriener, K. Segawa, K. Yada, Y. Tanaka, M. Sato, and Y. Ando, Phys. Rev. Lett. **107**, 217001 (2011).
- [226] D. Chevallier, D. Sticlet, P. Simon, and C. Bena, Phys. Rev. B **85**, 235307 (2012).
- [227] D. Sticlet, C. Bena, and P. Simon, Phys. Rev. Lett. **108**, 096802 (2012).
- [228] J. Klinovaja, A. Yacoby, and D. Loss, Phys. Rev. B **90**, 155447 (2014).
- [229] M. Kjaergaard, K. Wölms, and K. Flensberg, Phys. Rev. B **85**, 020503 (2012).
- [230] J. Klinovaja, P. Stano, and D. Loss, Phys. Rev. Lett. **109**, 236801 (2012).
- [231] A. C. Potter and P. A. Lee, Phys. Rev. B **83**, 094525 (2011).
- [232] J. Klinovaja, P. Stano, A. Yazdani, and D. Loss, Phys. Rev. Lett. **111**, 186805 (2013).

- [233] B. Braunecker and P. Simon, *Phys. Rev. Lett.* **111**, 147202 (2013).
- [234] M. M. Vazifeh and M. Franz, *Phys. Rev. Lett.* **111**, 206802 (2013).
- [235] J. Klinovaja, S. Gangadharaiah, and D. Loss, *Phys. Rev. Lett.* **108**, 196804 (2012).
- [236] J. Klinovaja, G. J. Ferreira, and D. Loss, *Phys. Rev. B* **86**, 235416 (2012).
- [237] J. Klinovaja and D. Loss, *Phys. Rev. X* **3**, 011008 (2013).
- [238] C. Dutreix, M. Guigou, D. Chevallier, and C. Bena, *The European Physical Journal B* **87**, 296 (2014), 10.1140/epjb/e2014-50243-9.
- [239] J. Klinovaja and D. Loss, *Phys. Rev. B* **88**, 075404 (2013).
- [240] J. R. Williams, A. J. Bestwick, P. Gallagher, S. S. Hong, Y. Cui, A. S. Bleich, J. G. Analytis, I. R. Fisher, and D. Goldhaber-Gordon, *Phys. Rev. Lett.* **109**, 056803 (2012).
- [241] F. Maier, T. Meng, and D. Loss, *Phys. Rev. B* **90**, 155437 (2014).
- [242] N. Ares, V. N. Golovach, G. Katsaros, M. Stoffel, F. Fournel, L. I. Glazman, O. G. Schmidt, and S. De Franceschi, *Phys. Rev. Lett.* **110**, 046602 (2013).
- [243] N. Ares, G. Katsaros, V. N. Golovach, J. J. Zhang, A. Prager, L. I. Glazman, O. G. Schmidt, and S. De Franceschi, *Appl. Phys. Lett.* **103**, 263113 (2013).
- [244] E. Prada, P. San-Jose, and R. Aguado, *Phys. Rev. B* **86**, 180503 (2012).
- [245] S. Das Sarma, J. D. Sau, and T. D. Stanescu, *Phys. Rev. B* **86**, 220506 (2012).
- [246] D. Rainis, L. Trifunovic, J. Klinovaja, and D. Loss, *Phys. Rev. B* **87**, 024515 (2013).
- [247] J. Klinovaja and D. Loss, [arXiv:1408.3366](https://arxiv.org/abs/1408.3366) .
- [248] S. Bravyi, D. P. DiVincenzo, and D. Loss, *Ann. Phys. (NY)* **326**, 2793 (2011).
- [249] J. Klinovaja and D. Loss, *Phys. Rev. B* **86**, 085408 (2012).

- [250] D. Futterer, M. Governale, U. Zülicke, and J. König, Phys. Rev. B **84**, 104526 (2011).
- [251] A. G. Moghaddam, T. Kernreiter, M. Governale, and U. Zülicke, Phys. Rev. B **89**, 184507 (2014).
- [252] A. A. Zyuzin, D. Rainis, J. Klinovaja, and D. Loss, Phys. Rev. Lett. **111**, 056802 (2013).
- [253] Y. Oreg, E. Sela, and A. Stern, Phys. Rev. B **89**, 115402 (2014).
- [254] J. Klinovaja and D. Loss, Phys. Rev. B **90**, 045118 (2014).
- [255] J. Klinovaja and D. Loss, Phys. Rev. Lett. **112**, 246403 (2014).
- [256] J. C. Y. Teo and C. L. Kane, Phys. Rev. B **89**, 085101 (2014).
- [257] J. Klinovaja and D. Loss, Phys. Rev. Lett. **111**, 196401 (2013).
- [258] T. Neupert, C. Chamon, C. Mudry, and R. Thomale, Phys. Rev. B **90**, 205101 (2014).
- [259] T. Meng, P. Stano, J. Klinovaja, and D. Loss, Eur. Phys. J. B **87**, 203 (2014).
- [260] J. Klinovaja and D. Loss, Eur. Phys. J. B **87**, 171 (2014).
- [261] I. Seroussi, E. Berg, and Y. Oreg, Phys. Rev. B **89**, 104523 (2014).
- [262] E. Sagi and Y. Oreg, Phys. Rev. B **90**, 201102 (2014).
- [263] J. Klinovaja and Y. Tserkovnyak, Phys. Rev. B **90**, 115426 (2014).
- [264] F. Maier and D. Loss, Phys. Rev. B **85**, 195323 (2012).
- [265] E. Ivchenko and A. Kiselev, JETP Lett. **67**, 43 (1998).
- [266] A. A. Kiselev, E. L. Ivchenko, and U. Rössler, Phys. Rev. B **58**, 16353 (1998).
- [267] J. J. Sakurai, *Modern quantum mechanics* (Addison-Wesley, 1994).
- [268] N. J. Traynor, R. T. Harley, and R. J. Warburton, Phys. Rev. B **51**, 7361 (1995).
- [269] M. Silver, W. Batty, A. Ghiti, and E. P. O'Reilly, Phys. Rev. B **46**, 6781 (1992).

- [270] H. Mayer and U. Rössler, *Phys. Rev. B* **44**, 9048 (1991).
- [271] M. Bayer, S. N. Walck, T. L. Reinecke, and A. Forchel, *Phys. Rev. B* **57**, 6584 (1998).
- [272] G. L. Bir and G. E. Pikus, *Sov. Phys.- Sol. State* **3**, 2221 (1962).
- [273] H.-R. Trebin, B. Wolfstädter, H. Pascher, and H. Häfele, *Phys. Rev. B* **37**, 10249 (1988).
- [274] M. H. Weiler, R. L. Aggarwal, and B. Lax, *Phys. Rev. B* **17**, 3269 (1978).
- [275] M. E. Levinshtein, S. Rumyantsev, and M. Shur, *Handbook series on semiconductor parameters* (World Scientific, Singapore, 1996).
- [276] A. Gold and A. Ghazali, *Phys. Rev. B* **41**, 7626 (1990).
- [277] M. Abramowitz and I. A. Stegun, *Handbook of Mathematical Functions* (Dover, New York, 1964).

Curriculum Vitae

Franziska Maier

Date of Birth May 30, 1985
Place of Birth Karlsruhe, Germany

Education

2010 - 2014 PhD Student in the Group of Prof. Dr. Daniel Loss
 University of Basel, Switzerland

2010 Diploma in Physics (equivalent to a MSc)
 University of Konstanz, Germany

2004 Abitur
 Fürstenberg-Gymnasium, Donaueschingen, Germany

List of Publications

1. *Electrically-tunable hole g-factor of an optically-active quantum dot for fast spin rotations*
Jonathan H. Prechtel, Franziska Maier, Julien Houel, Andreas V. Kuhlmann, Arne Ludwig, Andreas D. Wieck, Richard J. Warburton, and Daniel Loss,
arXiv:1412.4238.
2. *Majorana fermions in Ge/Si hole nanowires*
Franziska Maier, Jelena Klinovaja, and Daniel Loss,
Phys. Rev. B **90**, 195421 (2014).
3. *Strongly interacting holes in Ge/Si nanowires*
Franziska Maier, Tobias Meng, and Daniel Loss,
Phys. Rev. B **90**, 155437 (2014).
4. *Nuclear spin diffusion mediated by heavy hole hyperfine non-collinear interactions*
Hugo Ribeiro, Franziska Maier, and Daniel Loss,
arXiv:1403.0490.
5. *Anisotropic g factor in InAs self-assembled quantum dots*
Robert Zielke, Franziska Maier, and Daniel Loss,
Phys. Rev. B **89**, 115438, (2014).
6. *Tunable g factor and phonon-mediated hole spin relaxation in Ge/Si nanowire quantum dots*
Franziska Maier, Christoph Kloeffel, and Daniel Loss,
Phys. Rev. B **87**, 161305(R) (2013).
7. *Effect of strain on hyperfine-induced hole-spin decoherence in quantum dots*
Franziska Maier and Daniel Loss,
Phys. Rev. B **85**, 195323 (2012).

